

**IDENTIFICATION AND CHARACTERIZATION OF
LARGE, AND VERY LARGE SCALE MOTIONS IN
NUMERICALLY SIMULATED ATMOSPHERIC
BOUNDARY LAYERS**

by

Mohammad Ahsanuzzaman Khan

A dissertation submitted to the faculty of
The University of Utah
in partial fulfillment of the requirements for the degree of

Doctor of Philosophy

Department of Mechanical Engineering

The University of Utah

May 2018

Copyright © Mohammad Ahsanuzzaman Khan 2018

All Rights Reserved

The University of Utah Graduate School

STATEMENT OF DISSERTATION APPROVAL

The dissertation of Mohammad Ahsanuzzaman Khan
has been approved by the following supervisory committee members:

<u>Rob Stoll</u> ,	Chair(s) <u> </u>	Date Approved
<u>Eric Pardyjak</u> ,	Member <u> </u>	Date Approved
<u>Marc Calaf</u> ,	Member <u> </u>	Date Approved
<u>Meredith Metzger</u> ,	Member <u> </u>	Date Approved
<u>Steven K. Krueger</u> ,	Member <u> </u>	Date Approved

by Tim Ameel, Chair/Dean of
the Department/College/School of Mechanical Engineering
and by David Kieda, Dean of The Graduate School.

ABSTRACT

Turbulence in the Atmospheric Boundary Layer (ABL) is composed of a wide range of length and time scales. To fully understand the turbulent dynamics of these motions in the ABL, it is necessary to understand the interplay between these length and time scales and their dependence on and interaction with different forcing and boundary conditions. Various studies have confirmed the existence of Very Large Scale Motions (termed as “VLSMs”) in internal and external flows and statistical properties of these large-scale motions have been cataloged. However, how these structures or motions are affected throughout the ABL by realistic forcing conditions where rotation plays a significant role has yet to be explored. Also, not well understood is the interaction of VLSMs with smaller scales in regard to the turbulent kinetic energy exchange. Aside from the dynamical significance of the VLSMs, the detection and characterization of these structures is often not straightforward. In this study a new detection methodology was developed and used for the characterization of VLSMs in the ABL and additionally, the turbulent kinetic energy exchange between large-scale and smaller scale motions was studied quantitatively. The time scale of the VLSMs along with the challenge associated with identifying the correct length scale is highlighted. It was found that any rotation in the domain makes it difficult to identify the length scales of large-scale motions from velocity component energy spectra. Rotation was also found to inhibit the spatial extent of VLSMs in the primary wind direction while expanding it in the cross wind direction. However, given this, it is somewhat surprising that rotation does not have a significant influence on the energy exchange dynamics between scales. Finally, the spatial development of the large-scale motions and related hypotheses have been revisited in the light of the obtained results.

For my parents, Mukhlisur Rahman Khan and Anwara Khanom

CONTENTS

ABSTRACT	iii
LIST OF FIGURES	vii
LIST OF TABLES	x
CHAPTERS	
1. INTRODUCTION	1
1.1 References	3
2. LENGTH SCALE OF AND EFFECT OF ROTATION ON VERY LARGE SCALE MOTIONS	4
2.1 Introduction	4
2.2 Numerical Simulation	7
2.2.1 Simulation Setup	8
2.3 Results	9
2.3.1 Bulk Statistics and Mean Vertical Profiles	10
2.3.2 Correlation and Spectral Characteristics	11
2.3.3 Filtering and Conditional Averaging	15
2.4 Conclusion	19
2.5 References	20
3. MODULATION BY VERY LARGE SCALES AND SCALE-SCALE ENERGY TRANSFER TO AND FROM LARGE-SCALE MOTION .	30
3.1 Introduction	30
3.2 Large Eddy Simulations	33
3.3 Modulation of Small Scale Fluctuations by VLSMs	36
3.4 Analysis of Interscale Energy Transfer in the Wavelet Domain	40
3.5 Summary and Conclusions	48
3.6 References	50
4. TIME SCALE OF VERY LARGE SCALE MOTIONS	64
4.1 Introduction	64
4.2 Large Eddy Simulation	66
4.3 Dynamic Mode Decomposition	66
4.4 Results and Discussion	69
4.5 Summary and Conclusions	71
4.6 References	71
5. CONCLUSIONS AND FUTURE DIRECTIONS	78

5.1 Summary	78
-------------------	----

APPENDICES

A. TURBULENT KINETIC ENERGY EQUATION FOR A HORIZONTALLY HOMOGENEOUS, QUASI-STEADY FLOW	82
---	----

LIST OF FIGURES

2.1	Measurement of unsteadiness in the mean flow and the profile of vertical gradient. (a). C_u, C_v plotted against non-dimensional time tf for EK10 and EK02. Solid lines correspond to C_u and dotted lines to C_v . (b). Nondimensional vertical gradient of mean streamwise velocity, $\Phi_M = \kappa z u_*^{-1} d \langle \bar{u} \rangle / dz$ plotted as a function of nondimensional height. Lines with markers +, \circ , \diamond correspond to CHNL, EK10, and EK02, respectively. The solid black line corresponds to the classical log law expected to hold in the surface layer.	23
2.2	Normalized vertical profiles of time and horizontally averaged resolved and SGS stresses. (a) $\langle \bar{u}_1' \bar{u}_3' + \tau_{13} \rangle$ and τ_{13} plotted as a function of height normalized by boundary layer height (δ) for cases EK10, EK02, and CHNL. Solid lines correspond to $\langle \bar{u}_1' \bar{u}_3' + \tau_{13} \rangle$ and dotted lines correspond to τ_{13} . (b) $\langle \bar{u}_2' \bar{u}_3' + \tau_{23} \rangle$ and τ_{23} plotted as a function of normalized height for cases EK10, EK02, and CHNL. Solid lines correspond to $\langle \bar{u}_2' \bar{u}_3' + \tau_{23} \rangle$ and dotted lines to τ_{23} . Line types $-\circ-$, $-\square-$ and $-+ -$ correspond to EK10, EK02, and CHNL, respectively.	23
2.3	Vertical Rossby number profile of EK10 and EK02 plotted as a function of normalized height.	24
2.4	Correlation of u-velocity component. (a), (b), (c) show correlation of reference level $z/\delta = 0.5$ with all other horizontal levels as defined by equation 2.5 for CHNL, EK10, and EK02, respectively. Red iso-surfaces denote correlation greater than or equal to 0.25 and blue iso-surfaces show negative correlation, smaller or equal to -0.15 . (a', b', c'). show planar autocorrelation, R_{uu}^{2D} of CHNL, EK10, and EK02 at $x_3 = 0.5\delta$, respectively.	25
2.5	Premultiplied velocity spectra against normalized wavelengths are shown for different cases. (a), (b), (c) show spectra of the u -component of the velocity for CHNL, EK10, and EK02, respectively. (a'), (b'), (c') show spectra of the v -component of the velocity for CHNL, EK10, and EK02, respectively. Curves marked with $(\circ, \times, \diamond, +)$ correspond to heights $x_3/\delta = (0.06, 0.15, 0.30, 0.45, 0.71, 0.90) \pm 0.01$, respectively.	26
2.6	Identification of VLSMs. (Left) For the CHNL case, a cropped binarized negative u' velocity field image is shown which is overlayed with detected elliptical coherent structures with a range of major axis length lengths, $\delta - 10\delta$. (Right) Zoomed-in two detected structures with interior points painted in blue where average shear stresses were calculated are shown. Horizontal and vertical axes are aligned with streamwise and spanwise directions, respectively	27

2.7	Cumulative density function of coherent structure lengths, their aggregate contribution to shear stress as functions of height, and their average lengths. The left panel shows cumulative density function of the structure lengths detected in the range $\delta - 25\delta$ for <i>CHNL</i> (a), <i>EK10</i> (b), and <i>EK02</i> (c) cases. The arrows point to the direction of increasing distance from the surface. The panel on the right-hand side shows the ratio (d) $\tau_{x,y}^f/A_f$ plotted for different wall normal locations of all cases. (e) shows the mean length of major axes for all structures detected and (f) shows the mean minor axes lengths. Here (—○—) represents <i>CHNL</i> , (—×—) represents <i>EK10</i> , and (—○—) represents <i>EK02</i>	28
2.8	3D structures of VLSMs. (a), (b), (c) show the average 3D structures projected from detected 2D transects at the height of the first vertical grid point for the <i>CHNL</i> , <i>EK10</i> and <i>EK02</i> cases, respectively. (a'), (b'), (c') show the top view of the same 3D structures as shown on the left panels. Iso surfaces enclose values less than $\langle u \rangle - 1.5\sigma_u$	29
3.1	An illustration of the data extraction method used to investigate the modulation of the small-scale motions by large-scale motions is shown. The black dashed line in the figure represents a raw velocity signal ($u_1(x_3)$) extracted along a line in x_1 -direction from the simulated flow field. The filtered large-scale fluctuation (u_L) is represented by the red smooth line. The dotted blue line represents the data series of small-scale fluctuation (u_s). On the left, a hypothetical binning process for the u_L series is shown and the association of the representative u_L values to the correct bin is shown with arrows.	54
3.2	The relative strength of small-scale fluctuations conditioned on the strength of fluctuations of large scales as defined in Eq. 3.5 for the three different flow cases, (a) <i>CHNL</i> , (b) <i>EK10</i> , and (c) <i>EK02</i>	55
3.3	The wavenumber quantifying the scale of fluctuation of primary turbulent motions as a function of large-scale fluctuation intensities for the three cases, (a) <i>CHNL</i> , (b) <i>EK10</i> , and (c) <i>EK02</i>	55
3.4	The wall-normal Reynolds shear stress, $u'w'$, normalized by the surface shear stress as a function of large-scale fluctuations and distance in the wall-normal direction for each of the cases, (a) <i>CHNL</i> , (b) <i>EK10</i> , and (c) <i>EK02</i> . Solid lines correspond to the mean shear stress, $\langle u'w' \rangle_{u_L}$, and points correspond to $\pm 3\sigma_{u_L}^{u'w'}$	56
3.5	Premultiplied wavelet and Fourier spectra of streamwise velocity component, averaged over spanwise direction for (a) <i>CHNL</i> , (b) <i>EK10</i> , and (c) <i>EK02</i> at different wall-normal locations. Spectra are plotted against wavenumbers normalized by height. Lines represent Fourier spectra and circles represent wavelet spectra. Line types —, —, —, —, — correspond to heights (0.01 δ , 0.14 δ , 0.26 δ , 0.39 δ , 0.52 δ) for <i>CHNL</i> , (0.01 δ , 0.14 δ , 0.28 δ , 0.41 δ , 0.54 δ) for <i>EK10</i> , and (0.04 δ , 0.19 δ , 0.34 δ , 0.54 δ , 0.71 δ) for <i>EK02</i>	57

3.6	Wavelet dual bi-spectrum of subgrid scale transfer normalized by u_*^3 for the <i>CHNL</i> case. This figure shows the rate of energy transfer over unit area per unit length of scale where energy transfer occurs from scales r_m/δ to scales smaller than r_n/δ	57
3.7	The rate of energy transfer over unit area per unit length of scale is shown for the <i>EK10</i> case where energy transfer occurs from scales r_m/δ to scales smaller than r_n/δ . Energy transfer is normalized by u_*^3	58
3.8	Wavelet dual bi-spectrum of subgrid scale transfer normalised by u_*^3 for <i>EK02</i> . Energy transfer is measured over unit area per unit length of scale and transfer occurs from scales r_m/δ to scales smaller than r_n/δ	59
3.9	Wavelet dual bi-spectrum of subgrid scale transfer normalised by u_*^3 for the <i>CHNL</i> case. In contrast to Fig. 3.6, this figure shows the transfer occurring between length scales r_m to r_m ($r_n \equiv r_m$).	60
3.10	Wavelet dual bi-spectrum of subgrid scale transfer normalised by u_*^3 for the <i>EK10</i> case. In contrast to Fig. 3.7, this figure shows the transfer occurring between length scales r_m to r_m ($r_n \equiv r_m$).	61
3.11	Wavelet dual bi-spectrum of subgrid scale transfer normalised by u_*^3 for the <i>EK02</i> case. The energy transfer from scale r_m to $r_n (\equiv r_m)$ is shown in contrast to Fig. 3.8 where, $r_n < \frac{1}{2}r_m$	62
3.12	Aggregate subgrid scale energy transfer from large to small scales separated by an arbitrary cut-off scale. For panels on the left, total subgrid transfer is calculated using Eqn. 3.27 and the right-hand side panels correspond to total subgrid transfer calculated following the definition in Eqn. 3.26.	63
4.1	First four DMD modes with characteristic time period as listed in Table 4.2 at heights 0.047δ and 0.095δ for the <i>CHNL</i> case are shown in subfigure (a) and (b), respectively. In subfigure (a), top left panel shows spatial mode corresponding to normalized time period ($\Delta TU(\delta)/\delta$) of 27.09 and top right, bottom left, bottom right panels correspond to 10.19, 6.11, 4.63, respectively. In subfigure (b) panels beginning from top left corner in the clockwise order corresponds to normalized time periods 14.05, 8.78, 5.65, and 4.07, respectively.	74
4.2	DMD modes of different frequencies at a height of 0.48δ are shown for <i>EK02</i> . (a) Four DMD modes in clockwise order beginning from top left panel correspond to normalized time periods of 135.7, 37.4, 21.7, and 15.0. (b) DMD modes with time periods 11.6, 9.5, 8.0, 7.1.	76
4.3	Normalized histogram of the length scales of structures detected in the velocity field reconstructed from individual DMD modes. x -axis represents the length scales of structures normalized by the boundary layer depth δ . A discrete set of structures of length scales $\{0.3, 0.5, 1, 2, 3, 4, 5, 6, 7, 8, 9, 10, 11, 12, 13, 14, 15\}\delta$ were searched in the velocity field. Subfigures (a) and (b) represents respectively, <i>CHNL</i> and <i>EK02</i> . For each of these two cases the four analysed DMD modes correspond to the first four modes as listed in Table 4.2 (at 0.5δ), and 4.3 (at 0.48δ) and are plotted in clockwise fashion beginning from the top left panel of each subfigure.	77

LIST OF TABLES

2.1	Simulation parameters and flow characteristics	24
2.2	Fraction of the cumulative energy contained by all the spatial scales greater than the specified threshold at a height of $x_3 = 0.45\delta (\pm 0.01\delta)$ for the u_1 -component in the x_1 -direction	24
3.1	Simulation parameters	55
3.2	Wavelet decomposition levels and corresponding normalised horizontal length scales (r_m/δ) and wavenumbers ($k_m\delta$) of all three cases.	56
4.1	Simulation parameters	75
4.2	Time period of evolution of the first five DMD modes normalized by $\delta/U(z)$ for <i>CHNL</i> . Modes were calculated at different horizontal planes characterized by normalized heights presented.	75
4.3	Statistics of the first five DMD modes for <i>EK02</i> . DMD time periods are normalized by $\delta/U(z)$. Modes were calculated at different horizontal planes characterized by normalized heights presented.	75

CHAPTER 1

INTRODUCTION

The lower ten percent of the entire atmosphere is commonly known as the Atmospheric Boundary Layer (ABL). Most living organisms are engulfed by the ABL and are affected by the mixing processes in the ABL that dictate the distribution of particles e.g. moisture, carbon, and pollutants. The large-scale mixing processes in the ABL are mostly governed by turbulence. Thus, understanding the turbulence dynamics in the ABL has always been pivotal to endeavours oriented towards improving living conditions, comforts, prediction of impending disasters, and economic activities such as farming. The collective human efforts towards understanding the ABL are reflected in the enormous amount of literature and computational capacities dedicated to numerical weather modeling. As of today, the National Oceanic and Atmospheric Administration (NOAA) alone hosts a high-performance computing facility capable of operating at 5.78 petaflops, dedicated to run operational weather models of various ranges. Nevertheless, it has nearly been a hundred years since the onset of turbulence research. Lumely and Yaglom [1] while commenting on the current state of knowledge on turbulence have said “we do have a crude, practical, working understanding of many turbulence phenomena but certainly nothing approaching a comprehensive theory, and nothing that will provide predictions of an accuracy demanded by designers”.

There are many competing definitions of turbulence and some of them reiterated in [2, 3] emphasize that no definition of turbulence is sufficiently adequate to capture the essence of this complex phenomena. Turbulence can be better understood by its characteristics and properties. The properties as have been described by Tsinober [3] are briefly mentioned here:

- Turbulence possess intrinsic spatio-temporal randomness and irregularity
- Turbulence encompasses extremely wide range of strongly interacting scales
- The details of turbulent flows are extremely sensitive to perturbations

- Turbulent flows are dissipative. Sustenance of turbulence requires external energy input
- Turbulent flows are always three-dimensional and rotational

It is apparent that turbulence dictates mixing processes at multitudes of scales, be it mixing of momentum or scalar such as temperature, particulates. The range of scales that might be present in any flow can be quantified by the non-dimensional Reynold's number Re ($Re = v_c L_c / \nu$ where, v_c is the characteristic velocity, L_c is the characteristic length, and ν is the kinematic viscosity). In the ABL Re is usually as high as 10^6 . According to the definition of Re this means that the largest scale in ABL can be as large as 10^6 times the smallest scale. In this study we are interested in the Large and Very Large Scale Motions (LSMs & VLSMs) that can span hundred of meters to several kilometres in length scale. At these large scales viscosity does not play any significant role. Thus, studying inviscid flow is sufficient to understand the turbulence dynamics of LSMs and VLSMs. However, studying turbulence dynamics at any scale in the ABL necessitates taking into consideration of a wide variety of forcing and boundary/surface conditions. ABL flow is influenced strongly by rotation of the earth and density gradient in the wall-normal direction known as stratification. The surface condition in the ABL can be quite diverse in real life situation. Various types of land cover and surface heating due to solar radiation needs to be accounted for in the study of a real life ABL flow. However, in order to study only the effect of a single forcing or boundary condition all other force and boundary conditions must be kept constant and invariant over the time period considered. Numerical simulation lends itself as a suitable method to study the effect of a particular external force or boundary condition. So, we generated ABL flow field with numerical simulations. In our study we explore the effect of rotation of the earth on turbulent dynamics of the VLSMs and LSMs.

In this present study we have put forth our efforts to re-examine turbulence characteristics of LSMs and VLSMs. We also attempted to add new insights, and methods to existing tools and techniques to identify VLSMs and LSMs. In the second chapter we introduce a new technique based on common image processing algorithms to identify and characterize VLSMs. In the third chapter we assess the interactions of VLSMs and LSMs with other smaller scales in order to understand the dynamical importance of these large scale motions

on overall turbulence dynamics. The fourth chapter delineates application of dynamic mode decomposition to characterize VLSMs. Especially the properties of VLSMs deduced from conditional averaging procedures or other filtering techniques can be compared with DMD results and conclusions are made about organization of VLSMs.

1.1 References

- [1] John L. Lumely and Akiva M. Yaglom. A century of turbulence. *Flow, Turbulence and Combustion*, 66:241–286, 2001.
- [2] J O Hinze. *Turbulence*. McGraw-Hill Inc., 1975.
- [3] Arkady Tsinober. *An Informal Introduction to Turbulence*. Kluwer Academic Publishers, 2001.

CHAPTER 2

LENGTH SCALE OF AND EFFECT OF ROTATION ON VERY LARGE SCALE MOTIONS

Very Large Scale Motions (VLSMs) were studied under the effect of the Coriolis force. Previous studies confirmed the presence of VLSMs in channel and ABL flows through experimentation and simulations. However, due to limitations in experimentation and the lack of the account of Coriolis force in numerical simulations, the effects of rotation on VLSM have not been thoroughly examined. Here, the Large Eddy Simulation (LES) technique was used to simulate VLSMs under different degrees of rotation. Both traditional statistical and image processing techniques were then used to characterize them. The traditional method of determination of length scales of VLSMs from pre multiplied spectra of the stream-wise velocity component proved to be inadequate when rotation was introduced. By identifying the footprints of VLSMs as connected regions of low momentum fluid and then identifying those regions through standard image processing tools, the difficulties in determining the VLSM length scales could be circumvented. It was found that rotation inhibited the coherence and suppressed the development of VLSMs in the ABL flows. Also, it was found that the usual practice of visually identifying VLSM on numerically filtered velocity fields as long regions of low momentum might not be sufficiently accurate.

2.1 Introduction

In general, turbulent flows are composed of constituent coherent structures and background flows [4]. The dynamics and role of coherent structures are thus fundamental to the understanding of complex motions and mixing processes in the Atmospheric Boundary Layer (ABL) [5, 6]. Very Large Scale Motions (VLSMs) in the ABL have garnered significant interests of the research community lately [7, 8]. VLSMs are identified as very long regions of low momentum aligned in the streamwise direction that are flanked by high momentum

regions and they have been observed in turbulent pipe [9, 10, 11], channel [9, 11, 12], and boundary layer flows [13, 14]. The rich features of VLSMs and their importance were demonstrated in both experimental [9, 10, 11, 14] and numerical studies [12, 13, 15]. However, a concrete definition of VLSMs is lacking, which makes the identification of these structures highly subjective. A threshold value has to be chosen to differentiate between the low-momentum streaks and the bulk flow and it has been shown that the chosen threshold value dictates the number of VLSMs detected for a particular length scale on a given horizontal plane [16]. In these applications, the length scale of VLSMs scales with δ where δ refers to Boundary Layer (BL) height, channel half width, or pipe radius [11, 17]. From flow visualizations, the largest length scale of these coherent structures were shown to be approximately 20δ . However, the largest length scale from two-point correlation was consistently underpredicted and was reported to vary from 4δ to 2.5δ in the outer region of the BL. Hutchins and Marusic [14] hypothesized that the spanwise meandering of VLSMs could be responsible for the underestimation of streamwise length scales from two-point correlation of streamwise velocity. In this context, another important length scale has been identified to be important that is smaller than VLSMs but plays a dynamically important role like VLSMs. Structures corresponding to these length scales have been termed as the Large Scale Motions (LSMs). While the streamwise autocorrelation has been found to be insufficient at identifying VLSM streamwise length scales, premultiplied spectra have been observed to be of same the order or magnitude compared to visualization of instantaneous flow fields [9]. The presence of VLSMs causes a secondary peak to appear in the large wavelength region of the premultiplied spectra. In the spanwise direction, the extent of VLSMs has been observed to be nearly an order of magnitude smaller compared to the streamwise length scale [11]. The importance of VLSMs manifest in their contribution to the overall magnitude of Reynold's stress and turbulent kinetic energy. A cumulative distribution of turbulent kinetic energy and Reynold's stress over Fourier modes revealed that in pipe flow more than 65% of turbulent energy was due to very large scale motions while their contribution to Reynold's shear stress accounted for as much as 60% [9]. It was also found that large-scale motions with an estimated eddy turnover time of $2\delta/U_\infty$ (where U_∞ denotes the free streamwise velocity) or greater strongly modulate the magnitude of smaller scale fluctuations within the log region and they modulate the frequency of

small-scale fluctuations even more significantly above the log region [18].

Here, our focus is the characterization of VLSMs in the ABL and how they are impacted by Geostrophic forces. Unlike small-scale laboratory flows, the effect of the Earth's rotation cannot be ignored in the ABL and to faithfully represent the physics, conservation equations must be studied in a rotational frame of reference. When conservation of momentum is expressed in a rotational frame, the Earth's rotation is accounted for by the introduction of Coriolis force and this Coriolis force can have an impact on the size and shape of the large eddies of the flow field [19]. The Coriolis force is often referred to as a fictitious force due to lack of contribution to the velocity magnitude and eventually to the mean kinetic energy or turbulent kinetic energy (*tke*). Its importance in kinetic energy redistribution among different scales can be identified []. In the limiting case of zero Rossby number, $Ro = 0$, i.e., in case of solid body rotation or low enough Ro number where inertia is negligible compared to Coriolis force, Taylor Proudman column of vortices are observed. It is the Ro number that signifies the importance of a rotational frame of reference and defined as, $Ro = \frac{U}{2\Omega L}$, where U is the characteristic flow velocity usually a velocity associated with the integral length scale, Ω is the rate of rotation of the reference frame, and L is the characteristic length scale of the flow usually taken as the integral length scale. It can intuitively be predicted that Coriolis force can have an impact on large-scale coherent structures, although the effect is not readily comprehensible.

A consistent theme in VLSM studies is the identification and analysis of their spatial structure and evolution. Previous studies found that organized VLSMs show the presence of finer scales and that the spatial development of VLSMs occurs mainly as a result of the merger of smaller scale motions [12, 15, 16]. One of the possible mechanisms for the development of VLSMs is the merger of hairpin packets marching forward in the downstream direction [15]. Another possible explanation is that concatenation of fast-moving upstream LSMs with slow-moving downstream LSMs constitute VLSMs [12]. In the same study, it was also speculated that streamwise-elongated inclined hairpin vortex packets induce negative streamwise fluctuations that manifest as long low-momentum streaks in the streamwise direction [12]. The association of counter rotating vortex rolls with VLSMs has also been reported as identified from Large Eddy Simulation (LES) [13]. These mechanisms of VLSM formation, while offering a qualitative description, do not provide a comprehensive definition

of the VLSMs and their evolution.

The main objective of this study is to discern the effect of rotation on the characteristics of VLSMs. LESs were carried out over large domains to simulate the Earth's rotational effect. We focused on the coherence of the flow and looked into the known signatures of VLSMs to understand how rotation impacts their characteristics. The quantitative aspect of the contribution of VLSMs under the effect of rotation in overall energy content and Reynold's stresses were studied. A relatively straightforward definition of VLSMs was developed to facilitate a VLSM detection method based on widely used image processing techniques.

2.2 Numerical Simulation

In this study, the Large Eddy Simulation (LES) technique was used to examine the effect of rotation on VLSMs. The models and numerics used in the simulation code are described in detail in Stoll and Porté-Agel [20] and Stoll and Porté-Agel [21]. Here only a brief summary is given. The numerical code solves the spatially filtered incompressible Navier-Stokes equations in rotational form,

$$\frac{\partial \tilde{u}_i}{\partial t} + \tilde{u}_j \left(\frac{\partial \tilde{u}_i}{\partial x_j} - \frac{\partial \tilde{u}_j}{\partial x_i} \right) = -\frac{\partial \tilde{p}^*}{\partial x_i} - \frac{\partial \tau_{ij}}{\partial x_j} + f_c \epsilon_{ij3} \tilde{u}_j, \quad (2.1)$$

where \tilde{u}_i denotes the spatially filtered, resolved velocity in the i -th direction and $i = 1, 2, 3$ correspond to x_1, x_2, x_3 directions, respectively. $p^* = p'/\rho + \frac{1}{2} \tilde{u}_i \tilde{u}_i$ is the modified pressure, τ_{ij} is the subgrid scale (SGS) stress tensor. Viscous forces were assumed to be negligible as a result of the extremely high Reynolds number of the ABL and τ_{ij} was computed using the scale-dependent Lagrangian-averaged dynamic Smagorinsky model of Stoll and Porté-Agel [20]. Horizontal derivatives were calculated using a pseudo-spectral method while vertical derivatives were approximated using second-order central differences, and for time integration, the second-order Adams-Bashforth scheme was used. As surface boundary conditions, the required instantaneous surface shear stresses $\tau_{i3,s}(x, y, t)$ were computed from the instantaneous filtered velocity field at the lowest vertical grid level by local application of the Monin-Obukhov similarity theory [22] as:

$$\tau_{i3,s}(x, y, t) = - \left[\frac{\tilde{u}_r(x, y, (\Delta z/2), t) \kappa}{\ln((\Delta z/2)/z_o)} \right]^2 \frac{\tilde{u}_i(x, y, (\Delta z/2), t)}{\tilde{u}_r(x, y, (\Delta z/2), t)}, \quad (2.2)$$

where κ is the von karman constant ($= 0.4$), z_o is the local aerodynamic roughness ($= 0.1\text{m}$ in all simulated cases), $\tilde{u}_r(x, y, \Delta z/2, t) = [\tilde{u}_1(x, y, \Delta z/2, t)^2 + \tilde{u}_2(x, y, \Delta z/2, t)^2]^{1/2}$ is the local horizontal wind speed, and Δz is the numerical grid spacing in the vertical direction. Although application of Monin-Obukhov similarity theory is not strictly valid instantaneously and locally, sensitivity tests indicate that its primary impact on the flow dynamics is confined to the lowest computational levels [22]. This numerical code has been used to simulate the ABL under a variety of different conditions [23, 24, 25, e.g.,] and to examine the structure and evolution of turbulent motions [26, 27, e.g.,]. Its excellent representation of SGS momentum fluxes [20] makes it ideal for an examination of large-scale ABL velocity field dynamics.

2.2.1 Simulation Setup

Three different simulated flow cases designated as *CHNL*, *EK10*, and *EK02* were examined to assess the effect of rotation on the characteristics of VLSMs in the ABL. Each case was characterized by a different Ro with *CHNL* being a classical channel flow simulation under neutral stability condition driven by a constant horizontal pressure gradient, and *EK10* and *EK02* are Ekman layer simulations under different degrees of rotation. The *CHNL* case can be considered as a limiting case with an infinite Ro .

The focus of the study is large-scale dynamics and therefore, the simulation domain spans large horizontal extents in the x_1 ($L_1 = 128\text{ Km}$) and x_2 ($L_2 = 128\text{ Km}$) directions and has a height of 1500 m (L_3) for *CHNL* and *EK10* and a height of 750 m for *EK02* in the vertical direction. The corresponding numerical grid is discretized with $N_1 = 2048$, $N_2 = 2048$ and $N_3 = 64$ nodes. A summary of the discretization along with basic parameters of the simulations are furnished in Table 4.1 where u_* denotes the friction velocity, U_g denotes the geostrophic wind velocity in the x_1 -direction, δ stands for the boundary layer height, and f_c is the Coriolis parameter with a prescribed value of 10^{-4} s^{-1} . For the *CHNL* case, the flow is driven by a constant mean pressure gradient along the streamwise direction with a prescribed value of $\langle \rho^{-1} \frac{\partial \tilde{p}}{\partial x_1} \rangle = 1.3419 \times 10^{-9}\text{ ms}^{-2}$ where $\langle \rangle$ denotes a horizontal mean. For the *EK10* and *EK02* cases, geostrophic wind velocities (U_g) of 10 ms^{-1} and 2 ms^{-1} are specified, respectively. At the top of the boundary, the assumed balance between pressure and Coriolis force ($\langle \rho^{-1} \frac{\partial \tilde{p}}{\partial x_i} \rangle = f_c \epsilon_{ij3} \tilde{u}_j$) and the imposed stress

free condition ($\frac{\partial \tilde{u}_1}{\partial x_3} = \frac{\partial \tilde{u}_2}{\partial x_3} = 0$) result in the formation of an Ekman layer. The *EK10* case mirrors the simulations of Andren et al. [28] except for the facts that the domain is much larger in this case and the vertical component of the Coriolis force is absent. In terms of forcing, the difference between the simulated *CHNL* and Ekman layer cases is that, in *CHNL*, constant pressure gradient $\langle \rho^{-1} \frac{\partial \tilde{p}}{\partial x_1} \rangle$ acts on the flow while in *EK10* and *EK02*, constant $\langle \rho^{-1} \frac{\partial P}{\partial x_1} \rangle = -f_c(\langle u_2 \rangle - V_g)$, and $\langle \rho^{-1} \frac{\partial P}{\partial x_2} \rangle = f_c(\langle u_1 \rangle - U_g)$ are forcing the flows. Precursor simulations were carried out to generate initial flow fields for *EK10* and *EK02* using a one-dimensional single column model following the initialization procedure of Andren et al. [28]. Prognostic equations for the precursor simulations of *EK10* and *EK02* are shown in Eqn. 2.3.

$$\begin{aligned}\frac{\partial \langle u_1 \rangle}{\partial t} &= f(\langle u_2 \rangle - V_g) - \frac{\partial}{\partial x_3}(u'_1 u'_3) \\ \frac{\partial \langle u_2 \rangle}{\partial t} &= f(\langle u_1 \rangle - U_g) - \frac{\partial}{\partial x_3}(u'_2 u'_3).\end{aligned}\quad (2.3)$$

The turbulent stresses in Eqn. 2.3 $\langle u'_1 u'_3 \rangle$ and $\langle u'_2 u'_3 \rangle$ are estimated using eddy diffusivity models, $\langle u'_1 u'_3 \rangle = -k_m^u \frac{\partial \langle u \rangle}{\partial x_3}$ and $\langle u'_2 u'_3 \rangle = -k_m^v \frac{\partial \langle v \rangle}{\partial x_3}$. Eddy diffusivities in turn were approximated using a single equation mixing length model, which accounts for the atmospheric stability, i.e., $k_m^u = l_m^2 \frac{\partial \langle u_1 \rangle}{\partial x_3} f_m$ and $k_m^v = l_m^2 \frac{\partial \langle u_2 \rangle}{\partial x_3} f_m$ where l_m are mixing lengths estimated to match the initial profiles of Andren et al.[28] and f_m is a prescribed correction factor. For further details on the column model, the reader is referred to the comparative study on single column turbulence schemes in Cuxart et al. [29]. The time integration in precursor simulations were carried out using a second-order Adams-Bashforth model and run until quasi-equilibrium was reached. Once the 1D vertical profiles are created, 3D initial velocity fields were generated by adding random fluctuations to the mean vertical profiles in the surface layer.

2.3 Results

To begin, we looked at the mean statistics of the flows to ascertain the convergence of the simulations and to identify the significant differences among the three cases. Planar linear correlations in the velocity field were also studied to examine the coherence of the flow before proceeding to the direct identification and characterization of VLSMs.

2.3.1 Bulk Statistics and Mean Vertical Profiles

The level of unsteadiness in the mean velocity fields can be measured in terms of coefficients C_u and C_v where,

$$\begin{aligned} C_u &= -\frac{f}{(\bar{u}'_1 \bar{u}'_3)_0} \int_0^{x_3^{top}} (\langle \bar{u}_2 \rangle - V_g) dx_3 \text{ and} \\ C_v &= \frac{f}{(\bar{u}'_1 \bar{u}'_3)_0} \int_0^{x_3^{top}} (\langle \bar{u}_1 \rangle - U_g) dx_3. \end{aligned} \quad (2.4)$$

For a horizontally homogeneous turbulent flow field, C_u and C_v have steady-state values of unity [30]. Unsteadiness in C_u and C_v with respect to the nondimensional inertial time tf is shown in Fig. 2.1(a). Increased nonstationarity is observed in *EK10* compared to *EK02*, especially in the C_v values. Although the oscillations in the two cases tend to have similar damping, a discernible phase lag can be detected. The oscillations are expected to diminish exponentially around the $C_u, C_v = 1$ line [30]. Compared to the same quantities presented by Andren et al. [28], it can be concluded that in the considered cases, the oscillations are relatively damped which may have resulted from averaging the velocities over a larger domain. Overall, the figure indicates that the simulations are reasonably converged.

The nondimensional streamwise velocity gradient, $\Phi_M = \kappa x_3 u_*^{-1} d \langle \bar{u}_1 \rangle / dx_3$, plotted against nondimensional height is shown in Fig. 2.1(b), where, $u_* = -(\langle (\tau_{13,s})^2 + (\tau_{23,s})^2 \rangle)^{1/4}$. Following similarity theory, Φ_M can be predicted to have a value of approximately unity in the lowest 10% of the boundary layer [22, 30]. The values obtained from the simulations are consistent across the different levels of rotation and similar to values obtained previously using LES [22, 28, 31].

In Fig. 2.2, normalized shear stresses are plotted, illustrating an important difference between all the cases. In a horizontally homogeneous field under quasi-steady condition, the applied streamwise pressure gradient balances the total vertical stress gradient as evident from Eqn. 3.2. As a result, a linear vertical profile of the horizontally averaged total stress ($\langle \bar{u}'_1 \bar{u}'_3 + \tau_{13} \rangle$) is expected for the *CHNL* case that goes from a normalized value of -1 to a value of zero at the domain top (Fig. 2.2(a)). For the *EK02* and *EK10* cases, a linear total profile does not emerge in these cases because of a significant contribution to the stress profile from the spanwise stress component ($\langle \bar{u}'_2 \bar{u}'_3 + \tau_{23} \rangle$) that accounts for as much as 30% of the total stress at the ground level (Fig. 2.2(b)).

Figure 2.3 shows the difference in rotational tendencies between *EK10* and *EK02* in terms of the vertical profile of the local Rossby number defined as $Ro_z = \sqrt{\langle \omega_z^2 \rangle} / f$ where ω_z denotes the wall-normal component of the vorticity vector. With increasing height from the ground, the influence of the Coriolis force grows larger, which manifests in a decreasing ratio of inertia to Coriolis forces. *EK02* clearly shows a greater degree of influence of Coriolis force at every height compared to *EK10*, which is consistent with the increased importance of spanwise stress component (Fig. 2.2).

2.3.2 Correlation and Spectral Characteristics

The resolved velocity fields contain a range of large active spatial length scales that are similar or greater to the boundary layer height. A common method used to estimate the extent of the large active scales in the flow is the autocorrelation function with one of its primary functions being to define an integral length scale for a flow. By definition, VLSMs are larger than the integral length scale, but the autocorrelation function can still provide a relative measure of flow length scales present in the three different cases (Fig. 2.4). Integral length scales for the three different cases have been determined, which delineates the differences between the cases. In addition to autocorrelation, cross-correlation has also been studied which primarily provides a measure of the extent of the influence. The panels on the left-hand side of Fig. 2.4 show the streamwise velocity correlation of the mid-boundary layer plane ($z_{ref} = \delta/2$) with all other discrete horizontal levels resolved in the simulations.

The formal definition of this correlation is

$$R_{uu}^{3d}(\Delta x_1, \Delta x_2, x_3, x_3^{ref}) = \frac{\langle u'(x_1, x_2, x_3^{ref}) u'(x_1 + \Delta x_1, x_2 + \Delta x_2, x_3) \rangle}{\langle u'^2(x_1, x_2, x_3^{ref}) \rangle}, \quad (2.5)$$

where $\Delta x_1, \Delta x_2$ are spatial lags between the two points in x_1 - and x_2 -directions, respectively. Typically, juxtaposed low- and high-momentum streaks in the spanwise direction have been identified as a signature of the existence of VLSMs. For the *CHNL* case, iso-surfaces of both positive and negative correlation are visible where $R_{uu}^{3d} \geq 0.25$ is denoted by the red iso-surfaces and $R_{uu}^{3d} \leq -0.15$ is denoted by blue iso-surfaces. The *EK10* and *EK02* cases, do not show negative iso-surfaces on either of the sides of the positively correlated regions for a value of $R_{uu}^{3d} \leq -0.15$. This is a first sign of the impact of rotation on characteristics of VLSMs. These plots also show the maximum vertical extent of influence of active scales existing in the mid-boundary layer. In *CHNL*, the influence

of the largest active scales extends from the bottom of the domain up to 85% of the BL height. This was limited to 80% for the *EK10* and 70% for the *EK02* cases. The panels on the right-hand side of Fig. 2.4 show planar autocorrelation of u_1 -velocity component at $z = 0.5\delta$ where the planar autocorrelation is defined as:

$$R_{uu}^{2d}(\Delta x, \Delta x_2, x_3) = \frac{\langle u'(x_1, x_2, x_3)u'(x + \Delta x_1, x_2 + \Delta x_2, x_3) \rangle}{\langle u'^2(x_1, x_2, x_3) \rangle}. \quad (2.6)$$

The shape, orientation, and spread of the iso-lines are noticeably different for the three cases. Iso-lines of nominal correlation of 0.01 along with -0.1, 0.1, 0.25 are shown. Regions of negative correlation displayed by blue lines most prominently appear in the *CHNL* case. For the *EK10* case, very small regions of negative correlation are visible and for the *EK02* case, regions of negative correlation do not appear alongside the large elongated positively correlated regions. The rotated orientation of the iso-lines in *EK10* and *EK02* indicates the presence of rotation in the flows while in the *CHNL* case, the iso-lines are almost aligned with x_1 and x_2 axes, suggesting a mean-streamwise flow. A greater degree of rotation in *EK02* compared to *EK10* is also apparent from the orientation of the iso-lines corresponding to 0.1 and 0.01.

The lines marked by nominal positive correlation of 0.01 infer that the unidirectional pressure gradient in a channel flow helps retain high coherence of the velocity field and the rotation in geostrophic flows substantially prohibits this coherence. This assessment can be quantified by the examination of integral length scales, which can be defined in x_1 - and x_2 -directions as $L_{int,x_1} = \int_0^\infty dx R_{uu}^{2d}(x_1, 0)$ and $L_{int,x_2} = \int_0^\infty dy R_{uu}^{2d}(0, x_2)$, respectively. Here, a discrete version of the integral length scales was used following Träumner et al. [32] where Δx_1^o and Δx_2^o indicate the location of zero crossings of the correlation function on the x_1 and x_2 axes, respectively.

$$L_{int,x_1} = \sum_{\Delta x_1=0}^{\Delta x_1^o} R_{uu}^{2d}(x_1 + \Delta x_1, 0, x_3)\Delta x_1 \text{ and} \quad (2.7)$$

$$L_{int,x_2} = \sum_{\Delta x_2=0}^{\Delta x_2^o} R_{uu}^{2d}(0, x_2 + \Delta x_2, x_3)\Delta x_2. \quad (2.8)$$

Equations 2.7 and 2.8 were evaluated at $x_3 = 0.25\delta$. Streamwise integral length scale of *CHNL* was determined to be 2569 m and that of *EK10* and *EK02* were, respectively,

877 m and 265 m. Cross-stream integral length scales were, respectively, 382 m, 300 m and 160 m for the three cases. The differences among the flow cases continue to exist in spectral energy distributions.

The high energy peak in the long wavelength region or a plateau region in the longer wavelengths regime in the premultiplied spectra has primarily been the source of identification of VLSMs in channel flows [9, 13]. In Fig. 2.5, the premultiplied spectra of the velocity components are presented. The spectra are premultiplied by wavenumber and normalized by friction velocity and along the x -axes wavelength are normalized by δ . In the *CHNL* case (Fig. 2.5a), the typical high-energy peak and plateau region in the long wavelength regime can be identified from the spectra of u_1 in x_1 -direction, confirming the existence of the streamwise aligned large-scale structures along with VLSMs. The first peak, or the beginning of the plateau, corresponds to LSMs and the second peak or the end of the plateau corresponds to VLSMs. This plateau region with a slope of zero also corresponds to the -1 slope region of traditional Fourier spectra where inertial range scales are usually identified with a matching $-5/3$ slope [33, 34]. In this case of premultiplied spectra, the area under any curve corresponds to the total turbulent energy due to the streamwise velocity at a particular distance from the wall. The same common trend of decrease in turbulent energy with respect to distance from the wall is evident for all cases. It is noticeable in *CHNL* that for a height of 0.06δ , the peak appears at the wavelength of 21δ whereas, at the height of 0.45δ , the peak appears at 28δ . From the plotted lines, it is observed that the high-energy peaks corresponding to VLSMs shift towards larger wavelength up until the height of $z/\delta = 0.3$. Also, an overall shrinking plateau region is observed as the distance from the surface increases. As the height increases, the distinctive peak in the LSM region corresponding to a large amount of energy gradually ceases to exist. This indicates that in the lower portion of the BL, LSMs contribute significantly to the total energy content. All these features conform to the findings of the previous studies that probed VLSM characteristics in channel flows. However, in the case of Ekman layer flows (Fig. 5(b), 5(c)), significantly different energy distributions are observed. Instead of bi-modal, skewed mono-modal distributions with or without a clear plateau region are produced. For the *CHNL* and *EK10* cases, the highest energy peaks in the LSM regime shift towards the larger wavelengths with increasing distance from the wall. In contrast, for

the *EK02* case, the shift toward larger wavelengths is not as prominent and all of the peaks are concentrated within $\lambda_x/\delta = 1 \pm 0.2$. The observed difference in the length scales of the high-energy containing motions between the Ekman layer cases, i.e., *EK10* and *EK02*, can be attributed to the difference in the magnitude of rotation present in the flows. Also, the spectral energy distributions in *EK02* are flatter than those of the *EK10* case while at the same time, the relative energy content of LSMs diminishes significantly. This could either mean the absence of VLSMs or that their contribution to the stream-wise energy is not as pronounced as in the other cases. The tails of the spectral energy distributions show significant difference between the three cases. The *CHNL* case has a sharp fall in the energy content of the small-scale structures, while *EK10* has a gradual decline and *EK02* has an even slower decline.

On the right-hand side panels, (*a'*), (*b'*), and (*c'*) show premultiplied and normalized u_2 -spectra with respect to spanwise wavelengths (λ_2) normalized by δ . The possibility of streamwise aligned large-scale structures being washed out due to the cross-stream velocity component can be inferred from u_2 -spectra. Intense energy in the cross-stream scales would indicate such a possibility. The energy distributions in the cross-stream scales in these cases are mono-modal with or without a clear plateau. The energy distributions in cross-stream velocity scales are similar between the different cases unlike the u_1 -spectra. The high-energy peaks move towards the larger wavelength region with increasing distance from the surface. *CHNL* and *EK10* show nearly similar distribution, each with its most significant large scale being on the order of δ . At similar heights, similar length scales tend to have more energy in *EK10* compared to *CHNL*. This is due to a higher magnitude in fluctuations of the u_2 velocity component. Energy content at each scale at each horizontal level is lower in *EK02* compared to *EK10* with a notable exception at $z = 0.054\delta$. These premultiplied spectra do not provide any conclusive evidence of the absence of VLSMs in Ekman layer flows, although they do not show any evidence of their presence either. To address this issue in the next section, alternative approaches are used to identify VLSMs that involve selective filtering and alternative VLSM definitions as well as quantifying the contributions of VLSMs to the surface shear stress.

2.3.3 Filtering and Conditional Averaging

Conditional averaging was carried out with a goal of further characterizing the size and shape of VLSMs and of identifying the contribution of VLSMs to shear stress, $\tau_{x,y} = \sqrt{((u'_1 u'_3)^2 + (u'_2 u'_3)^2)}$, where $u'_1 u'_2 = (u_1 - \langle u_1 \rangle_{x,y})(u_2 - \langle u_2 \rangle_{x,y})$, and $u'_2 u'_3 = (u_2 - \langle u_2 \rangle_{x,y})(u_3 - \langle u_3 \rangle_{x,y})$ with $\langle \rangle_{x,y}$ denoting the planar average. The conditional averaging was carried out at selected wall parallel planes to characterize the flows in the wall-normal direction and to have a quantitative account of the coherent structures on horizontal planes. Many studies have examined the characteristics and contributions of coherent structures with length scales of order of δ or smaller [1]. Here, to facilitate the determination of contributions from only large-scale coherent structures, smaller flow scales that fall within the inertial sub-range of turbulence were removed by filtering. Two-dimensional spectral cut-off filtering in the horizontal plane was used and the cut-off scale was selected as the distance of the selected surface from the ground. This filtering was designed to remove all horizontal scales smaller than the scales of the energy producing eddies. A new alternative definition of planar coherent structures was adopted to facilitate our analysis. Two-dimensional coherent structures were defined as the connected region of pixels either having negative u'_1 fluctuations (low momentum) or positive u'_1 fluctuations (high momentum). The adopted definition was motivated by the commonly reported presence of VLSMs in filtered velocity fields identified through visualization [14, 35]. Visually, VLSMs appear to be long regions of low or high momentum fitting the definition assumed. Here, an objective analysis was devised using image-processing techniques to detect such long structures and quantify their spatial characteristics. In addition, to quantify the importance of a detected structure to momentum transport, the ratio of shear stress fraction and area fraction was determined. Here, horizontal transects of 3D structures were identified at different heights. To identify a 2D horizontal transect of a structure a binary version of the velocity field was created. To identify low-momentum structures, all positive streamwise velocity field fluctuations were set to zero and negative values were assigned a value of one so that on a given horizontal level

$$u'_1(x, y) = \begin{cases} 1, & u'_1 \leq 0 \\ 0, & u'_1 > 0 \end{cases} . \quad (2.9)$$

Next the binary planar image was segmented and labeled using a connected component labeling technique [36]. Spatial image moments and shape attributes for each labeled area were calculated including the centroid, area, major axis length, minor axis length, and orientation. The zeroth-order moment of a shape is the area of that shape. The ratio of first-order and zeroth-order moments yields the centroid of an image object. The major axis length is equivalent to the major axis length of an ellipse that has the same moments of inertia along the horizontal and vertical axes and also has the same moments of inertia along the principal axes. The orientation was measured as degrees of angle between the horizontal axis and the major axis of a shape. More details on spatial moments and discrete binary image shape attributes can be found in Pratt [37]. The major axis length of each labelled segment was checked against a threshold and if it was greater than a specified threshold, the segment was marked as a possible horizontal transect through a VLSM. On these marked image objects, ellipses with predetermined major and minor axes lengths were drawn with coincident centroids. All such elliptical areas in five statistically independent frames were then averaged to characterize an average footprint of a VLSM. The frames were $L_{int,x}/U_c$ (sec) apart from each other in time where the characteristic velocity U_c was taken as the mean velocity at the height of the BL. In the image segment identification process, an incremental range of length scales $(0.75n - 1.25n)\delta$ with $n = 2, 3, \dots, 24$ was used. Structures identified within each range of scales on selected horizontal levels provided cumulative measurements of the contribution to the shear stress and turbulent kinetic energy by coherent structures on those 2D planes.

To quantify the importance and contribution of VLSMs to shear stress, two quantities were calculated after averaging, the area fraction and the shear stress fraction. The total area fraction, A_f , was calculated as,

$$A_f = \sum \frac{\mathbb{N}}{\mathbb{N}_a},$$

where \mathbb{N} represents the number of non-zero pixels within an individual ellipse and \mathbb{N}_a denotes the total number of pixels in the binary image. Summation over all area fractions yielded total area fraction. The total shear stress fraction $\tau_{x,y}^f$ was calculated as,

$$\tau_{x,y}^f = \frac{\sum \langle \tau_{x,y} \rangle \mathbb{N}}{\langle \tau_{x,y} \rangle_a \mathbb{N}_a},$$

where $\langle \tau_{x,y} \rangle_a$ is the average shear stress of the wall parallel plane and $\langle \tau_{x,y} \rangle$ is that of a selected elliptical area. An example of the determination process is presented in Fig. 2.6. The image on the left-hand side shows a binarized image of the u'_1 field at the height of 0.15δ . The white regions represent negative u'_1 fluctuations and black regions represent positive velocity regions. In this picture all detected structures having lengths in the range of $\delta - 10\delta$ are shown as blue regions. On the right-hand side, a two blue regions encircled with red ellipses and marked interior points painted in blue are shown. The detected regions were characterized with the major and minor axes lengths of the bounding ellipses and the painted blue points were used as sampling points for calculating average shear stress. Finally, the ratio $\tau_{x,y}^f/A_f$ was studied to quantify the significance of the selected areas in terms of their contribution towards the shear stress.

Figure 2.7 shows cumulative density functions of the lengths of coherent structures as a function of height in the left panels along with the ratio $\tau_{x,y}^f/A_f$ in the right panels. The cumulative density functions highlight differences in the population of VLSMs existing in the u_1 -velocity fields. Between the three cases *CHNL*, shows the presence of VLSM horizontal transects as large as 30δ on a surface-parallel plane at the height of 0.66δ and similar observation can be made for *EK10* and *EK02*. However, a comparison of Figs. 2.7(a), (b), and (c) indicates that ratio of large-scale structures to small-scale structures decreases for higher degrees of rotation in the velocity field. Also evident is the fact that the large-scale structures are scarce at lower levels, i.e., in the surface layer but appear more frequently as the distance from the ground increases, i.e., outer layers. In general the number of occurrences of large-scale structures is a function of height. To get a quantitative picture of the importance of such detected structures to horizontal shear stress, $\tau_{x,y}^f/A_f$ is plotted against normalized height in Fig. 2.7(d). Due to huge differences in the number of detected structures in each band, $\tau_{x,y}^f/A_f$ in Fig. 2.7(d), average major axis length in 2.7(e), and average minor axis length in 2.7(f) at each horizontal level were calculated as the expected values. The $\tau_{x,y}^f/A_f$ ratio plot shows the importance of the structures detected in terms of their contribution to overall shear stress at the respective horizontal levels. *CHNL* shows the highest contribution to shear stress from connected regions while *EK02* shows the minimum contribution. This figure also reveals a significant fact that structures or at least the VLSM horizontal transects on surface-parallel planes do not contribute significantly to

shear stress in the surface layer. However, the authors refrain from drawing any strong conclusion from this result in the vicinity of the surface because of the use of a highly approximate modeled shear stress boundary condition in LES of the ABL. In general, as the distance from the bottom surface increases, the importance and contribution of these visually-identified long connected regions of low momentum increases gradually. The length scale of VLSMs likewise can also be observed to be a function of z in Fig. 2.7(e). Although a slight difference in the maximum average length of the structures is observed in *CHNL* and *EK10* cases, i.e., 8.19δ at a height of 0.7δ for the *CHNL* case and 8.4δ at a height of 0.65δ for *EK10* (fig. 2.7(e)), the trend in these two cases is almost identical. The shortest among the maximum average lengths appears in *EK02* as 5.95δ at a height of 0.5δ . As evident from Fig. 2.7(f), the structure width increases with height consistently. At the highest measurement height, *CHNL* shows the minimum structure width, i.e., 1.47δ , whereas *EK10* and *EK02* show 2.06δ and 2.13δ , respectively. With the introduction of rotation in the velocity field, the structures become shorter but wider.

A visual depiction of the 3D structure of the reported VLSMs as connected regions of low-momentum fluid is shown in Fig. 2.8. To determine the 3D structure, the binarized u'_1 velocity field was examined for 2D horizontal transects on the horizontal plane at $2\Delta_z$ distance away from the ground where Δ_z is the vertical grid spacing of the staggered grid. Upon identification of any connected region having a major axis length longer than a specified threshold, an enclosing 3D box was drawn centered at the centroid of the region. The 3D rectangular box extended from the bottom wall to the top of the simulation domain. The horizontal dimensions of the box in the streamwise and spanwise directions for the three different cases were estimated from the corresponding expected dimensions of the VLSMs (Fig. 2.7(d) and 2.7(e)). The horizontal box dimensions were large enough to contain the VLSMs within the box and had streamwise lengths of 15δ , 15δ , and 10δ and constant spanwise length of 2δ for *CHNL*, *EK10*, and *EK02*, respectively. The conditional averaging revealed the average 3D shape of a VLSM, which is expected from the very nature of the operation of conditional averaging. The fact that should be emphasized here is that the detection-condition was imposed only on a horizontal plane and no constraint was in place to the 3D shape or orientation. The assumption of similarity in size, orientation, and shape of the structures around the selected averaging points is inherent to the idea

of conditional averaging. If the assumptions hold true, then a 3D coherent shape would appear. Considering these facts, it can be inferred that the 3D structures obtained reveal a few characteristics of the VLSM. The conspicuous differences between VLSMs identified in each case appear in shape and dimension. For the *CHNL* case on an average, VLSMs appear to have a symmetrical cylindrical shape in the middle that gets tapered off near the ends and the length in the mean wind direction is approximately 9δ . *Ek10* case shows a structure that is slightly shorter in the mean wind direction and shows signs of rotation near the top where Ro is relatively low compared to that near the surface (see Fig. 2.3). The average length can be identified to be approximately 7δ . For the *EK02* case, a much shorter but wider structure is obtained. The effect of rotation in this case is the most prominent. The length can be identified to be approximately 5.7δ .

2.4 Conclusion

VLSMs were identified and their relative scales were compared for three different simulated flows. The simulation domain was large enough compared to the length scale of VLSMs not to impose any inhibition in the spatial development of these structures. One simulation provided the canonical channel flow case and the other two were Ekman layer simulations characterized by different degrees of rotation. Differences in the flow cases in terms of basic turbulent statistics along with the coherence were discussed. Coherence in the flows were compared in the light of correlation between different horizontal planes and integral length scales. The unidirectional constant pressure driven flow was observed to have the highest degree of coherence. The differences in coherence among the flow cases are reflected in the the determined mean length scales of the composite 3D structures of VLSMs.

Previously, VLSMs were reported for flows only where rotation did not have any significant effect. Thus, the challenges of identification of VLSMs in rotational flows were not addressed. The most common problem in identification and detection of VLSMs is the lack of a concrete definition based upon which a detection algorithm could be developed. To address this issue and to test a hypothesis that VLSMs could be identified based on the reported visual characteristics of those structures, i.e., as long streaks of low-momentum fluid primarily elongated in the streamwise direction, an alternative simple definition of

VLSM was adopted. VLSMs were defined as the long connected regions of low-momentum fluid. This definition yielded quantitatively consistent length scales of VLSMs with the same detected from premultiplied spectra for the *CHNL*. The detection of length scales of VLSMs from one dimensional premultiplied spectra quickly becomes marred as soon as rotation is introduced in the flow since distinguishable dominant peaks ceases to appear. Adopting the alternative definition and utilizing the established image processing techniques lend an effective technique of detection and measurement that works well even when rotation is introduced in the flow. This was verified by the identification of VLSMs in Ekman layer flows. A simple linear correspondence of the streamwise length scale was not observed with local Rossby number; however, it was observed that in general rotation inhibits the streamwise length scale of the VLSMs but is conducive to the increase in length scale in the cross-stream direction. The greater the influence of rotation compared to inertial acceleration, the greater the cross-stream length scale is. It was also observed that irrespective of the forcing condition, the length scale of the two dimensional planar structures was increasing in the direction normal to the ground. This result is consistent with the findings of de Silva et al. [38].

2.5 References

- [4] A. K. M. Fazle Hussain. Coherent structures and turbulence. *Journal of Fluid Mechanics*, 173, 1986.
- [5] Jacques Lewalle, Joël Delville, and Jean-Paul Bonnet. Decomposition of mixing layer turbulence into coherent structures and background fluctuations. *Flow, Turbulence and Combustion*, 64, 2000.
- [6] H.E. Fiedler. Coherent structures in turbulent flows. *Progress in Aerospace Sciences*, 25(3), 1988.
- [7] Chinthaka Jacob and William Anderson. Conditionally averaged large-scale motions in the neutral atmospheric boundary layer: insights for aeolian processes. *Boundary-Layer Meteorology*, 162(1):21–41, Jan 2017. ISSN 1573-1472. doi: 10.1007/s10546-016-0183-4. URL <https://doi.org/10.1007/s10546-016-0183-4>.
- [8] F. Kerhervé, S. Roux, and R. Mathis. Combining time-resolved multi-point and spatially-resolved measurements for the recovering of very-large-scale motions in high reynolds number turbulent boundary layer. *Experimental Thermal and Fluid Science*, 82:102–115, 2017.
- [9] M Guala, S. E. Hommema, and R. J. Adrian. Large-scale and very-large-sacle motions in turbulent pipe flow. *Journal of Fluid Mechanics*, 554:521–542, 2006.

- [10] K. C. Kim and R. J. Adrian. Very large-scale motion in the outer layer. *Physics of Fluids*, 11:417–422, 1999. doi: 10.1063/1.869889.
- [11] J. P. Monty, J. A. Stewart, R. C. Williams, and M. S. Chong. Large-scale features in turbulent pipe and channel flows. *Journal of Fluid Mechanics*, 589, 2007.
- [12] Jin Lee, Jae Hwa Lee, Jung-II Choi, and Hyung Jin Sung. Spatial organization of large- and very-large-scale motions in a turbulent channel flow. *Journal of Fluid Mechanics*, 749:818–840, 2014.
- [13] Jiannong Fang and Fernando Porté-Agel. Large-eddy simulation of very large-scale motions in the neutrally stratified atmospheric boundary layer. *Boundary-Layer Meteorology*, 155:397–416, 2015.
- [14] N. Hutchins and Ivan Marusic. Evidence of very long meandering features in the logarithmic region of turbulent boundary layers. *Journal of Fluid Mechanics*, 579: 1–28, 2007.
- [15] Jae Hwa Lee and Hyung Jin Sung. Very-large-scale motions in a turbulent boundary layer. *Journal of Fluid Mechanics*, 673:80–120, 2011.
- [16] J. R. Baltzer, R. J. Adrian, and Xiaohua Wu. Structural organization of large and very large scales in turbulent pipe flow simulation. *Journal of Fluid Mechanics*, 720, 2013.
- [17] D Chung and B. J. McKeon. Large-eddy simulation of large-scale structures in long channel flow. *Journal of Fluid Mechanics*, 661, 2010.
- [18] B. Ganapathisubramani, N. Hutchins, J. P. Monty, D. Chung, and I. Marusic. Amplitude and frequency modulation in wall turbulence. *Journal of Fluid Mechanics*, 712, 2012.
- [19] Igor N Esau. The Coriolis effect on the coherent structures in the planetary boundary layers. *Journal of Turbulence*, 4, 2003.
- [20] Rob Stoll and Fernando Porté-Agel. Dynamic subgrid-scale models for momentum and scalar fluxes in large-eddy simulation of neutrally stratified atmospheric boundary layers over heterogeneous terrain. *Water Resources Research*, 42(1), 2006.
- [21] Rob Stoll and Fernando Porté-Agel. Large-eddy simulation of the stable atmospheric boundary layer using dynamic models with different averaging schemes. *Boundary-Layer Meteorology*, 126(1):1–28, 2008.
- [22] Rob Stoll and Fernando Porté-Agel. Effect of Roughness on surface boundary conditions for large-eddy simulation. *Boundary-Layer Meteorology*, 118:169–187, 2006.
- [23] Rob Stoll and Fernando Porté-Agel. Surface heterogeneity effects on regional-scale fluxes in stable boundary layers: surface temperature transitions. *Journal of the Atmospheric Sciences*, 66(2):412–431, 2009. doi: 10.1175/2008JAS2668.1.
- [24] Brian N. Bailey and Rob Stoll. Turbulence in sparse, organized vegetative canopies: a large-eddy simulation study. *Boundary-Layer Meteorology*, 147(3):369–400, 2013. doi: 10.1007/s10546-012-9796-4.

- [25] Nathan E. Miller and Rob Stoll. Surface heterogeneity effects on regional-scale fluxes in the stable boundary layer: aerodynamic roughness length transitions. *Boundary-Layer Meteorology*, 149(2):277–301, 2013. doi: 10.1007/s10546-013-9839-5.
- [26] Brian N. Bailey, Rob Stoll, Eric R. Pardyjak, and Walter F. Mahaffee. Effect of vegetative canopy architecture on vertical transport of massless particles. *Atmospheric Environment*, 95:480 – 489, 2014. doi: <https://doi.org/10.1016/j.atmosenv.2014.06.058>.
- [27] Brian N. Bailey and R. Stoll. The creation and evolution of coherent structures in plant canopy flows and their role in turbulent transport. *Journal of Fluid Mechanics*, 789:425–460, 2016. doi: 10.1017/jfm.2015.749.
- [28] A. Andren, A. R. Brown, J. Graf, P. J. Mason, C.H. Moeng, F. T. M. Nieuwstadt, and U. Schumann. Large-eddy simulation of a neutrally stratified boundary layer: a comparison of four computer codes. *Quarterly Journal of the Royal Meteorological Society*, 120:1457–1484, 1994.
- [29] J. Cuxart, Holtslag A.A.M., R.J. Beare, E. Bazile, A. Beljaars, A. Cheng, L. Conangla, M. Ek, F. Freedman, R. Hamdi, A. Kerstein, H. Kitagawa, G. Lenderink, D. Lewellen, J. Mailhot, T. Mauritsen, V. Perov, G. Schayes, G-J. Steeneveld, G. Svensson, P. Taylor, W. Weng, S. Wunsch, and K-M. Xu. Single-column model intercomparison for a stably stratified atmospheric boundary layer. *Boundary-Layer Meteorology*, 118(2), 2006.
- [30] J. R. Garrat. *The atmospheric boundary layer*. Cambridge University Press, 1992.
- [31] Elie Bou-Zeid, Charles Meneveau, and Marc Parlange. A scale-dependent lagrangian dynamic model for large eddy simulation of complex turbulent flows. *Physics of Fluids*, 17(2):025105, 2005. doi: 10.1063/1.1839152. URL <https://doi.org/10.1063/1.1839152>.
- [32] K. Träumner, Th. Damian, Ch. Stawiarski, and A. Wieser. Turbulent structures and coherence in the atmospheric surface layer. *Boundary-Layer Meteorology*, 154:1–25, 2015.
- [33] A. E. Perry, S. Henbest, and M. S. Chong. A theoretical and experimental study of wall turbulence. *Journal of Fluid Mechanics*, 165:163–199, 1986.
- [34] Seyed G. Saddoughi and Srinivas V. Veeravalli. Local isotropy in turbulent boundary layers at high reynolds number. *Journal of Fluid Mechanics*, 268:333–372, 1994. doi: 10.1017/S0022112094001370.
- [35] David J. C. Dennis and Timothy B. Nickels. Experimental measurement of large-scale three-dimensional structures in a turbulent boundary layer. part 2. long structures. *Journal of Fluid Mechanics*, 673, 2011.
- [36] E. R. Davies. *Computer and machine vision : theory, algorithms, practicalities*. Elsevier/Academic Press, 2012.
- [37] William K. Pratt. *Introduction to digital image processing*. CRC Press, Taylor & Francis Group, 2014.
- [38] Charitha M. de Silva, Nicholas Hutchins, and Ivan Marusic. Uniform momentum zones in turbulent boundary layers. *Journal of Fluid Mechanics*, 786:309–331, 2016.

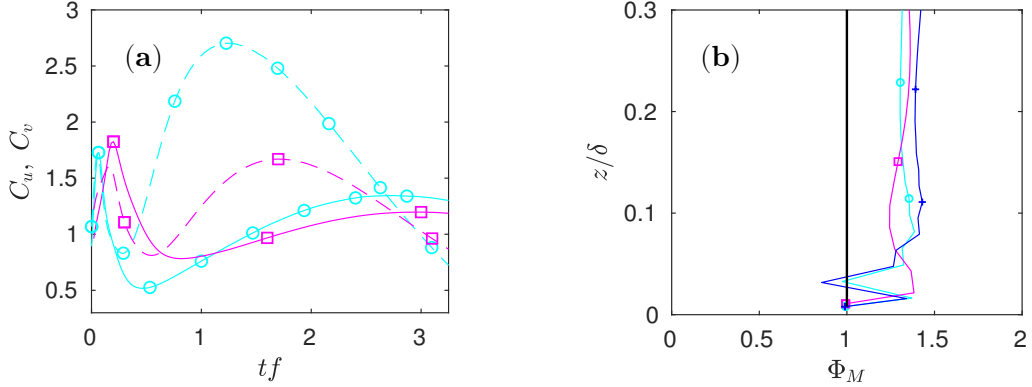


Figure 2.1. Measurement of unsteadiness in the mean flow and the profile of vertical gradient. (a). C_u, C_v plotted against non-dimensional time tf for EK10 and EK02. Solid lines correspond to C_u and dotted lines to C_v . (b). Nondimensional vertical gradient of mean streamwise velocity, $\Phi_M = \kappa z u_*^{-1} d \langle \bar{u} \rangle / dz$ plotted as a function of nondimensional height. Lines with markers +, o, □ correspond to CHNL, EK10, and EK02, respectively. The solid black line corresponds to the classical log law expected to hold in the surface layer.

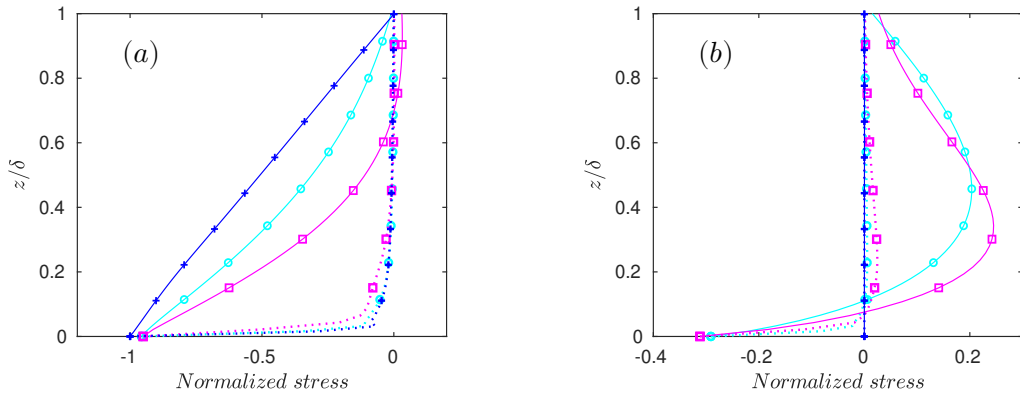


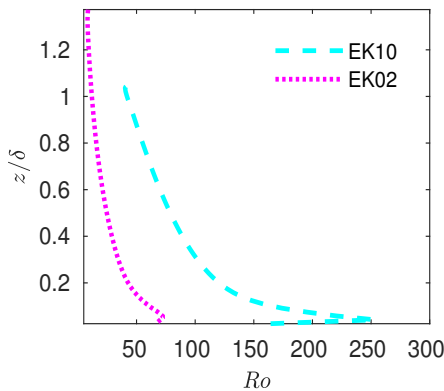
Figure 2.2. Normalized vertical profiles of time and horizontally averaged resolved and SGS stresses. (a) $\langle \bar{u}_1' \bar{u}_3' + \tau_{13} \rangle$ and τ_{13} plotted as a function of height normalized by boundary layer height (δ) for cases EK10, EK02, and CHNL. Solid lines correspond to $\langle \bar{u}_1' \bar{u}_3' + \tau_{13} \rangle$ and dotted lines correspond to τ_{13} . (b) $\langle \bar{u}_2' \bar{u}_3' + \tau_{23} \rangle$ and τ_{23} plotted as a function of normalized height for cases EK10, EK02, and CHNL. Solid lines correspond to $\langle \bar{u}_2' \bar{u}_3' + \tau_{23} \rangle$ and dotted lines to τ_{23} . Line types $-o-$, $-□-$ and $-+--$ correspond to EK10, EK02, and CHNL, respectively.

Table 2.1. Simulation parameters and flow characteristics

	N_1/N_2	N_3	$L_1/L_2(\text{Km})$	$L_3 (\text{Km})$	$\delta(\text{m})$	Ro
<i>CHNL</i>	2048	64	128	1.5	0	1500.00
<i>EK10</i>	2048	64	128	1.5	2	1433.00
<i>EK02</i>	2048	64	128	0.75	2	550.69

Table 2.2. Fraction of the cumulative energy contained by all the spatial scales greater than the specified threshold at a height of $x_3 = 0.45\delta (\pm 0.01\delta)$ for the u_1 -component in the x_1 -direction

Threshold	δ	3δ	5δ	7δ	9δ	11δ
<i>CHNL</i>	0.841	0.633	0.524	0.461	0.416	0.383
<i>EK10</i>	0.771	0.490	0.356	0.278	0.227	0.190
<i>EK02</i>	0.693	0.396	0.283	0.220	0.178	0.146
Threshold	13δ	15δ	17δ	19δ	21δ	23δ
<i>CHNL</i>	0.359	0.339	0.320	0.305	0.290	0.277
<i>EK10</i>	0.167	0.147	0.130	0.116	0.105	0.096
<i>EK02</i>	0.122	0.105	0.090	0.079	0.070	0.064

**Figure 2.3.** Vertical Rossby number profile of *EK10* and *EK02* plotted as a function of normalized height.

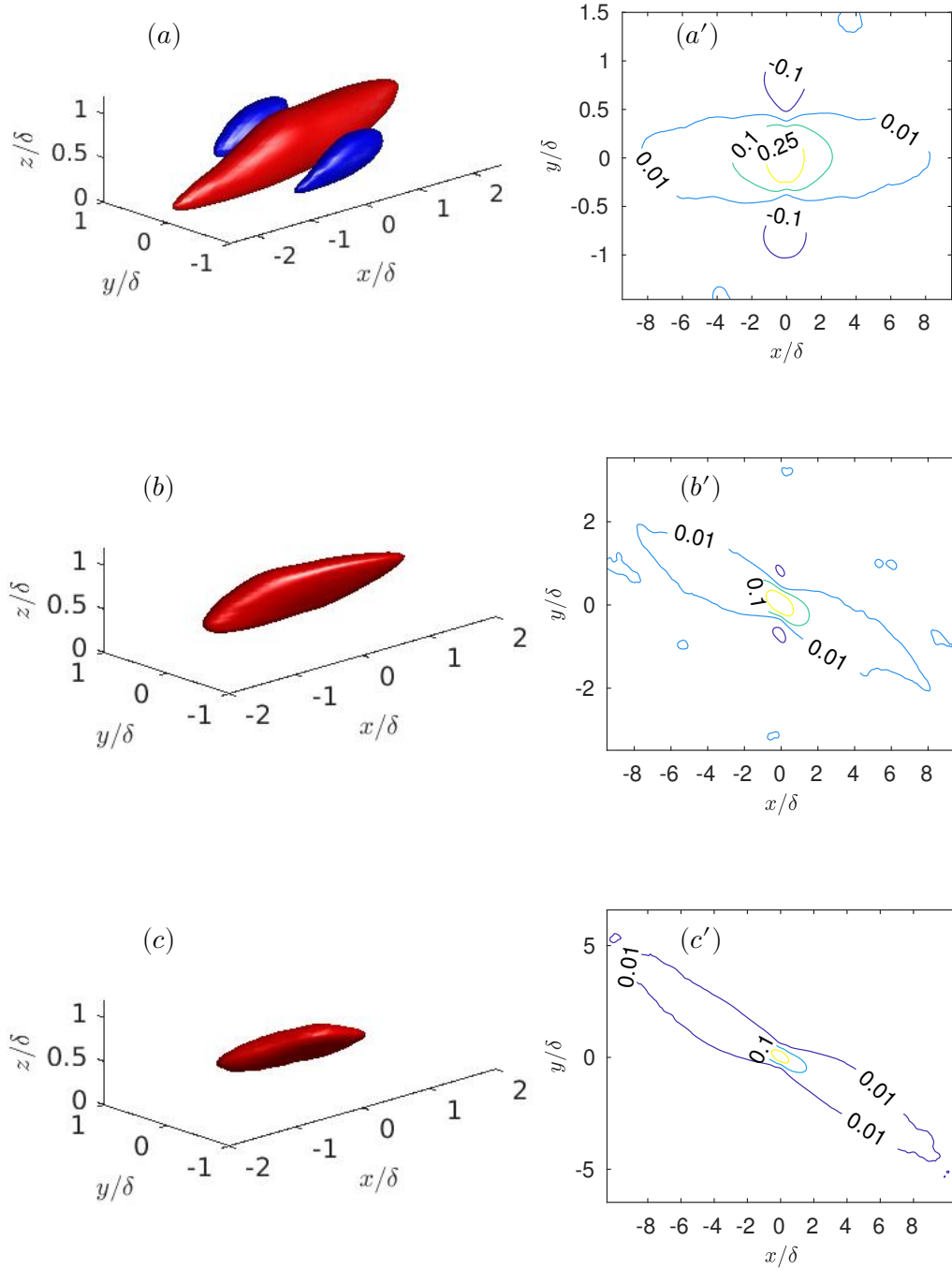


Figure 2.4. Correlation of u-velocity component. (a), (b), (c) show correlation of reference level $z/\delta = 0.5$ with all other horizontal levels as defined by equation 2.5 for *CHNL*, *EK10*, and *EK02*, respectively. Red iso-surfaces denote correlation greater than or equal to 0.25 and blue iso-surfaces show negative correlation, smaller or equal to -0.15 . (a'), (b'), (c'). show planar autocorrelation, R_{uu}^{2D} of *CHNL*, *EK10*, and *EK02* at $x_3 = 0.5\delta$, respectively.

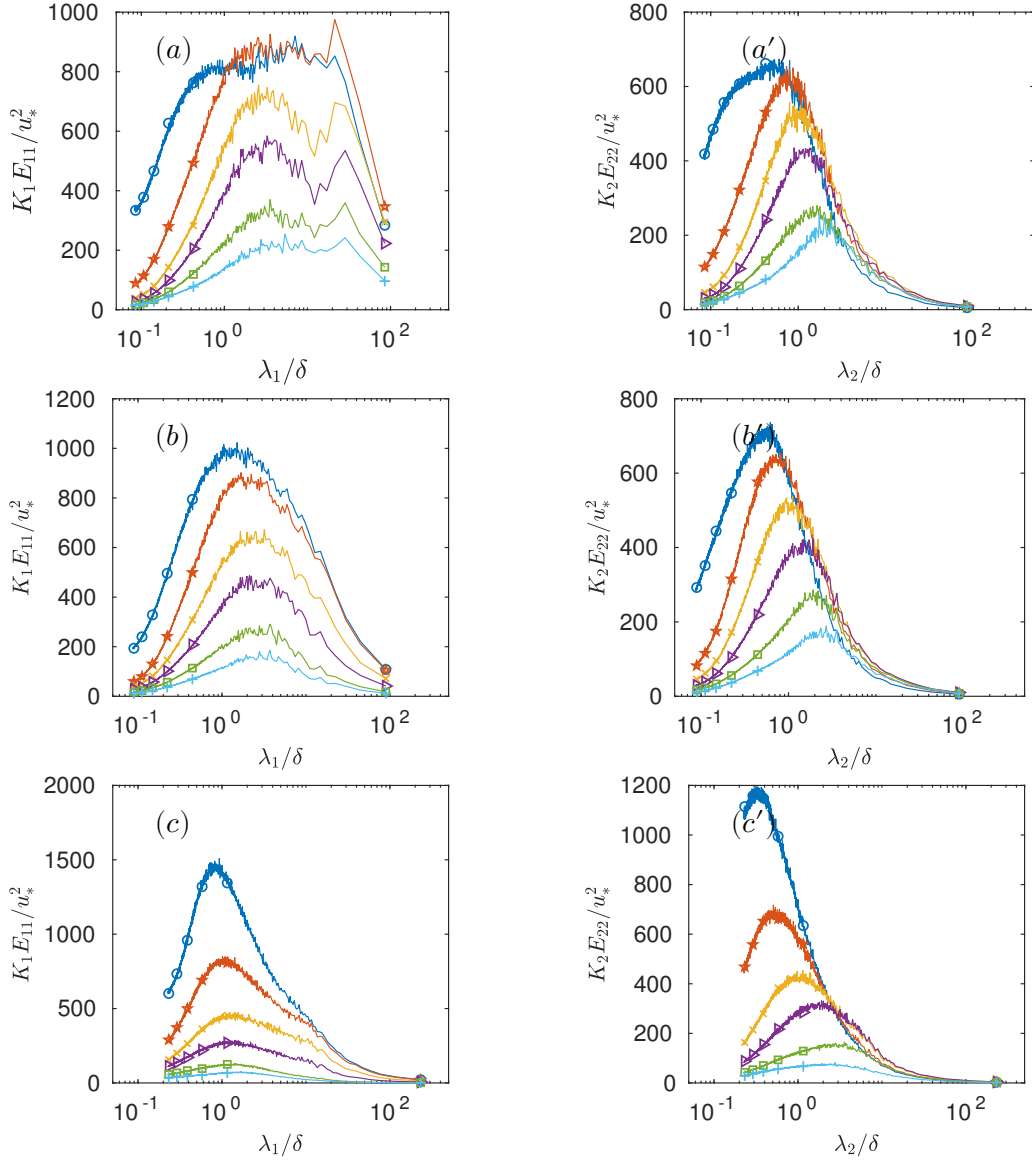


Figure 2.5. Premultiplied velocity spectra against normalized wavelengths are shown for different cases. (a), (b), (c) show spectra of the u -component of the velocity for CHNL, EK10, and EK02, respectively. (a'), (b'), (c') show spectra of the v -component of the velocity for CHNL, EK10, and EK02, respectively. Curves marked with (\circ , \times , \square , \circlearrowleft , $+$) correspond to heights $x_3/\delta = (0.06, 0.15, 0.30, 0.45, 0.71, 0.90) \pm 0.01$, respectively.

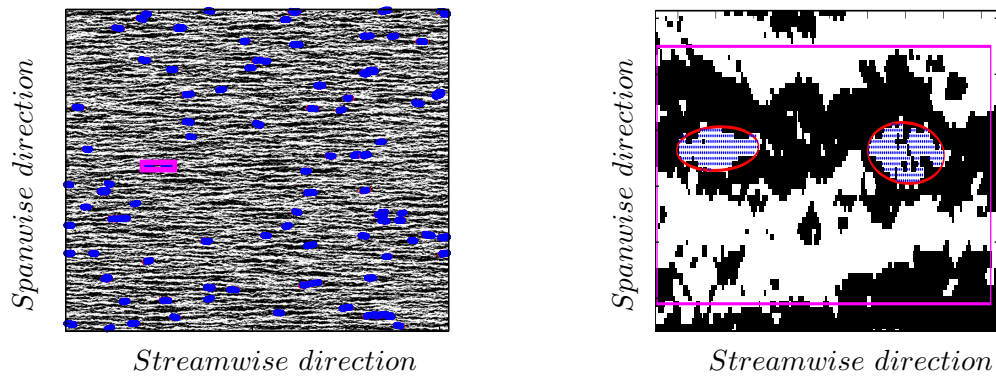


Figure 2.6. Identification of VLSMs. (Left) For the *CHNL* case, a cropped binarized negative u' velocity field image is shown which is overlayed with detected elliptical coherent structures with a range of major axis length lengths, $\delta - 10\delta$. (Right) Zoomed-in two detected structures with interior points painted in blue where average shear stresses were calculated are shown. Horizontal and vertical axes are aligned with streamwise and spanwise directions, respectively

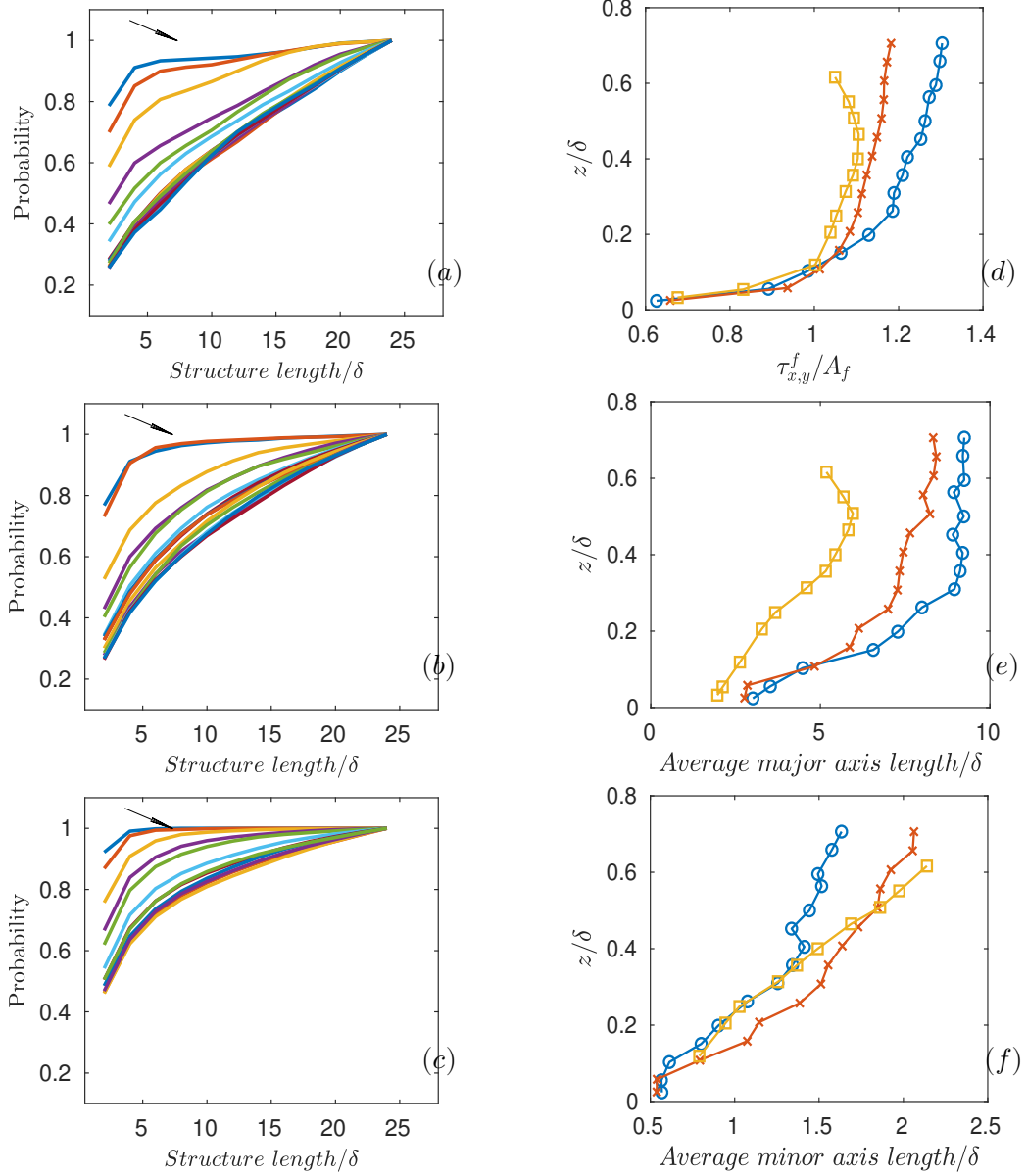


Figure 2.7. Cumulative density function of coherent structure lengths, their aggregate contribution to shear stress as functions of height, and their average lengths. The left panel shows cumulative density function of the structure lengths detected in the range $\delta - 25\delta$ for *CHNL* (a), *EK10* (b), and *EK02* (c) cases. The arrows point to the direction of increasing distance from the surface. The panel on the right-hand side shows the ratio (d) $\tau_{x,y}^f/A_f$ plotted for different wall normal locations of all cases. (e) shows the mean length of major axes for all structures detected and (f) shows the mean minor axes lengths. Here (—○—) represents *CHNL*, (—×—) represents *EK10*, and (—□—) represents *EK02*.

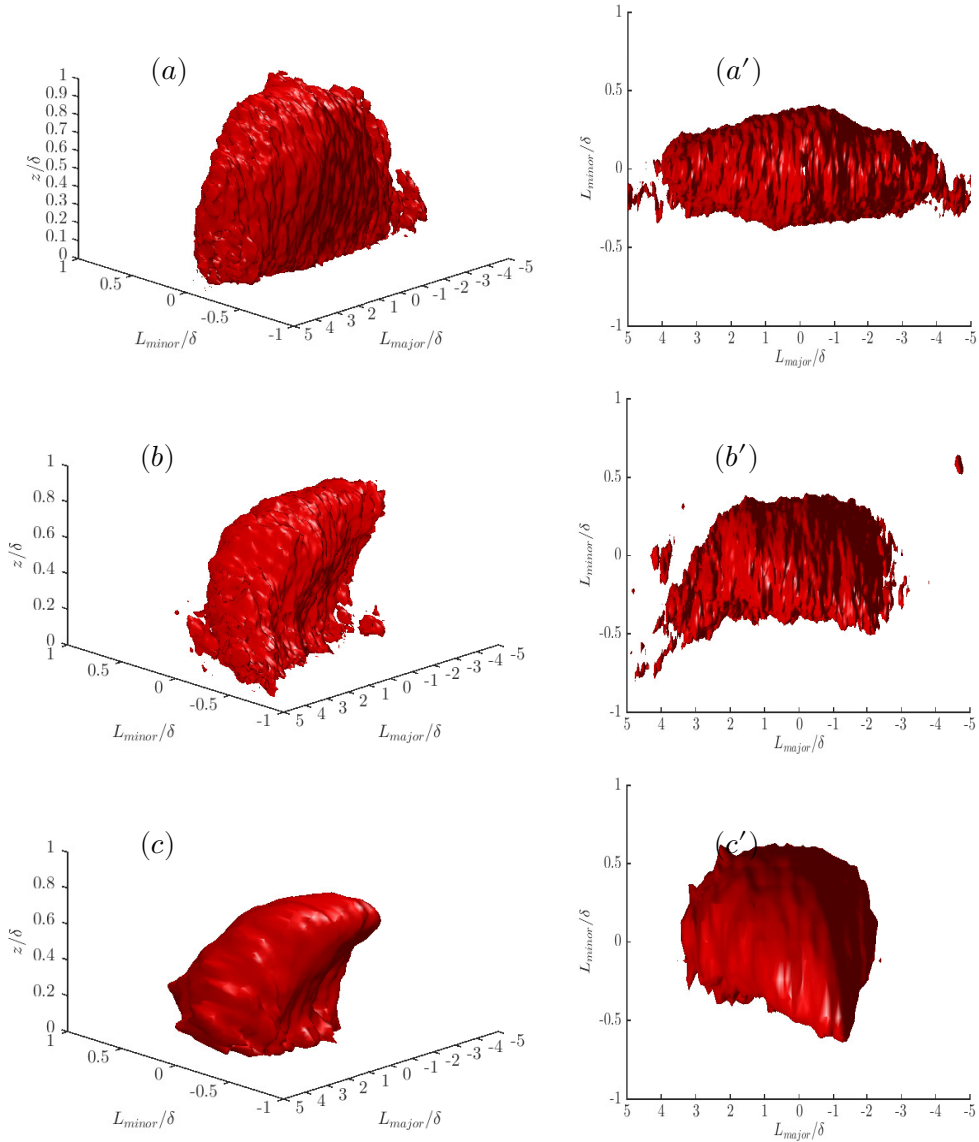


Figure 2.8. 3D structures of VLSMs. (a), (b), (c) show the average 3D structures projected from detected 2D transects at the height of the first vertical grid point for the *CHNL*, *EK10* and *EK02* cases, respectively. (a'), (b'), (c') show the top view of the same 3D structures as shown on the left panels. Iso surfaces enclose values less than $\langle u \rangle - 1.5\sigma_u$

CHAPTER 3

MODULATION BY VERY LARGE SCALES AND SCALE-SCALE ENERGY TRANSFER TO AND FROM LARGE-SCALE MOTION

The existence of large and very large scale motions (LSMs/VLSMs) in the ABL was reported in previous studies. It was also reported from experimental studies that the large-scale motions modulate the small scales. However, the possible influence of large scales over small scales due to nonlocal turbulent kinetic energy (*tke*) exchange was not examined. Also, the mechanism of spatial development of VLSMs was speculated mostly from visualization of flow features and was not examined in the light of *tke* exchange. It can be expected that the formation mechanism of LSMs and VLSMs will have some signatures in the energy exchange process between individual scales as governed by the nonlinear term of the Navier-Stokes equations. Here, the modulation effect of large scales on smaller scales is interrogated in the simulated flow fields and the energy exchange between different scales has been explored in the wavelet domain. It has been observed that the energy exchange is not influenced by the presence of VLSMs or different forcing conditions in the examined cases and *tke* exchange is predominantly local. However, support has been found from the interscale energy exchange process in favour of the hypothesis that LSMs concatenate to give rise to VLSMs.

3.1 Introduction

Many studies have confirmed the existence of Large-Scale and Very Large-Scale Motions (LSMs and VLSMs) throughout the boundary layer in pipe [39, 40, 41], channel [39, 42, 43, 44, 45], and zero pressure gradient boundary layer flows [42, 44, 46]. Flow structures corresponding to LSMs and VLSMs can be visually identified in an instantaneous flow field as long streaks of low momentum primarily oriented along the streamwise direction and flanked by similarly shaped high-momentum regions on either side. These structures scale with outer length scales δ , where δ denotes boundary layer depth, channel half height, pipe

radius, etc. depending upon the flow. Monty et al. [39] measured streamwise velocity with hot wire rakes in a pipe and in a channel and reconstructed the spatial velocity field using Taylor's frozen turbulence hypothesis to visually identify VLSMs. In their study, they observed VLSMs of the order of 25δ in the log layer. Using a similar hot wire apparatus, Hutchins and Marusic [44] also visually identified VLSMs in the log layer of a wind tunnel boundary layer and reported length scales to be found of the order of 20δ . They also reported the existence of VLSMs in the buffer layer through their studies of DNS data of channel flow and speculated that correlations likely exist between log-layer-VLSMs and buffer-layer-VLSMs. Using stereoscopic particle image velocimetry data in conjunction with the application of Taylor's frozen turbulence hypothesis, Dennis and Nickels [47] constructed a 3D velocity field from data collected in a water tunnel and showed the 3D structure of VLSMs through a series of iso-surface plots. VLSMs were shown to be low-speed (or high-speed) turbulent bulges inclined with respect to the wall and mainly elongated in the streamwise direction that extend from the wall towards the outer region in the wall-normal direction [47]. Other studies have come to similar conclusions [48, 49].

Studies on VLSMs and LSMs are plagued by a lack of an objective definition of these large-scale motions. All visual detection procedures are subjective in nature and a threshold value has to be chosen while visualizing low-momentum or high-momentum regions. Dennis and Nickels [47] appropriately pointed out that choosing a higher threshold may result in underestimation of length of these long structures while inappropriate filtering may smooth away small-scale structures and join smaller structures to give an impression of a single large-scale structure. A more objective definition or detection criteria of the length scales of VLSMs comes from premultiplied 1D spectra of the streamwise velocity component. A bimodal distribution of energy is observed in the premultiplied spectra, where the low wavenumber peak corresponds to VLSMs and the most energy containing relatively large wavenumber mode before a sharp fall-off corresponds to LSMs. This observation of the bimodal distribution has been used to distinguish the two length scales, i.e., LSM and VLSM [40, 42, 50]. However, this scale identification from 1D spectra is not devoid of pitfalls. Hutchins and Marusic [44] pointed out that the meandering nature of the VLSM can cause a shift of the energy peak in premultiplied spectra to shorter wavelengths. Also the approach of extracting a dominant wavelength from energy spectra of the streamwise

velocity component to identify VLSMs has an inherent assumption [41] that spatially a low-momentum region would be in immediate vicinity of a high-momentum region of similar length scale in the streamwise direction and, since a VLSM structure represents only a half cycle of a sinusoidal function, the low wavenumber peak in spectra would be indicative of twice the length scale of the VLSM. The issues have been reflected as discrepancies on reported length scales of VLSMs from the premultiplied spectra and visualisation methods. In logarithmic regions of channel and boundary layer flows energy peaks corresponding to wavelengths 7.5δ and 5δ have been reported [42], whereas VLSM length scales of the order of 10δ have been reported from visualizations in both cases [43, 44, 46]. We feel the need for an alternative approach to asses the importance of VLSMs along with the identification of the probable length scale.

The wavelet framework offers an alternative approach to look at scale-dependent energy transfers and deduce the important length scales of turbulent dynamics. The most pursued way of analysing scale-to-scale energy transfer involves studying triadic interaction between scales coupled through the nonlinear term in the Fourier domain. Fundamentally, this approach is decoupled from spatial-transport phenomena and the analysis can assess interactions only in a global sense from a spatial point of view due to the nonlocality of sinusoidal functions. The other approach is to study the interaction among scales in both physical space and length scale space utilising structure functions. In this approach, one attempts to analyze the terms of a diagnostic equation of the turbulent kinetic energy (*tke*) budget derived from the second-order structure function as outlined by Hill [51]. Marati et al. [52] studied an inhomogeneous wall bounded flow using the formulation sketched by Hill [51]. However, this approach is limited in exploring the length scales bounded by integral-length scales since, structure functions lose physical significance when the auto-correlation drops to a nonsignificant value.

In this study, we focus on scale-scale energy transfers associated with VLSMs in the atmospheric boundary layer (ABL). The ABL is distinguished from laboratory-scale flows due to the presence of a diurnally varying buoyancy force and the Coriolis force. Previous studies analyzed length scales of LSMs and VLSMs and the probable mechanisms of their organization, but the question whether weak rotation of the reference frame and atmospheric stability (buoyancy) affects the length scales and organization of these structures

remained unanswered. In order to study the effect of Coriolis force on VLSMs, a very large domain of the order of 100δ is desirable given that VLSMs can span a length of 10δ . Such requirements poses a fundamental predicament to the DNS approach. Multipoint experimental measurements over such a large domain is also prohibitive, if not impossible. The most practical solution is offered by the large eddy simulation (LES) technique that was used for this study. In order to study two different regimes of large scales and to identify and differentiate their dynamics and significance, a boundary must be delineated between the two regimes of large scales, i.e., LSM and VLSM. We assume that the demarcation scale between LSMs and VLSMs is $\pi\delta$ corresponding to $k_x\delta = 2$ following Guala et al. [40]. Since the subjects of this study are VLSMs and LSMs along with the impact of the earth's rotation on them, simulation of very large flow fields was required. To properly resolve length scales as large as 20δ , we chose a domain large enough that these large scales were properly captured as structures advecting freely through the flow field. The possibility that LSMs and VLSMs interact with smaller scales nonlocally is also explored. First, we briefly describe the simulation methods and basic flow properties (Sec. 3.2) and continue with an assessment of the modulating influence of VLSMs on smaller scales as observed from our numerical data set (Sec. 3.3). Section 3.4 presents the results obtained from analysis of interscale energy transfers in the wavelet domain with a brief introduction to the wavelet method and relevant discussion on LSMs and VLSMs. Finally, we wrap up with a discussion on probable mechanics of developing VLSMs from smaller scale motions.

3.2 Large Eddy Simulations

Three different flow cases were simulated for this study designated as *CHNL*, *EK10*, and *EK02*. *CHNL* is a classic high Reynold's number channel flow simulation over a large horizontal domain where the flow is sustained by a mean pressure gradient applied across the streamwise (x) direction. The mean flow velocity vector in this case points to x-direction. Turbulence is fed off the mean velocity due to instabilities [53]. The velocity component that contributes most to the turbulent kinetic energy (*tke*) is the x-component of the velocity (u_1) and contribution of the spanwise velocity (u_2) to the *tke* is insignificant, unlike in *EK10* and *EK02*. *EK10* and *EK02* are simulations of Ekman layer flows with geostrophic wind velocities (U_g) of 10 m/s and 2 m/s, respectively (Table 4.1). A geostrophic wind

condition refers to the balance between the Coriolis force and the mean pressure gradient ($\rho^{-1} \frac{\partial \langle p \rangle}{\partial x_i} = f_c \epsilon_{ij3} \tilde{u}_j$) under horizontal homogeneity, and a zero wall-normal stress boundary conditions at the top edge of the BL. Consequently, at the top of the BL, the momentum equation for the z-direction reduces to, $\frac{\partial \langle p \rangle}{\partial z} = 0$. In terms of forcing, the key difference between the simulated channel and Ekman cases in this study is that, in *CHNL*, a constant $\langle \rho^{-1} \frac{\partial P}{\partial x} \rangle$ sustains the flow while in *EK10* and *EK02* a constant $\langle \rho^{-1} \frac{\partial p}{\partial y} \rangle = -f_c U_g$ is acting on the flow, where f_c is the Coriolis parameter. Effectively, the Ekman layer flows are constant pressure gradient flows in a rotating frame of reference.

All three simulations were carried out in a LES framework where the spatially filtered Navier-Stokes equations for an incompressible flow in the ABL were solved in conjunction with a subgrid-scale stress model. The model equations can be expressed as:

$$\frac{\partial \tilde{u}_i}{\partial x_i} = 0, \quad (3.1)$$

$$\frac{\partial \tilde{u}_i}{\partial t} + \frac{\partial \tilde{u}_i \tilde{u}_j}{\partial x_j} = \frac{-\partial \tilde{p}^*}{\partial x_i} - \frac{\partial \tau_{ij}}{\partial x_j} + f_c \epsilon_{ij3} \tilde{u}_j, \quad (3.2)$$

where $i = 1, 2, 3$ corresponds to x, y, z directions, respectively, $\tilde{\cdot}$ denotes spatial filtering, \tilde{u}_i denotes the spatially filtered velocity component in the i -direction, $\tilde{p}^* = \frac{1}{\rho} \tilde{p} + \frac{1}{3} \tau_{kk}$ is the modified, filtered pressure, the Coriolis parameter has a prescribed value of 10^{-4} , and τ_{ij} is the modelled subgrid-scale stress tensor defined as $\tau_{ij} = \tilde{u}_i \tilde{u}_j - \tilde{u}_i \tilde{u}_j$. τ_{ij} was modeled with a scale-dependent Lagrangian dynamic subgrid-scale model. Further details of the subgrid-scale model can be found in Stoll and Porté-Agel [54]. The LES code used in this study is pseudo-spectral in nature and uses a Cartesian, staggered grid. Horizontal derivatives are calculated in spectral space while in the surface-normal direction, a second-order-accurate finite-difference approximation is used. Dealiasing was applied through the 3/2 rule, the lateral boundary conditions were periodic, and the top of the domain utilized a stress free condition, i.e., $\partial \tilde{u}_1 / \partial x_3 = \partial \tilde{u}_2 / \partial x_3 = 0$ and the velocity fields were kept divergence free by pressure-correction through the solution of the Poisson equation for the pressure. All three simulations were run for long enough time to reach a quasi-steady condition. At the wall, instantaneous surface shear stresses, $\tau_{i3,s}(x, y, t)$, were needed as part of the boundary condition, and were computed as a function of the resolved scale velocities \tilde{u}_1 and \tilde{u}_2 at the lowest vertical nodes at a height of $\Delta_z/2$. This was done using Monin-Obukhov similarity theory as follows:

$$\tau_{i3,s}(x, y, t) = - \left[\frac{\tilde{u}_r(x, y, z, t) \kappa}{\ln(z/z_o)} \right]^2 \frac{\tilde{u}_i(x, y, z, t)}{\tilde{u}_r(x, y, z, t)}, \quad (3.3)$$

where κ is the von Kármán constant ($= 0.4$) and z_o is the local aerodynamic roughness length which was assumed to be 0.1 m in the simulated cases. The code has been used to simulate the ABL under a variety of different forcing conditions [e.g., 55, 56, 57] and to examine the structure and evolution of turbulent motions [e.g., 58, 59]. Its excellent representation of SGS momentum fluxes [54] makes it ideal for an examination of large-scale velocity-field dynamics. In the horizontal directions (x, y), the extents of the domains (L_x, L_y) were 128 Km and in the vertical direction (z), 1.5, 1.5, and 0.75 Km for *CHNL*, *EK10*, and *EK02*, respectively (Table 4.1). To decouple the effect of the Coriolis force from other typical atmospheric conditions such as buoyancy, neutral atmospheric conditions were assumed in all three cases and the effects of rotation were subsequently evaluated. By varying the geostrophic wind velocity, different degrees of rotational effects were observed.

The filter scales Δ_x and Δ_y were the same in the horizontal directions x and y , respectively. We took the filtered equations and decomposed the dependent variables further into horizontally averaged ($\langle \zeta \rangle$) and fluctuating components (ζ'), where ζ stands for any of the dependent variables. For convenience, the tilde will be dropped and all dependent variables will be understood as spatially filtered quantities. With the proposed decomposition and under the assumption that this horizontal averaging over statistically independent frames conforms to Reynold's averaging, the transport equation for the turbulent kinetic energy (q) takes the following form:

$$u'_3 u'_i \frac{\partial \langle u_i \rangle}{\partial x_3} + [\langle u_j \rangle \frac{\partial q}{\partial x_j} + u'_j \frac{\partial q}{\partial x_j} + \frac{\partial}{\partial x_j} (u'_i \tau'_{ij})] + u'_i \frac{\partial p'}{\partial x_i} + u'_i \frac{\partial \langle p \rangle}{\partial x_i} + u'_i \frac{\partial \langle \tau_{i3} \rangle}{\partial x_3} - \tau'_{ij} s'_{ij} = 0, \quad (3.4)$$

where, $q = \frac{1}{2} u'_i u'_i$ and $s'_{ij} = \frac{1}{2} (\frac{\partial u'_i}{\partial x_j} + \frac{\partial u'_j}{\partial x_i})$. In Equation A.5, the first term on the left-hand side denotes production of *tke* by mean shear, the second term captures the spatial redistribution of *tke* by the mean flow and turbulence, and the third and fourth terms denote velocity and pressure correlation. The fifth term stands for redistribution of *tke* by horizontally averaged subgrid-scale turbulence, and the last term denotes subgrid-scale dissipation by turbulent motions. Although, this equation of *tke* transport will not be directly analysed in this study, it will serve as a guidepost for the inter-scale energy transfer analysis. In this study a scale dependent version of the combined terms

$(-\frac{\partial}{\partial x_i} \langle p' u' \rangle - u'_j \frac{\partial \langle q \rangle}{\partial x_j} - \frac{\partial}{\partial x_j} \langle u'_i \tau'_{ij} \rangle + \langle \tau'_{ij} s'_{ij} \rangle)$ was analysed via a discrete wavelet framework. Before analysis of the interscale energy exchange, the characteristics of VLSMs are examined to confirm that the same modulating characteristics of VLSMs are observed in simulated flows as was observed in experimental analysis.

3.3 Modulation of Small Scale Fluctuations by VLSMs

One of the most important identified features of VLSMs is their modulating influence on small scales. Although the precise mechanism of how this modulation takes place has not been definitely identified, through statistical analysis of small-scale fluctuations within an envelope of large-scale fluctuations, the influence can be verified and quantified. Mathis et al. [60] conducted tests on the modulating influence of VLSMs on small scales from multipoint measurements in the boundary layer. This was done by isolating the low-frequency envelope of high-frequency (small scale) fluctuations with an application of the Hilbert Transformation and correlating the filtered envelope with the appropriately matched VLSM signal in the near-wall region. A clear signature of long wavelength motions in the log layer modulating smaller scale motions in the roughness sublayer was shown. Bernardini and Pirozzoli [61] expanded upon the analysis of Mathis et al. [60] and calculated two-point correlations between the small wavenumber envelope of high-wavenumber fluctuations and large-scale fluctuations to demonstrate the appearance of a secondary peak in the amplitude-modulation covariance map. The secondary peak corresponded to long wavelengths and the findings solidified the basic conclusions of Mathis et al. [60] and Ganapathisubramani et al. [62], hereafter referred to as GH12. GH12 also looked into the amplitude modulation imparted by VLSMs in a high Reynolds number wind tunnel boundary layer utilizing a traversing hot-wire probe. A conditional analysis of small-scale motions as reported in GH12 proved that the amplitude, frequency, and phase of small-scale fluctuations are linked to the same variables of large-scale fluctuations. We adopted the analysis method of GH12 and explored the modulating effect of large-scale motions for the simulation data sets. Results have been compared with that of GH12 to verify whether LSMs and VLSMs, as detected in the simulation data sets, exhibit similar effects. For the sake of completeness, a brief description of the analysis is furnished here. For a complete description of the methods, GH12 should be consulted where a descriptive illustration is

also presented. The key difference from the analysis of GH12 is that we analyze spatial data whereas, in GH12, the analysis was done on time-series data. To keep the analysis in line with a point measurement of a time series, we treat each streamwise row of the u_1 -component of the velocity and turbulent stress ($u'_1 u'_3$) as a single data series. Thus, on the 2048×2048 horizontal grid used here, we get 2048 independent data series at each wall-normal location on the simulation grid. Four independent instantaneous snapshots of the flow field were taken for each case, thus providing a total of 8192 data sets on each horizontal plane. A brief description of the procedure is summarized below:

- (i) The fluctuating streamwise velocity component ($u'_1(z)$) was separated by subtracting the horizontally averaged velocity ($\langle u_1(z) \rangle$) from each wall-normal plane from the instantaneous velocity fields.
- (ii) The large-scale component of the fluctuating velocity field ($u_L(z)$) was obtained by filtering $u'(z)$ with a spectral cut-off filter where the cut-off wavelength was 2δ (the red smooth line as shown in Fig. 3.1). The small-scale fluctuating component was obtained as: $u_s(z) = u'(z) - u_L(z)$ (the cyan dotted line in Fig. 3.1).
- (iii) In each data, set the series of $u_s(z)$ and $u_L(z)$ were divided into segments of length 2δ . Similar segmentation was applied to the turbulent stress ($u'_1 u'_3(z)$) series. Statistics in each individual segment were linked to the representative large-scale fluctuation values.
- (iv) Large-scale fluctuations were then categorized by a binning process based on the centre value of $u_L(z)$ from each segment of length 2δ as described in step (iii) and as shown with a hypothetical binning in Fig. 3.1. This process links each individual segment of small-scale data to a $u_L(z)$ bin. In other words, this process gives statistics of small scales conditioned on $u_L(z)$. The number of occurrences of $u_L(z)$ in each bin $N[u_L(z)]$ was counted for all data sets.
- (v) In each segment of small scales (u_s), the following statistics were calculated:
 - (1) The relative variance of the small scales $\Delta u_s^2(u_L, z)$ as:

$$\Delta \langle u_s^{2+} \rangle = \frac{\langle u_s^2(u_L, z) \rangle_S - \langle u_s^2(u_L = 0, z) \rangle_S}{\langle u_s^2(u_L = 0, z) \rangle_S} \times 100, \quad (3.5)$$

where $\langle u_s^2(u_L, z) \rangle_S = \frac{\sum u_s^2(z)|_{u_L(z)}}{N[u_L(z)]}$ and $\langle u_s^2(u_L = 0, z) \rangle_S$ denotes $\langle u_s^2(u_L, z) \rangle_S$ corresponding to the $u_L = 0$ bin.

- (2) The average wavenumber of the small-scale fluctuation. This was calculated by counting the number of zero-crossings (N_m) and then dividing by 2 ($N_m/2$). Finally, a mean representative wavenumber was calculated as:

$$\langle k_x | u_L \rangle = \frac{\sum k_x(z)}{N[u_L(z)]}, \quad (3.6)$$

where $\sum k_x$ refers to the summation of the average k_x values of all data sets corresponding to an individual $u_L(z)$ bin on a horizontal plane.

- (3) At different surface-parallel planes the mean $\langle u'_1 u'_3 \rangle$ and variance $\sigma_{u'_1 u'_3}^2$ (of the wall-normal stress ($u'_1 u'_3$)) for each bin were calculated. Finally, a combined mean $\langle u'_1 u'_3 \rangle_{u_L}$ and a pooled standard deviation ($\sigma_{u_L}^{u'_1 u'_3}$) corresponding to each u_L bin was calculated as:

$$\langle u'_1 u'_3 \rangle_{u_L} = \frac{\sum \langle u'_1 u'_3 \rangle N_S}{\sum N_S} \text{ and} \quad (3.7)$$

$$\sigma_{u_L}^{u'_1 u'_3} = \sqrt{\frac{\sum [\sigma_{u'_1 u'_3}^2 + (\langle u'_1 u'_3 \rangle - \frac{\sum \langle u'_1 u'_3 \rangle}{\sum N_S})^2 N_S]}{\sum N_S}} \quad (3.8)$$

where the summation (\sum) was taken over all segments of the data series on a horizontal plane, corresponding to a single u_L bin. N_S refers to the number of data points in a segment.

Figure 3.2 shows the strength of small-scale fluctuations conditioned on the magnitude of the fluctuation of large scales, in a relative sense, $\Delta \langle u_s^{2+} \rangle$. The large-scale modulation is measured relative to the weakest large-scale fluctuation corresponding to $u_L = 0$, which effectively represents ‘unmodulated information’. To facilitate the comparison between the three cases, u_L values have been normalized by corresponding friction velocity u_* . Any positive change in $\Delta \langle u_s^{2+} \rangle$ should be understood as a percentage amplitude amplification relative to large-scale events corresponding to $u_L/u_* = 0$ while a negative change as a percentage attenuation of small-scale intensities compared to a $u_L/u_* = 0$ event. High-momentum large-scale events intensify the small-scale high-velocity events in the surface

layer. The higher the momentum-excess in large scales, the higher the strengthening effect on small-scale fluctuations, as is evident from the modulating influence for $u_L/u_* = 0.7$ and $u_L/u_* = 0.3$ (Fig. 3.2). Low-momentum large-scale events have the opposite effect on the variance of small-scale fluctuations. Low-velocity large-scale regions weaken small-scale fluctuation intensities. A low-velocity event of $u_L/u_* = -0.7$ shows more weakening of the small-scale variance than does a $u_L/u_* = -0.3$ event. The effect of high-velocity and low-velocity large-scale events reverses at a height where the surface layer nominally ends. After the crossover point, low-momentum large-scale events intensify the turbulent fluctuations, whereas a high-momentum event at these heights correlates to a turbulence deficit of small scales. The magnitude of modulation by large scales also increases with height beyond the crossover point. The crossover point has been reported to be located at $z^+ = 3.9\sqrt{Re_\tau}$ in GH12, where, z^+ is the wall normal height measured in terms of viscous units and Re_τ is the Reynolds number defined in terms of friction velocity and boundary layer depth δ . In the present study where Re is infinite under the limiting case of inviscid flow the crossover point is observed to be located at 0.18δ . The trends of modulation of the small-scale variance by the large-scale fluctuations are similar across the three different flows analyzed. Qualitatively, the results are very similar to those reported in GH12.

The characteristic wavenumber of small-scale motions that are conditioned by the excursions of large scales from the mean flow showed very similar behavior for the three cases (Fig. 3.3). It is evident from Fig. 3.3 that the amplitude of the large-scale motions does not influence the characteristic wavenumber of small scales for a particular case. The general trend of the characteristic wavenumber decreasing in the wall-normal direction indicates that the spatial extent of modulated small scales that are under the influence of large scales increases with height. However, this trend is not monotonous. The modulated small scales grow in spatial extent till nearly 20% of the boundary layer height and then reach a plateau, finally shifting towards smaller spatial extent again. In general, this agrees with GH12 who observed that the characteristic frequency of small scales decreased with increasing distance from the surface in the region from $y/\delta = 0.01 - 0.6$, after which it plateaued and then increased as the height reached the boundary layer top. In general, a functional independence of the characteristic frequency/wavenumber of small-scale turbulent motions on large-scale fluctuations is manifested in the collapse of lines corresponding to different

u_L values.

A statistical analysis of wall-normal shear stress is also presented in this study to understand the influence of large-scale velocity fluctuations to the turbulent shear stress variations. Figure 3.4 shows how excursions of velocity from the mean value in the large scales impact the deviation of turbulent shear stress from the mean along with the range of deviation measured in terms of standard deviations. It is evident that at any wall normal location, the weakest of the large-scale events corresponding to $u_L = 0$ causes the highest magnitude of the shear stress. This emphasizes that the mean flow is responsible for majority of the shear stress. The level of fluctuation in the large scales also directly correlates to the magnitude of the shear stress. The higher the magnitude of fluctuation in the large scale, the lower is the contribution to the turbulent shear stress. Also, it is apparent that low-momentum large scale structures tend to contribute more to shear stress than high-momentum structures. The characteristic influence of large-scale structures on shear stress are similar across flow fields analyzed. The effect of modulation of VLSMs on small-scale motions was also studied with a different threshold that separated VLSMs and small-scale motions. The large-scale component of the fluctuating velocity field ($u_L(z)$) was also obtained by filtering $u'(z)$ with a spectral cut-off filter where the cut-off wavelength was 5δ . This different threshold value did not impact the observations qualitatively. However, here only results for 2δ cut-off scale are shown.

3.4 Analysis of Interscale Energy Transfer in the Wavelet Domain

Before analyzing the energy exchange between individual scales in the wavelet domain, we take a look at the comparison of spectra to discern the turbulent kinetic energy distribution over length scales in different cases. Premultiplied spectra of the streamwise velocity component averaged over the spanwise direction for all three cases are shown in Fig. 3.5. The spectra are normalized with u_* and multiplied by wavenumber k_x . In the figure, the solid lines represent Fourier spectra, and the circles represent wavelet spectra. In the inertial subrange of turbulence, theory predicts and experimental evidence supports that the velocity spectra will follow a power law resulting in the well-known $-5/3$ spectral scaling (or $-2/3$ for premultiplied spectra) [63]. The premultiplied spectra for all cases

exhibits inertial range scaling with an expected slope of $-2/3$ for normalized wavenumbers $k_x z > 1$. *CHNL* has a clear range of scales that fall into zero slope region, while *EK10* and *EK02* do not exhibit a range of scale with a matching zero slope. It is apparent in *EK10* and *EK02* that normalized wavenumbers of the order of $k_x z = 1$ display to have the maximum energy available ,which means that at any height z , an eddy of the order of length scale z can be expected to have the maximum energy available. It is also apparent from the figure that at higher heights, the characteristic eddies tend to be shorter than z , and at lower heights characteristic eddies tend to be larger than z . This indicates the availability of large-scale motions at lower boundary layer. Also a widening of the band of energetic scales with decreasing the wall normal distance is observed. This is consistent with the attached hairpin eddy model of structural organization of a turbulent flow as proposed by Perry et al. [63], Nickels and Marusic [64] which projects that near the wall more eddies are available to contribute to the energy. The spectra also help to identify dynamically different discrete wavelet scales. For example, it is apparent from Fig. 3.5(a) and Table 3.2 that discrete wavelet scales corresponding to decomposition level 2, 3, 4, 5, and 6 fall into energy containing scales regime and scales corresponding to level 7, 8, and 9 fall into the inertial subrange regime for the *CHNL* case. Similarly, all discrete wavelet scales corresponding to different turbulent dynamical regimes can be identified for *EK10* and *EK02*. Although the spectra reveal the range of important scales in the flow, the dynamics between individual scales cannot be understood. In the following after a brief presentation of the wavelet framework, interscale energy exchange is examined to assess the importance of scale-scale interaction related to VLSMs in the ABL.

A function in $L^2(\mathbb{R}^N)$ can be expanded as a series of orthonormal basis functions and when these orthonormal basis functions consist of scaled and translated versions of a single mother-wavelet function, and a scaling function, the expansion becomes a discrete wavelet expansion. A class of functions that conform to the admissibility condition, are orthogonal to their integer translates, and orthogonal to their own dilations [65, 66] are classified as orthogonal wavelets. The discrete scaling ($w_\phi(j_o, m, n)$) and wavelet coefficients ($w_\psi(j, m, n)$) of a function $\beta(x, y)$ can be obtained from the inner product of the separable basis functions $\phi_{j_o, m, n}$, $\psi_{j, m, n}^i$ with the function $\beta(x, y)$ as [66, 67, 68]:

$$\begin{aligned} w_\phi(j_o, m, n) &= \frac{1}{\sqrt{MN}} \sum_{\zeta=0}^{M-1} \sum_{\eta=0}^{N-1} \beta(\zeta \Delta_x, \eta \Delta_y) \phi_{j_o, m, n}(\zeta, \eta) \\ w_\psi^q(j, m, n) &= \frac{1}{\sqrt{MN}} \sum_{\zeta=0}^{M-1} \sum_{\eta=0}^{N-1} \beta(\zeta \Delta_x, \eta \Delta_y) \psi_{j, m, n}^i(\zeta, \eta), \quad q = \{H, V, D\}, \end{aligned} \quad (3.9)$$

where $N = M = 2^J$ are the number of grid points in y and x directions, ζ and η are the grid indices, Δ_x and Δ_y are the grid resolutions, respectively in x, y directions and j_o denotes an arbitrary starting scale for the wavelet decomposition, which is unity in this case. The 2D array of scaling coefficients $W_\phi(j_o, m, n)$ gives an approximation at scale j_o , i.e., low pass filtered version of the analysed function $\beta(x, y)$, while three other 2D zarrays $W_\psi^{(H, V, D)}(j, m, n)$ give complementary details to the approximation in horizontal, vertical, and diagonal directions respectively at scales $j \geq j_o$, such that the function $\beta(x, y)$ can be perfectly reconstructed from all the coefficients, where, $j = j_o, j_o + 1, j_o + 2, \dots, J - 1$; m, n are the number of non-zero filter coefficients of 1D filters that constitute 2D separable wavelet functions. The 2D scaling and wavelet functions are derived from products of 1D functions as follows:

$$\phi(x, y) = \phi(x)\phi(y), \quad (3.10)$$

$$\psi^H(x, y) = \phi(x)\psi(y), \quad (3.11)$$

$$\psi^V(x, y) = \psi(x)\phi(y), \quad (3.12)$$

$$\psi^D(x, y) = \psi(x)\psi(y), \quad (3.13)$$

where $\phi(x)$, $\phi(y)$ are one-dimensional scaling, and $\psi(x)$ and $\psi(y)$ are the wavelet functions. The scaled and translated scaling and wavelet functions at different decomposition levels (j) that form the basis of the fast wavelet transform are:

$$\phi_{j, m, n}(x, y) = 2^{j/2}\phi(2^j x - m, 2^j y - n) \text{ and} \quad (3.14)$$

$$\psi_{j, m, n}^i(x, y) = 2^{j/2}\psi(2^j x - m, 2^j y - n), \quad i = \{H, V, D\}. \quad (3.15)$$

The details of implementation of the fast wavelet transform from these functions can be found in [66, 67].

Following Meneveau [69], any generic dependent variable (β) obtained from LES can be decomposed into large- and small-scale fluctuations using wavelet filtering,

$$\beta(x, y) = \bar{\beta}(x, y) + \beta(x, y)^{<n} + \beta(x, y)^{>n} \quad (3.16)$$

where

$$\bar{\beta}(x, y) = \frac{1}{\sqrt{MN}} \sum_m \sum_n w_\phi(j_o, m, n) \phi_{j_o, m, n}(x, y), \quad (3.17)$$

is the mean horizontal value of β . $\beta^{<n}$ denotes large-scale fluctuations, which is equivalent to the low-pass filtered portion of β where cut-off wavelength is r_n , and $\beta^{>n}$ denotes the small-scale counterpart. $\beta^{<n}$ can be obtained from a summation of all wavelet scales larger than the scale represented by r_n :

$$\beta^{<n}(x, y) = \sum_{q=H,V,D} \sum_{j=1}^n \sum_m \sum_n w_\psi^q(j, m, n) \psi_{j, m, n}(x, y). \quad (3.18)$$

Similarly, the small-scale fluctuating component can be obtained as,

$$\beta^{>n}(x, y) = \sum_{q=H,V,D} \sum_{j=n+1}^J \sum_m \sum_n w_\psi^q(j, m, n) \psi_{j, m, n}(x, y). \quad (3.19)$$

In practice, $\beta^{<n}$ is obtained by setting all wavelet coefficients above level n and scaling coefficients to zero and then carrying out the inverse wavelet transform to reconstruct the field from the remaining non-zero coefficients. $\beta^{>n}$ is obtained in a similar fashion by setting all wavelet and scaling coefficients below level n to zero and the inverse wavelet transform from only the scaling coefficients, setting all wavelet coefficients to zero, recovers the mean field ($\bar{\beta}$). $\beta^{>n}$ and $\beta^{<n}$ can be compared to the filtered β fields obtained through the application of high-pass and low-pass, spectral-cutoff filters with the cutoff wavenumber k_n corresponding to $2\pi/r_n$, respectively.

Expressing velocity and pressure fields as wavelet series, the nonlinear term in the conservation of momentum equation can be decomposed in a manner similar to Leonard's decomposition [70] with

$$u_i u_j = (\bar{u}_i + u_i^{<n} + u_i^{>n})(\bar{u}_j + u_j^{<n} + u_j^{>n}), \quad (3.20)$$

which can be rearranged to define a term T_{ij} that represents the summation of the pseudo cross-stress tensor that accounts for interactions among large- and small-scale turbulent motions and the Reynold's stress tensor as:

$$u_i u_j - \Gamma - u_i^{<n} u_j^{<n} = u_i^{>n} u_j^{<n} + u_i^{<n} u_j^{>n} + u_i^{>n} u_j^{>n} = \theta_{ij}, \quad (3.21)$$

where, $\Gamma = \bar{u}_i \bar{u}_j + u_i^{<n} \bar{u}_j + u_i^{>n} \bar{u}_j + \bar{u}_i u_j^{<n} + \bar{u}_i u_j^{>n}$ and $u_i^{<n} u_j^{<n}$ is the Reynold's stress for fluctuations below decomposition level n .

For convenience, we have adopted the Meneveau's notation and will denote wavelet coefficient of the velocity fields at scale m as $w_\psi^{m,q}[\mathbf{i}]$ and that of all other variables as $[]_\psi^{(m,q)}[\mathbf{i}]$. The transport equation of *tke* for the scale r_m can be written as:

$$\begin{aligned} \frac{\partial}{\partial t} (w_\psi^{(m,q)})^2 [\mathbf{i}] + w_\psi^{(m,q)} [\mathbf{i}] \left[\frac{\partial}{\partial x_j} (u_i^{<n} u_j^{<n} + \Gamma) \right]_\psi^{(m,q)} [\mathbf{i}] = \\ - w_\psi^{(m,q)} [\mathbf{i}] \left[\frac{\partial}{\partial x_i} (p^{<n}) \right]_\psi^{(m,q)} [\mathbf{i}] - w_\psi^{(m,q)} [\mathbf{i}] \left[\frac{\partial p^{>n}}{\partial x_i} + \frac{\partial}{\partial x_j} (\theta_{ij} + \tau_{ij}) \right]_\psi^{(m,q)} [\mathbf{i}], \end{aligned} \quad (3.22)$$

where the last term in Eqn. 3.22 encompasses the nonlinear interactions across scales and here is used to define

$$t^{(m,n)} = \sum_{i=1}^2 \sum_{q=1}^3 w_\psi^{(m,q)} [\mathbf{i}] \left[\frac{\partial p^{>n}}{\partial x_i} + \frac{\partial}{\partial x_j} (\theta_{ij} + \tau_{ij}) \right]_\psi^{(m,q)} [\mathbf{i}]. \quad (3.23)$$

The term $t^{(m,n)}$ that accounts for the transfer of energy between scales r_m and all scales smaller than r_n ($r_m \geq r_n$) can be recovered from the decomposition in 3.21. Meneveau [69] explained the term $t^{(m,n)}$ as an alternative to the scale-scale transfer term $G(k|k_n)$ representing the nonlinear interactions among turbulent scales in the Fourier domain such that $G(k|k_n)$ demotes the aggregate effect of nonlinear interactions to wavenumber k due to interactions among triads of scales $(k, p, k-p)$ where, " $k < k_n$ and at least one of the other two legs is larger than k_n ". A similitude of $t^{(m,n)}$ can be drawn with the detailed triadic interactions as formulated in the spectral space by Domaradzki et al. [71]:

$$t^{(m,n)} \approx \sum_{p=1}^{k_{max}} \sum_{q>k_n}^{k_{max}} G^{pqn}. \quad (3.24)$$

A negative value of $t^{(m,n)}$ represents energy loss from the scale r_m and a positive value indicates energy transfer to scale r_m from scales smaller than r_n , i.e., backscatter. The same filter scale (r_m/r_n) must be used in both horizontal directions and thus, a single (m/n) integer is used to represent the filter scale. This is in contrast to spectral space where a wide array of wave vectors that obey the triangle relation $\bar{\mathbf{p}} + \bar{\mathbf{q}} = \bar{\mathbf{m}}$ can interact nonlinearly. The disadvantage is that while spectral space allows one to probe into the detailed triadic scale interactions, a local-spatial distribution of energy cannot be obtained. Wavelet space in spite of limitations of entangling spatial transport with scale-scale interaction provides an opportunity to explore spatial distribution of scale-scale interactions that can be used to

develop an understanding of the sparsity of turbulent energy and quantify its intermittency [69, 72, 73].

A dual bi-spectrum of subgrid energy exchange can be defined from $t^{(m,n)}$ following Meneveau [69] as,

$$T(z, k_m | k_n) = \frac{2^{-(J-n)} (\Delta x \Delta y)^{1/2} t^{(m,n)}}{2\pi \ln(2)}. \quad (3.25)$$

Figures 3.6, 3.7, 3.8 and 3.9, 3.10, 3.11 show the dual bi-spectrum of subgrid scale energy spectra, i.e., the rate of energy transfer per unit area per unit length of scale, $T(z, k_m | k_n)$, at different horizontal planes above the ground. The results shown in Fig. 3.6, 3.7, 3.8 and 3.9, 3.10, 3.11 differ in their definition of $T(z, k_m | k_n)$. Fig. 3.6, 3.7, 3.8 use a definition of $T(z, k_m | k_n)$ where the filter scale r_n is always smaller than r_m and interaction among triads of scales are considered where at least one of the scale is $\leq \frac{1}{2}r_m$. In Fig. 3.9, 3.10, 3.11, $T(z, k_m | k_n)$ is due to interactions of scales r_m with scale r_m and scales smaller than r_m . In Fig. 3.6, 3.7, 3.8 backscattering events far outnumber forward energy cascade events. However, a comparison between Fig. 3.6, 3.7, 3.8 and 3.9, 3.10, 3.11 shows that for any particular scale, energy exchange due to interactions between neighbouring scales dwarfs interactions between distant scales. In Fig. 3.9, 3.10, 3.11 forward cascade of energy is dominant over backscattering. In most of the cases, it is the neighbouring scale in terms of dyadic wavelet scales where most of the energy exchange for any fixed r_n occurs irrespective of the direction of energy transfer.

Although the discrete wavelet transform is limited only to dyadic scales, local and nonlocal energy transfer can be identified in the limiting cases. Studies that looked into turbulent energy exchange between scales in the Fourier space defined local versus non-local energy transfers in relation to the smallest and the largest scale in the triad. If k, p , and q are the three wavemodes of the nonlinear term obeying the condition $k + p + q = 0$, the ratio between the maximum and the minimum length scales can be defined as $s = \max(k, p, q)/\min(k, p, q)$. Domaradzki et al. [71] and Bourouiba et al. [74] categorized interaction between scales as a local if $s \leq 2$ and nonlocal if $s \geq 2$. Under this definition of locality of scales, it can be concluded that energy transfer is predominantly local for all scales larger or of the order of LSMs in all cases. This trend is observed throughout the boundary layer. Two instances of nonlocal energy transfer are observed in *CHNL* (Fig.

3.6). All scales smaller than 0.08δ are observed to be receiving a relatively higher amount of energy from distant scales 0.33δ and 0.67δ . A similar nonlinear interaction is observed when scales smaller than 0.17δ interact with scale 0.67δ . Also, energy contribution to scales smaller than 0.17δ from 0.33δ and 0.67δ are comparable. In *Ek10*, one instance of nonlocal interaction is observed within the analyzed range of scales. Scale 0.35δ tend to contribute more subgrid energy to scales smaller than 0.09δ as compared to scale 0.17δ (Fig. 3.7). *EK02* shows mostly local interaction among scales within the analyzed range (Fig. 3.8). All the observed nonlocal interactions are attributed to scales smaller than or at the lower end of the presumed definition of LSMs. It can for this reason be concluded that VLSMs do not influence the dynamics of smaller scale motions through nonlocal interactions while LSMs have the potential to have nonlocal impact for some range of scales. It must be emphasized that the relative contribution of nonlocal transfers in backscattering is very small compared to local transfer (Fig. 3.9, 3.10, 3.11). In Fig. 3.9, 3.10, 3.11, backscattering is observed only above the log region in all three cases. Scale-scale interaction show differences in *EK02* compared to *EK10* and *CHNL* including markedly less of a tendency of backscattering.

From the definition of $t^{(m,n)}$ a local subgrid-scale flux of energy can be calculated by summing $t^{(m,n)}$ over m ,

$$\Pi_{sg}^n(z)[\mathbf{i}] = - \sum_{m=1}^n 2^{2n} t^{(m,n)}[2^{(m-n)}\mathbf{i}], \quad (3.26)$$

where Π_{sg}^n quantifies the summation of energy transfer from all scales larger or equal to r_m to scales smaller than r_n . According to the current definition, a positive value of Π_{sg}^n would refer to energy transfer from large to small scales and a negative value would indicate energy transfer from small to large scales, i.e., backscatter. From Π_{sg}^n , a subgrid energy flux spectra is defined as: $\pi_{sg}^n = 2^{-2(M-n)} \langle \Pi_{sg}^n \rangle$, which quantifies rate of local energy dissipation per unit area from scales larger than r_n . Meneveau [69] explained this term as a surrogate of the LES term that quantifies energy transfer between resolved and subgrid scale motions, i.e., $(\tilde{u}_i \frac{\partial}{\partial x_j} (\widetilde{u_i u_j} - \widetilde{\tilde{u}_i \tilde{u}_j}))$. In case of a homogeneous flow, this analogy is straightforward; however, for any wall bounded flow where heterogeneity is strong at least in one direction, this should be understood with caution and for variables filtered appropriately in the homogeneous directions only. In this study, where homogeneity can only be assumed in horizontal directions π_{sg}^n calculated in a wavelet filtering framework is

analogous to $(\tilde{u}_i \frac{\partial}{\partial x_j} (\widetilde{u_i u_j} - \widetilde{\tilde{u}_i \tilde{u}_j}))$, where variables are filtered with a 2D filter on surface-parallel planes. The turbulent flow field at any wall-normal location (z) was obtained by subtracting convection velocity $\langle u \rangle(z)$, where $\langle u \rangle(z)$ was the mean horizontal velocity assumed steady after the simulation had reached a quasi-steady condition. In practice, these assumptions allowed us to treat the velocity field represented by wavelet scaling coefficients as one for which inverse wavelet transform would yield the average velocity field with a convection velocity of $\langle u \rangle(z)$. π_{sg}^n can also be understood as a scale-dependent version of the combined terms $(-\frac{\partial}{\partial x_i} \langle p' u' \rangle - u'_j \frac{\partial \langle q \rangle}{\partial x_j} - \frac{\partial}{\partial x_j} \langle u'_i \tau'_{ij} \rangle + \langle \tau'_{ij} s'_{ij} \rangle)$ in Eqn. A.5. In Fig. 3.12, horizontally averaged scale-dependent subgrid-scale energy transfer $\langle \pi_{sg}^n \rangle$ is shown. Panels a' , b' , and c' on the right-hand side of Fig. 3.12 show the results corresponding to Eqn. 3.26. Panels a , b , and c on the left shows $\langle \pi'_{sg}^n \rangle$. Subgrid energy flux spectra $\langle \pi'_{sg}^n \rangle$ differs from $\langle \pi_{sg}^n \rangle$ as defined in Eqn. 3.26. $\langle \pi'_{sg}^n \rangle$ is derived from a slightly different definition of Π_{sg}^n than Eq. 3.26 as follows:

$$\Pi'_{sg}^n(z)[\mathbf{i}] = - \sum_{m=1}^{n-1} 2^{2n} t^{(m,n)}[2^{(m-n)}\mathbf{i}]. \quad (3.27)$$

The difference between π_{sg}^n and π'_{sg}^n is that the former term accounts for the energy transfer occurring between scales of spatial extent of r_n , and all scales equal to r_n or smaller, while the later only includes aggregate results of interaction between all scales larger than r_m and smaller than r_n . Substantial difference between π_{sg}^n and π'_{sg}^n suggests that within the interrogated wavelet scale regime where integer length scales are distributed over $\log(2)$ scale, interactions among the similar spatial scales dominate the subgrid-scale energy transfer. In Fig. 3.12, π_{sg}^n and π'_{sg}^n are normalized by estimated dissipation in the log layer. Using the relevant velocity scale (u_*) in the internal ABL and an estimated velocity gradient in the log layer derived from similarity theory, an energy scale relevant in the log layer can be formed as $u_*^3/(\Delta z \kappa)$, where Δz is the resolution of the simulation in the wall normal direction, i.e., distance of the first u-node in wall normal direction [75]. This energy estimate is the expected order of energy to exist in the surface layer. Panels a , b , and c in Fig. 3.12 indicate that local subgrid-scale energy transfer due to interactions of distant scales on an average is negative, i.e., backscatter. This trend is consistent across all three cases and throughout the boundary layer. Smaller scales are observed to transfer higher amounts of energy to larger scales. For example, in Fig. 3.12(a), all scales smaller than

$r_n = 0.08\delta$ are observed to transfer more energy to scales larger than 0.17δ compared to the total energy transfer from scales smaller than 0.17δ to scales larger than 0.33δ . Panels a' , b' , and c' show plane average π'_{sg}^n and show a very different distribution compared to plane average π_{sg}^n . The quantity π'_{sg}^n accounts for the interaction of similar length scales. However, the spatial transport $\left\{ \frac{\partial}{\partial x_j} (u_i \tau_{ij}) \right\}$ due to interaction of large scales with a band of small scales cannot be separated in this formulation while analysing the energy transfer ($\tau_{ij} S_{ij}$) due to lack of a simple relation between wavelets and its derivatives as was pointed out by Meneveau [69].

3.5 Summary and Conclusions

The existence of VLSMs as slender and elongated low- or high-momentum regions clearly marked with borders has been confirmed from visual inspection of the flow fields in the atmospheric boundary layer [76]. The importance of these structures is of interest because of the fact that any turbulent flow exhibits a hierarchy of motions of different scales. The role of VLSMs in this hierarchy is not completely defined. One important aspect of VLSMs is that they influence or modulate small-scale motions and the characterization of this modulation was explored in Sec. 3.3. For this analysis on modulation effect, the large scale has been defined as any motion with a scale larger than 2δ . The same analysis was carried out with a cut-off scale of 5δ to separate large and small scales. Irrespective of the definition of large scales, qualitatively, results did not change. It was observed that large-scale fluctuations correlate with small-scale fluctuations in agreement with previous work [62] and that the degree of fluctuation in large scales dictates the degree of fluctuation in small scales with large fluctuations in large scales corresponding to large fluctuations in small scales. The frequency of fluctuations of small scales, however, is not strongly correlated to the strength of fluctuations of large scale in the log and outer region and appears to be a function of height. The magnitude of Reynold's stress is inversely correlated to the intensity of large-scale fluctuations. This observation bears importance in automated detection algorithms of VLSMs in any flow field and suggests that VLSMs are most likely to be found as areas characterized by lower Reynold's stresses.

The mechanism of exerting influence on small-scale dynamics by large scales is explored through interscale energy exchange in the wavelet domain. The main question was whether

nonlocal energy transfer would be responsible for the influence of VLSMs on small-scale motions. It was observed that the magnitude of nonlocal energy transfer in the three examined cases was insignificant compared to the local energy transfer. There was no evidence found that VLSM or LSM could significantly impact small-scale turbulent motions through nonlocal energy transfer. Another question was whether weak rotation would impact energy transfer between scales and ultimately impact the organization of VLSMs and LSMS. This was particularly important due to the fact that in the environment at large scales, Coriolis force cannot be ignored. Prior work has shown that for very low Rossby number including the limiting case of solid body rotation (zero Ro number), the energy transfer characteristics change even though the Coriolis force is absent from the tke transport equation [77, 78]. Weak rotation as has been interrogated in this study also shows its impact on the energy distribution over length scales. This is evident from the one-dimensional spectra of the streamwise velocity (Fig. 3.5). Unlike pressure-driven channel flow, a very narrow band of scales contain most of the tke when there is a Coriolis force. This could indicate the inhibition of the development of VLSMs or shortening of the length scale of VLSMs. However, significant changes in the local, nonlocal energy transfer characteristics were not observed, an indication that the fundamental turbulent dynamics were not altered although the ratio of the largest to smallest energy containing length scales did change when Coriolis force was introduced.

As the method responsible for the organisation of VLSMs, GH12 associated the well-known paradigm of the train of hairpin vortices where counter rotating vortices align themselves along the streamwise direction spaced by the inclined, induced long regions of low- and high-speed fluids. From kinematic consideration, this scenario stands out as a possible organization of the constituent coherent structures that shape VLSMs. By coherent structures, we refer to a conglomeration of phase-correlated vortices following the definition adopted by Hussain [79] and prefer to maintain a clear distinction between coherent structures and VLSMs, which are often mixed up and used interchangeably in the literature. This distinction is important to maintain to understand the physical energy cascade process. Although scale-scale interaction or the turbulent energy content over scales is analysed in spectral space or wavelet space, the physical mechanism of transfer is most often explained by vorticity dynamics. There is an apparent disconnect between energy

density over assumed wavelike motions, which do not really exist in a turbulent flow field, and the physical mechanism of vortex stretching or merging through which energy transfers to smaller scales or travels towards larger scales, respectively.

The physical mechanism of energy transfer from large to smaller scales corresponds to breaking up of large energy containing coherent motions [80, chap. 5]. Irrespective of the background mechanism responsible for the formation of LSMs and VLMSs, the interscale energy transfer characteristics as explored here indicate that it is possible for smaller scale motions to merge together to form large-scale motions. This prediction can be attributed to the observed transfer of energy from small to large scales. However, a hierarchy of this merging process is also observed. In general, smaller scale motions combine to form a larger scale motions and those larger scale motions would combine to form even larger scale motions. However, the reverse cascading of energy does not break the observance of Richardson's prescribed forward energy cascading. The energy transfer from large to small scales always dwarfs the energy transfer from small to large scales. The observed energy exchange process and spectra here lend support toward the hypothesis that LSMs concatenate to form VLSMs as suggested by Baltzer et al. [41], Balakumar and Adrian [42], Kim and Adrian [50].

3.6 References

- [39] J. P. Monty, J. A. Stewart, R. C. Williams, and M. S. Chong. Large-scale features in turbulent pipe and channel flows. *Journal of Fluid Mechanics*, 589, 2007.
- [40] M Guala, S. E. Hommema, and R. J. Adrian. Large-scale and very-large-sacle motions in turbulent pipe flow. *Journal of Fluid Mechanics*, 554:521–542, 2006.
- [41] J. R. Baltzer, R. J. Adrian, and Xiaohua Wu. Structural organization of large and very large scales in turbulent pipe flow simulation. *Journal of Fluid Mechanics*, 720, 2013.
- [42] B. J. Balakumar and R. J. Adrian. Large and very-large-sacle motions in channel and boundary-layer flows. *Philosophical Transactions of the Royal Society A*, 365:665–681, 2007.
- [43] Jin Lee, Jae Hwa Lee, Jung-II Choi, and Hyung Jin Sung. Spatial organization of large- and very-large-scale motions in a turbulent channel flow. *Journal of Fluid Mechanics*, 749:818–840, 2014.
- [44] N. Hutchins and Ivan Marusic. Evidence of very long meandering features in the logarithmic region of turbulent boundary layers. *Journal of Fluid Mechanics*, 579: 1–28, 2007.

- [45] Jiannong Fang and Fernando Porté-Agel. Large-eddy simulation of very large-scale motions in the neutrally stratified atmospheric boundary layer. *Boundary-Layer Meteorology*, 155:397–416, 2015.
- [46] Jae Hwa Lee and Hyung Jin Sung. Very-large-sacle motions in a turbulent boundary layer. *Journal of Fluid Mechanics*, 673:80–120, 2011.
- [47] David J. C. Dennis and Timothy B. Nickels. Experimental measurement of large-scale three-dimensional structures in a turbulent boundary layer. part 2. long structures. *Journal of Fluid Mechanics*, 673, 2011.
- [48] D Chung and B. J. McKeon. Large-eddy simulation of large-scale structures in long channel flow. *Journal of Fluid Mechanics*, 661, 2010.
- [49] F. Kerhervé, S. Roux, and R. Mathis. Combining time-resolved multi-point and spatially-resolved measurements for the recovering of very-large-scale motions in high reynolds number turbulent boundary layer. *Experimental Thermal and Fluid Science*, 82:102–115, 2017.
- [50] K. C. Kim and R. J. Adrian. Very large-scale motion in the outer layer. *Physics of Fluids*, 11:417–422, 1999. doi: 10.1063/1.869889.
- [51] Reginald J. Hill. Exact second-order structure-function relationships. *Journal of Fluid Mechanics*, 468:317–326, 2002.
- [52] N. Marati, C. M. Casciola, and R. Piva. Energy cascade and spatial fluxes in wall turbulence. *Journal of Fluid Mechanics*, 521:191–215, 2004.
- [53] M. T. Landahl and E. Mollo-Christensen. *Turbulence and random processes in fluid mechanics*. Cambridge University Press, 2nd edition, 1992.
- [54] Rob Stoll and Fernando Porté-Agel. Dynamic subgrid-scale models for momentum and scalar fluxes in large-eddy ssmulation of neutrally startified atmospheric boundary layers over heterogeneous terrain. *Water Resources Research*, 42(1), 2006.
- [55] Rob Stoll and Fernando Porté-Agel. Surface heterogeneity effects on regional-scale fluxes in stable boundary layers: surface temperature transitions. *Journal of the Atmospheric Sciences*, 66(2):412–431, 2009. doi: 10.1175/2008JAS2668.1.
- [56] Brian N. Bailey and Rob Stoll. Turbulence in sparse, organized vegetative canopies: a large-eddy simulation study. *Boundary-Layer Meteorology*, 147(3):369–400, 2013. doi: 10.1007/s10546-012-9796-4.
- [57] Nathan E. Miller and Rob Stoll. Surface heterogeneity effects on regional-scale fluxes in the stable boundary layer: aerodynamic roughness length transitions. *Boundary-Layer Meteorology*, 149(2):277–301, 2013. doi: 10.1007/s10546-013-9839-5.
- [58] Brian N. Bailey, Rob Stoll, Eric R. Pardyjak, and Walter F. Mahaffee. Effect of vegetative canopy architecture on vertical transport of massless particles. *Atmospheric Environment*, 95:480 – 489, 2014. doi: <https://doi.org/10.1016/j.atmosenv.2014.06.058>.
- [59] Brian N. Bailey and R. Stoll. The creation and evolution of coherent structures in plant canopy flows and their role inturbulent transport. *Journal of Fluid Mechanics*, 789:425–460, 2016. doi: 10.1017/jfm.2015.749.

- [60] Romain Mathis, Nicholas Hutchins, and Ivan Marusic. Large-scale amplitude modulation of the small-scale structures in turbulent boundary layers. *Journal of Fluid Mechanics*, 628:311–337, 2009. doi: 10.1017/S0022112009006946.
- [61] Matteo Bernardini and Sergio Pirozzoli. Inner/outer layer interactions in turbulent boundary layers: A refined measure for the large-scale amplitude modulation mechanism. *Physics of Fluids*, 23(6):061701, 2011. doi: 10.1063/1.3589345. URL <http://dx.doi.org/10.1063/1.3589345>.
- [62] B. Ganapathisubramani, N. Hutchins, J. P. Monty, D. Chung, and I. Marusic. Amplitude and frequency modulation in wall turbulence. *Journal of Fluid Mechanics*, 712, 2012.
- [63] A. E. Perry, S. Henbest, and M. S. Chong. A theoretical and experimental study of wall turbulence. *Journal of Fluid Mechanics*, 165:163–199, 1986.
- [64] T. B. Nickels and Ivan Marusic. On the different contributions of coherent structures to the spectra of a turbulent round jet and a turbulent boundary layer. *Journal of Fluid Mechanics*, 448:367–385, 2001.
- [65] Ingrid Daubechies. Orthonormal bases of compactly supported wavelets. *Communications on Pure and Applied Mathematics*, 71(7), 1988.
- [66] C. Sidney Burrus, Ramesh A. Gopinath, and Haitao Guo. *Introduction to Wavelets and Wavelet Transformations A Primer*. Prentice-Hall Inc., 1st edition, 1998.
- [67] Rafael C. Gonzalez and Richard E. Woods. *Digital Image Processing*. Prentice-Hall Inc., 3rd edition, 2008.
- [68] Richard Baraniuk, Hyeokho Choi, Ramesh Neelamani, Vinay Ribeiro, Justin Romberg, Haitao Guo, Felix Fernandes, Brent Hendricks, Ramesh Gopinath, Markus Lang, Jan Erik Odegard, Dong Wei, and Josh Jackson. *The Rice Wavelet Toolbox*, 2014. URL <http://github.com/ricedsp/rwt>.
- [69] Charles Meneveau. Analysis of turbulence in the orthonormal wavelet representation. *Journal of Fluid Mechanics*, 232:469–520, 1991.
- [70] A. Leonard. Energy cascade in large-eddy simulations of turbulent fluid flows. *Advances in Geophysics*, 18:237 – 248, 1975. ISSN 0065-2687. doi: [http://dx.doi.org/10.1016/S0065-2687\(08\)60464-1](http://dx.doi.org/10.1016/S0065-2687(08)60464-1). URL <http://www.sciencedirect.com/science/article/pii/S0065268708604641>. Turbulent Diffusion in Environmental Pollution.
- [71] J. Andrzej Domaradzki, Wei LiuCarlos Härtel, and Leonard Kleiser. Energy transfer in numerically simulated wall-bounded turbulent flows. *Physics of Fluids*, 6(4), 1994. doi: 10.1063/1.868272.
- [72] D. C. DUNN and J. F. MORRISON. Anisotropy and energy flux in wall turbulence. *Journal of Fluid Mechanics*, 491:353–378, 2003. doi: 10.1017/S0022112003005548.
- [73] David C. Dunn and Jonathan F. Morrison. Analysis of the energy budget in turbulent channel flow using orthogonal wavelets. *Computers & Fluids*, 34(2):199 – 224, 2005. ISSN 0045-7930. doi: <http://dx.doi.org/10.1016/j.compfluid.2004.04.003>. URL <http://www.sciencedirect.com/science/article/pii/S0045793004000787>.

- [74] L. Bourouiba, D. N. Straub, and M. L. Waite. Non-local energy transfers in rotating turbulence at intermediate Rossby number. *Journal of Fluid Mechanics*, 690:1–19, 2011.
- [75] J. R. Garrat. *The atmospheric boundary layer*. Cambridge University Press, 1992.
- [76] K. Träumner, Th. Damian, Ch. Stawiarski, and A. Wieser. Turbulent structures and coherence in the atmospheric surface layer. *Boundary-Layer Meteorology*, 154:1–25, 2015.
- [77] P. K. Yeung and Ye Zhou. Numerical study of rotating turbulence with external forcing. *Physics of Fluids*, 10(11), 1998.
- [78] Murshed Hossain. Reduction in the dimensionality of turbulence due to strong rotation. *Physics of Fluids*, 6(3), 1994.
- [79] A. K. M. F. Hussain. Coherent structures-reality and myth. *The Physics of Fluids*, 26, 1983.
- [80] P. A. Davidson. *Turbulence An Introduction for Scientists and Engineers*. Oxford University Press, 2004.

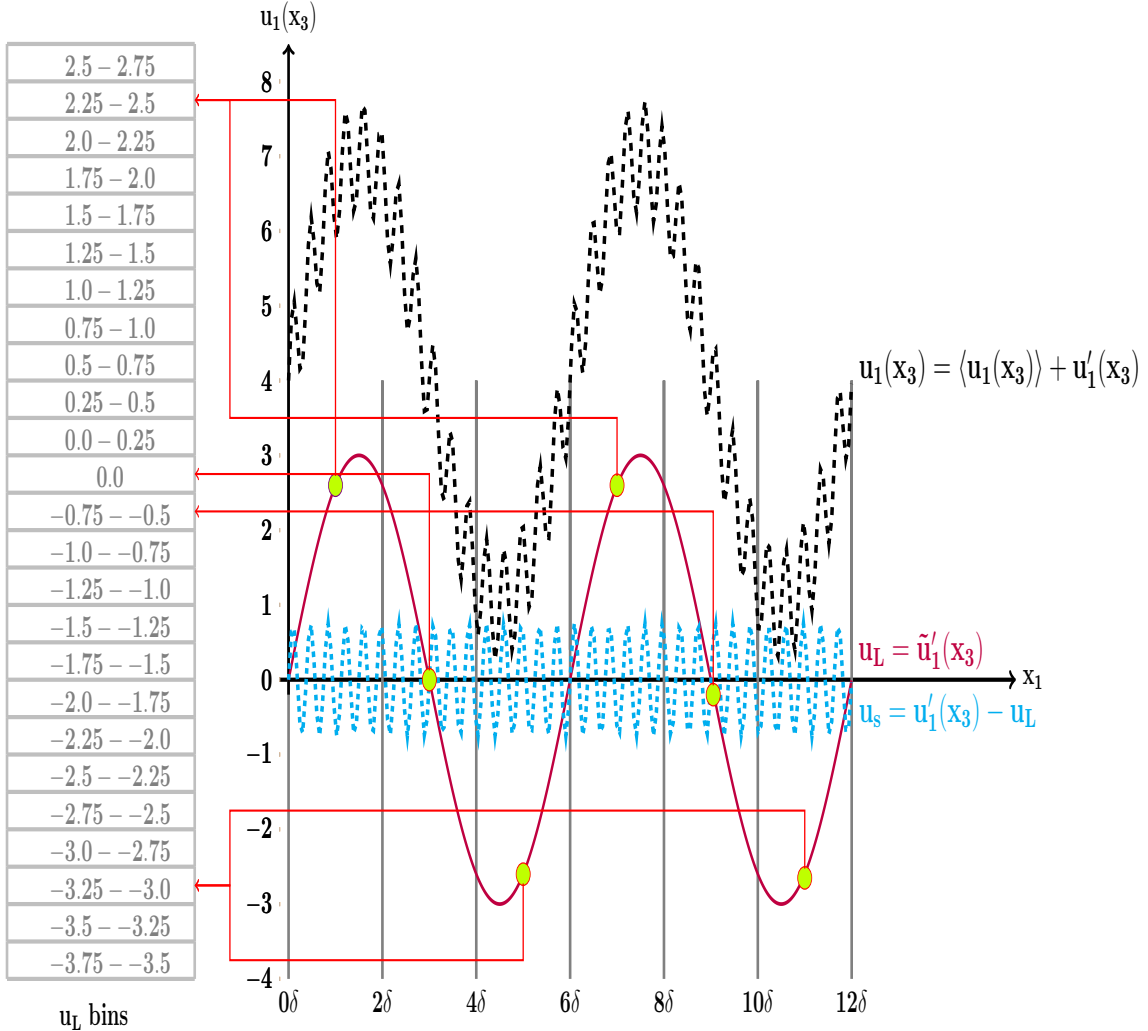


Figure 3.1. An illustration of the data extraction method used to investigate the modulation of the small-scale motions by large-scale motions is shown. The black dashed line in the figure represents a raw velocity signal ($u_1(x_3)$) extracted along a line in x_1 -direction from the simulated flow field. The filtered large-scale fluctuation (u_L) is represented by the red smooth line. The dotted blue line represents the data series of small-scale fluctuation (u_s). On the left, a hypothetical binning process for the u_L series is shown and the association of the representative u_L values to the correct bin is shown with arrows.

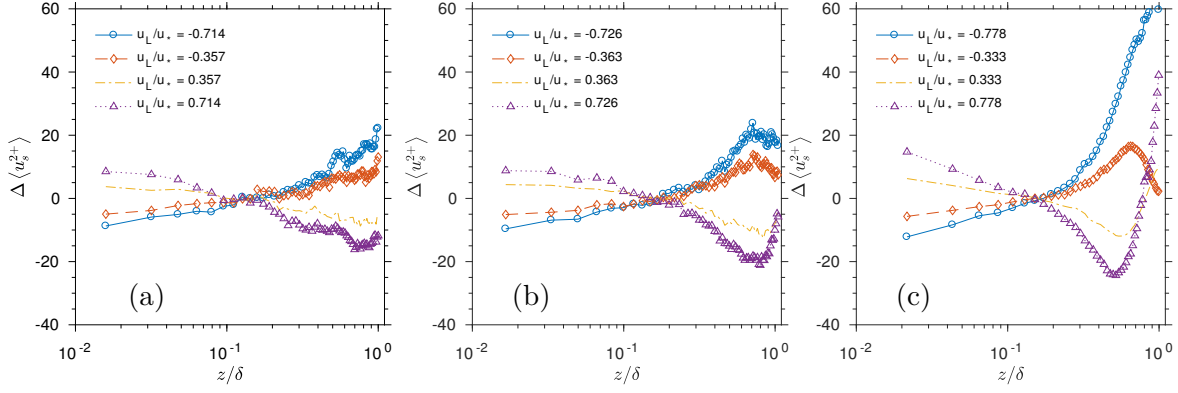


Figure 3.2. The relative strength of small-scale fluctuations conditioned on the strength of fluctuations of large scales as defined in Eq. 3.5 for the three different flow cases, (a) *CHNL*, (b) *EK10*, and (c) *EK02*.

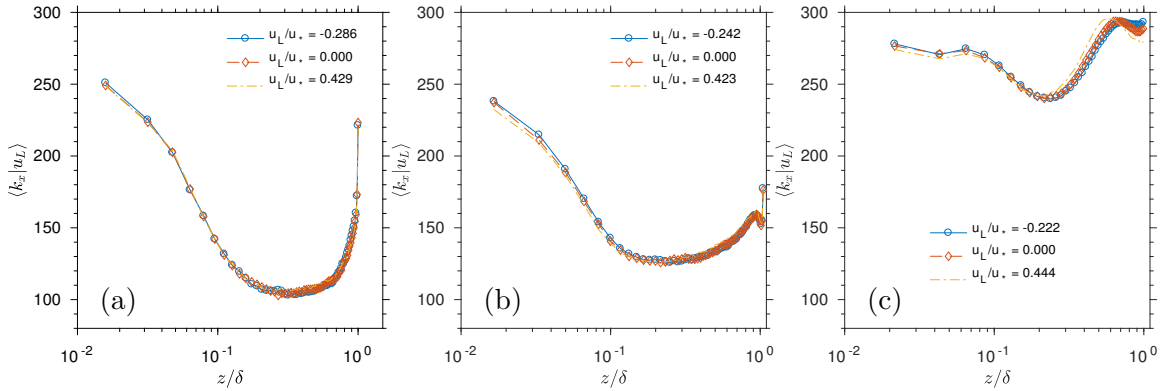


Figure 3.3. The wavenumber quantifying the scale of fluctuation of primary turbulent motions as a function of large-scale fluctuation intensities for the three cases, (a) *CHNL*, (b) *EK10*, and (c) *EK02*.

Table 3.1. Simulation parameters

	Nx	Ny	Nz	\$L_x\$ (Km)	\$L_y\$ (Km)	\$L_z\$ (Km)	\$U_g\$ (m/s)	\$u_*\$ (m/s)	\$\delta\$ (m)	\$Ro\$	\$f(s^{-1})\$
<i>EK10</i>	2048	2048	64	120	120	1.5	10	0.41	1433.00	67	\$10^{-4}\$
<i>EK02</i>	2048	2048	64	120	120	0.75	2	0.09	550.69	33	\$10^{-4}\$
<i>CHNL</i>	2048	2048	64	120	120	1.5	0	0.42	1500.00	-	-

Table 3.2. Wavelet decomposition levels and corresponding normalised horizontal length scales (r_m/δ) and wavenumbers ($k_m\delta$) of all three cases.

Wavelet Decomposition Level (m/n)	CHNL		EK10		EK02	
1	r_m/δ	$k_m\delta$	r_m/δ	$k_m\delta$	r_m/δ	$k_m\delta$
2	42.666	0.147	44.66	0.140	116.21	0.0541
3	21.333	0.294	22.33	0.281	58.109	0.1081
4	10.666	0.589	11.16	0.562	29.054	0.2163
5	5.333	1.178	5.582	1.125	14.527	0.4325
6	2.666	2.356	2.791	2.250	7.2637	0.8650
7	1.333	4.712	1.395	4.501	3.6319	1.7300
8	0.666	9.424	0.697	9.003	1.8159	3.4600
9	0.33	18.849	0.348	18.00	0.9080	6.9201
10	0.166	37.699	0.174	36.01	0.4540	13.840
	0.083	75.398	0.087	72.02	0.2270	27.680

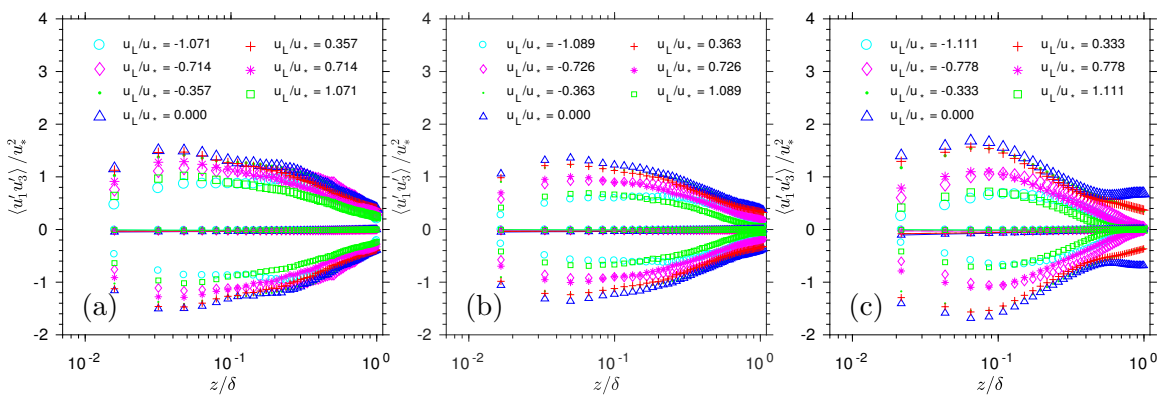


Figure 3.4. The wall-normal Reynolds shear stress, $u'w'$, normalized by the surface shear stress as a function of large-scale fluctuations and distance in the wall-normal direction for each of the cases, (a) CHNL, (b) EK10, and (c) EK02. Solid lines correspond to the mean shear stress, $\langle u'w' \rangle_{u_L}$, and points correspond to $\pm 3\sigma_{u_L}^{u'w'}$.

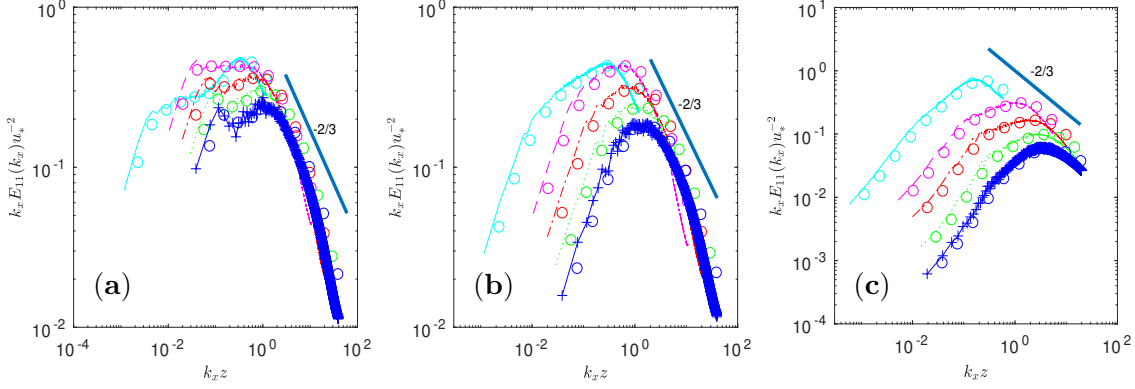


Figure 3.5. Premultiplied wavelet and Fourier spectra of streamwise velocity component, averaged over spanwise direction for (a) *CHNL*, (b) *EK10*, and (c) *EK02* at different wall-normal locations. Spectra are plotted against wavenumbers normalized by height. Lines represent Fourier spectra and circles represent wavelet spectra. Line types $-,-,-,$ $\dots,-,+$ correspond to heights $(0.01\delta, 0.14\delta, 0.26\delta, 0.39\delta, 0.52\delta)$ for *CHNL*, $(0.01\delta, 0.14\delta, 0.28\delta, 0.41\delta, 0.54\delta)$ for *EK10*, and $(0.04\delta, 0.19\delta, 0.34\delta, 0.54\delta, 0.71\delta)$ for *EK02*.

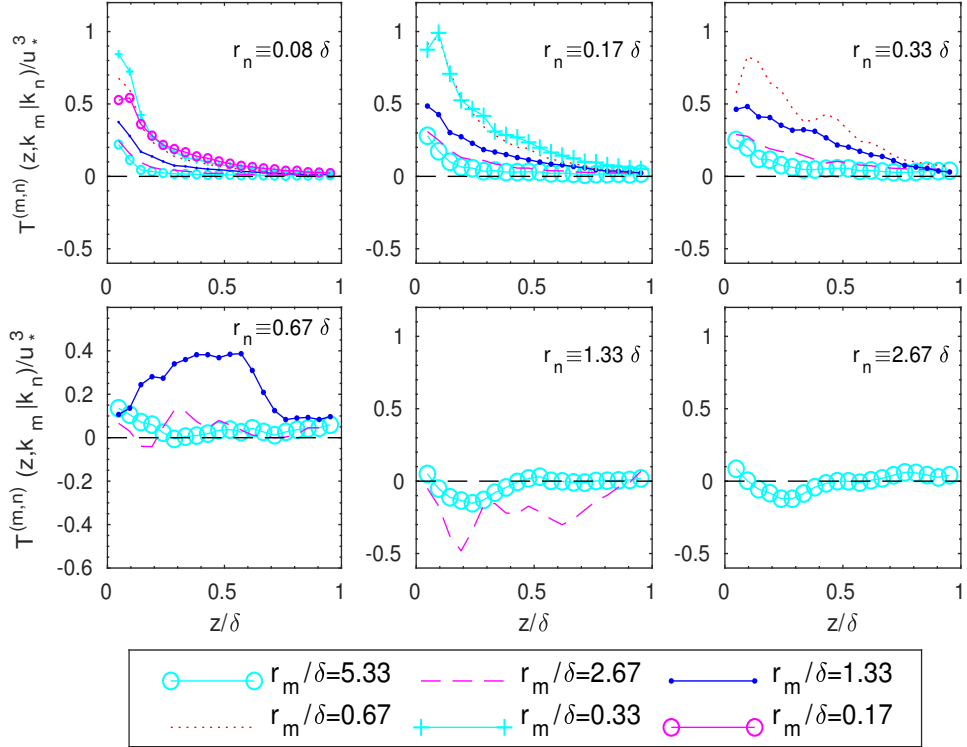


Figure 3.6. Wavelet dual bi-spectrum of subgrid scale transfer normalized by u_*^3 for the *CHNL* case. This figure shows the rate of energy transfer over unit area per unit length of scale where energy transfer occurs from scales r_m/δ to scales smaller than r_n/δ .

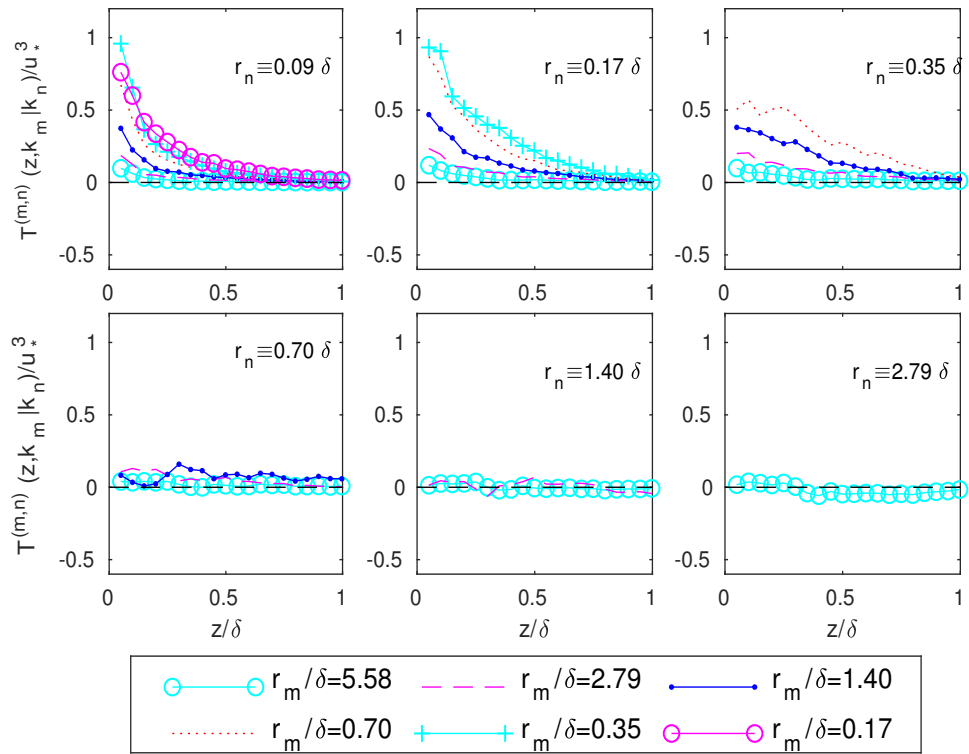


Figure 3.7. The rate of energy transfer over unit area per unit length of scale is shown for the EK10 case where energy transfer occurs from scales r_m/δ to scales smaller than r_n/δ . Energy transfer is normalized by u_*^3 .

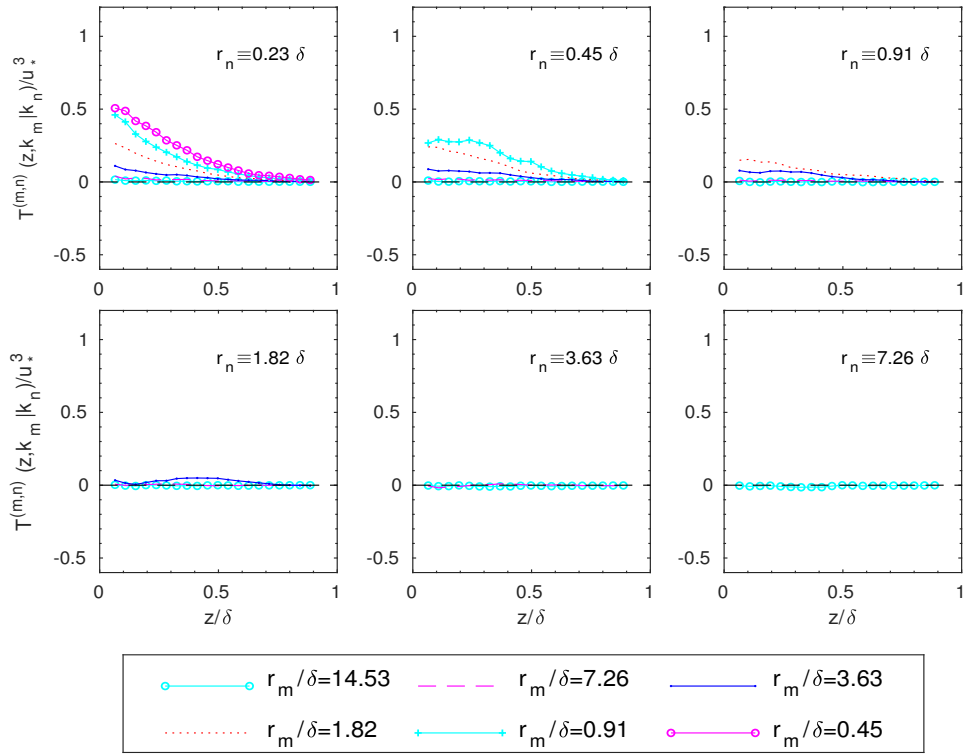


Figure 3.8. Wavelet dual bi-spectrum of subgrid scale transfer normalised by u_*^3 for EK02. Energy transfer is measured over unit area per unit length of scale and transfer occurs from scales r_m/δ to scales smaller than r_n/δ .

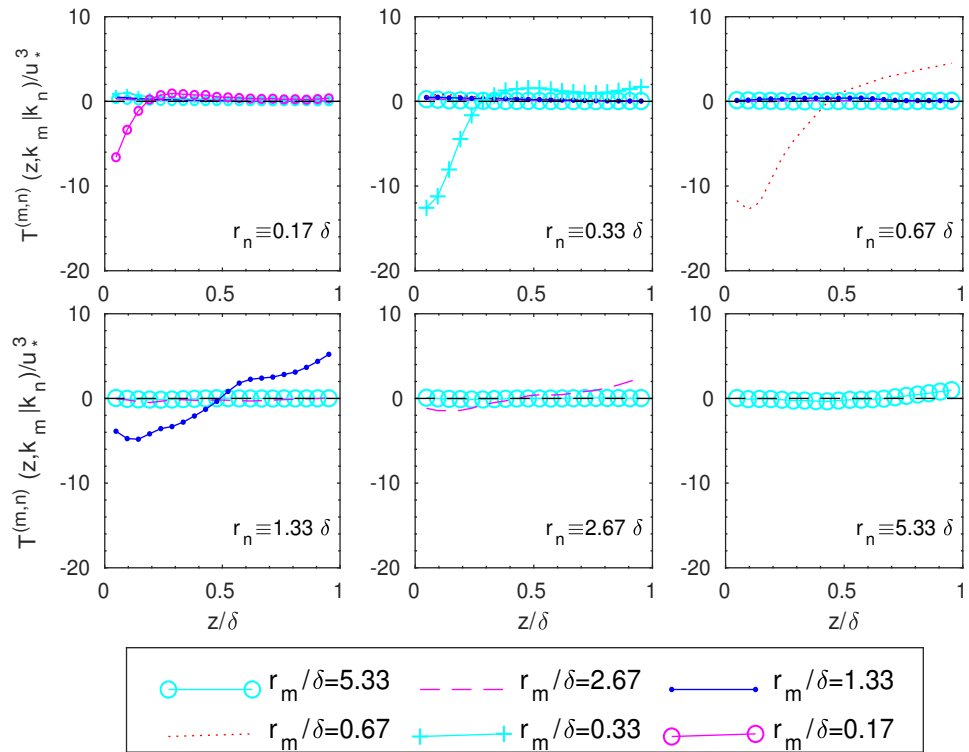


Figure 3.9. Wavelet dual bi-spectrum of subgrid scale transfer normalised by u_*^3 for the CHNL case. In contrast to Fig. 3.6, this figure shows the transfer occurring between length scales r_m to r_m ($r_n \equiv r_m$)

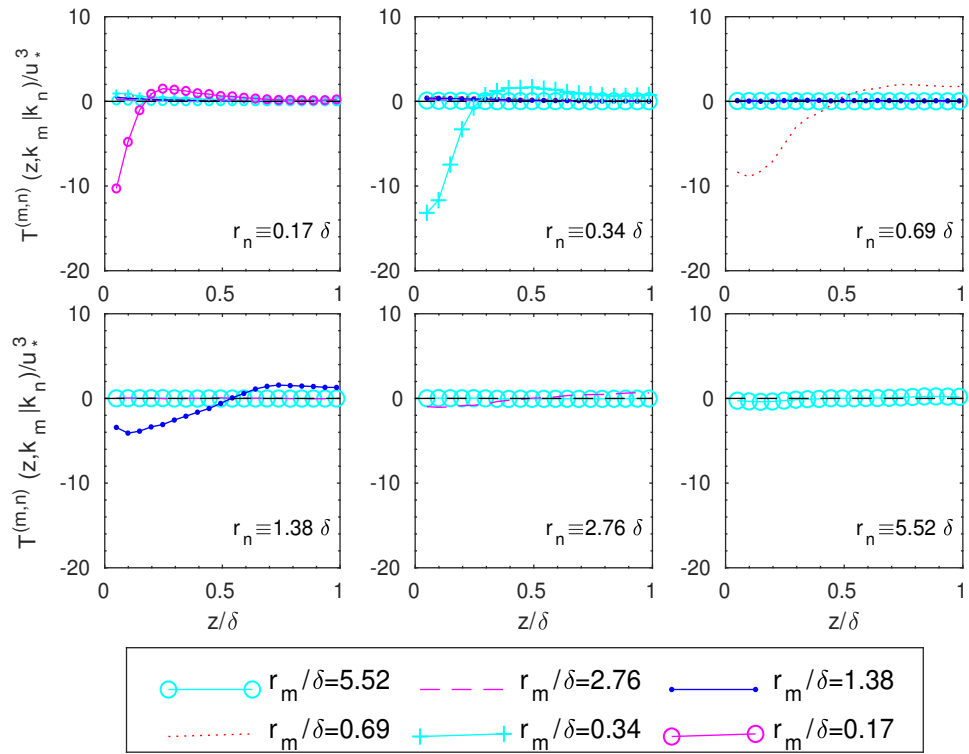


Figure 3.10. Wavelet dual bi-spectrum of subgrid scale transfer normalised by u_*^3 for the EK10 case. In contrast to Fig. 3.7, this figure shows the transfer occurring between length scales r_m to r_m ($r_n \equiv r_m$)

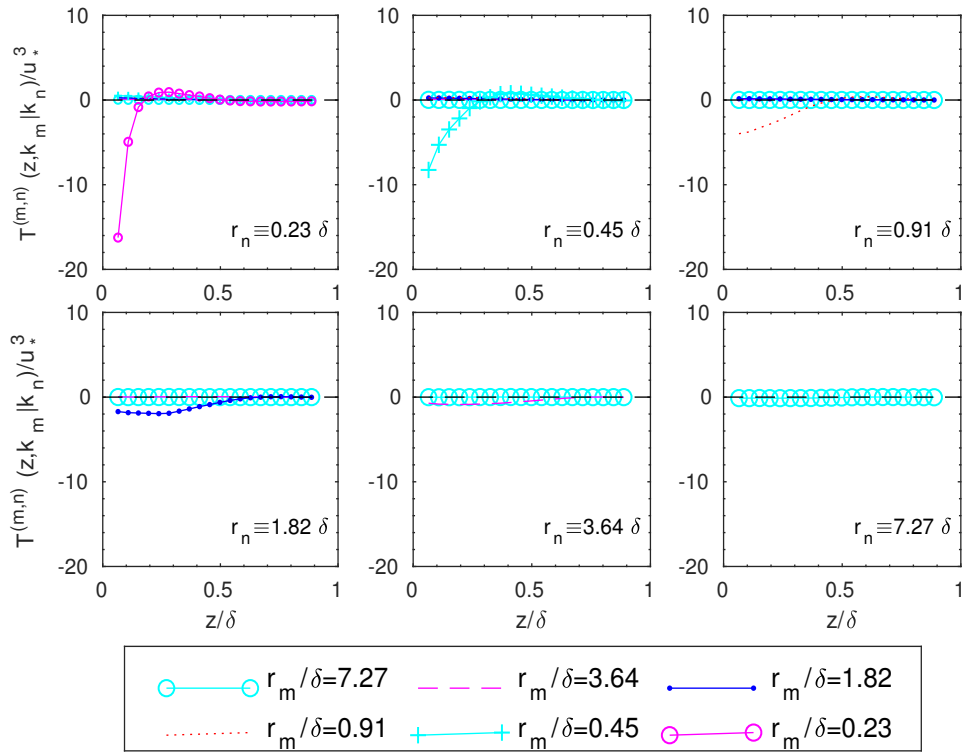


Figure 3.11. Wavelet dual bi-spectrum of subgrid scale transfer normalised by u_*^3 for the EK02 case. The energy transfer from scale r_m to $r_n (\equiv r_m)$ is shown in contrast to Fig. 3.8 where, $r_n < \frac{1}{2}r_m$.

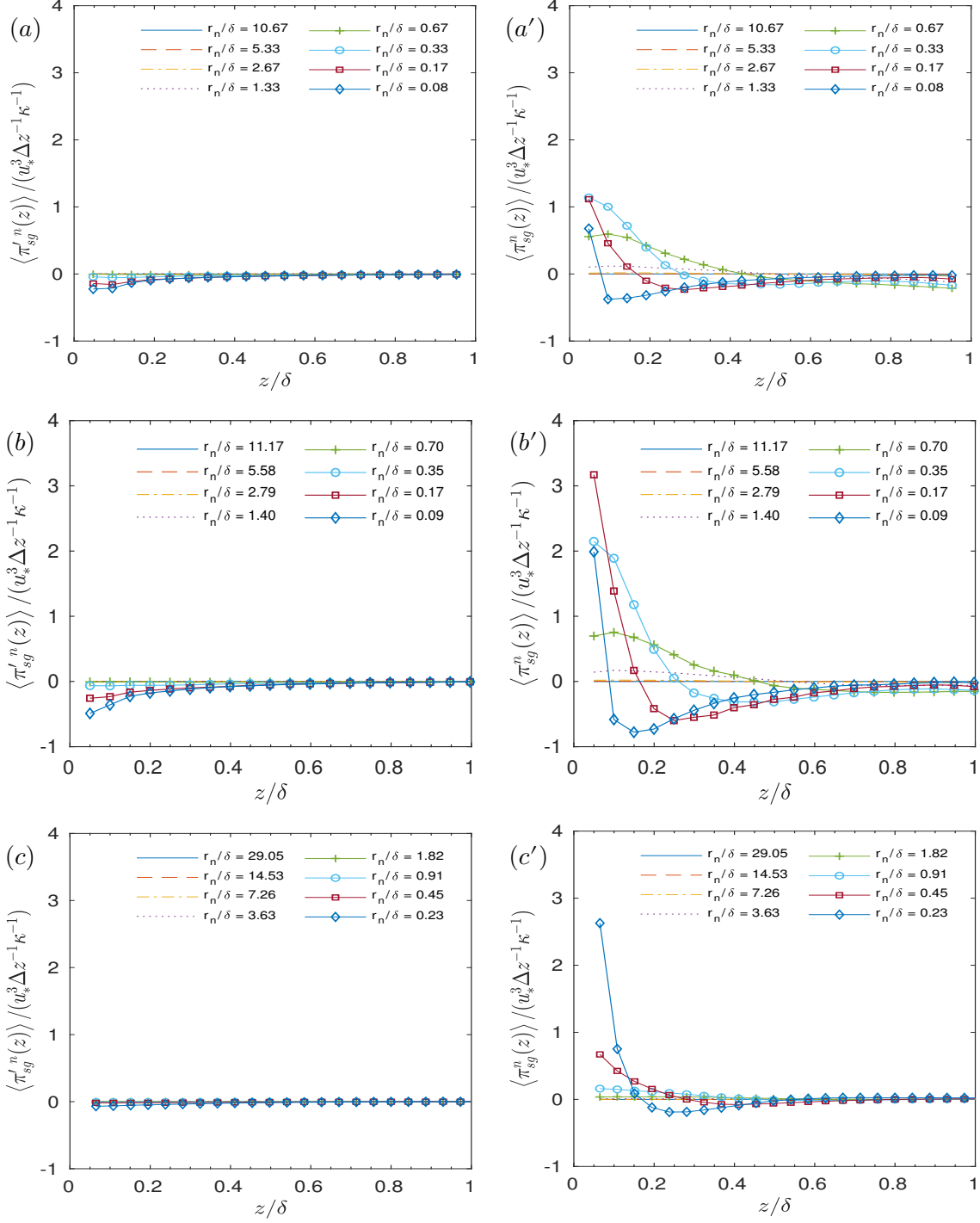


Figure 3.12. Aggregate subgrid scale energy transfer from large to small scales separated by an arbitrary cut-off scale. For panels on the left, total subgrid transfer is calculated using Eqn. 3.27 and the right-hand side panels correspond to total subgrid transfer calculated following the definition in Eqn. 3.26.

CHAPTER 4

TIME SCALE OF VERY LARGE SCALE MOTIONS

Dynamic Mode Decomposition (DMD) has been used to study the time scale of Very Large Scale Motions (VLSMs) in the atmospheric boundary layers. While the length scales of VLSMs have been identified in previous studies, the time scale of evolution has not been identified objectively. It was reported in the earlier studies that VLSMs convect with a velocity lower than the local mean velocity. The time scales of VLSMs were found to be much larger than the large eddy turnover time, which is in line with the previous findings. DMD results also show that low-momentum and high-momentum regions appear alternatively in the spanwise direction as was observed from experiments and other visualization methods. However, the spanwise extent of the VLSMs appears to be significantly lower than what was estimated by earlier studies.

4.1 Introduction

Understanding the hierarchy of scales and how these scales interact is fundamental towards understanding turbulent flow phenomena and devising mechanisms to control turbulent mixing processes. A common line of inquiry is to examine the spatial organization of turbulent motions at different scales using flow visualization technique. Typically, a visualization experiment is carried out using a passive scalar as a tracer. Such experiments can reveal the presence of multiple hierarchical scales and their relative motions. For example, a silhouette image of a large-scale structure resulting from the conglomeration of finer scale motions has been captured in Boundary Layer (BL) flows [81, 82]. These visualization experiments by Falco [81] and Hommema and Adrian [82] provided insight on the organization of large-scale motions in the BL including the visual identification of inclined ramp like structures previously identified. However, Hussain [83] discussed caveats of visualisation technique and emphasizes that caution must be taken in interpretation

of scalar marked boundary lines of structures. Still, when a sufficient description of the flow field is available from a simulation or experiment, data driven modeling can be used as a surrogate of the experimental methods while avoiding some of the limitations of experimental methods. One of the convincing qualities of data-driven methods is that they do not heavily depend on the use of subjective parameters as used in conventional conditional averaging. Among the data-driven techniques, mainly two methods, i.e., Proper Orthogonal Decomposition (POD) [eg., 84, 85] and Dynamic Mode Decomposition (DMD). [eg., 85, 86, 87] have been used widely. Taira et al. [88] summarized the most important strengths and weaknesses of both methods.

A general strategy of studying flow structures is to project velocity fields on to different basis vectors i.e., Fourier modes, empirical eigen vectors, and discrete wavelet basis vectors. The velocity field is usually decomposed as a linear combination of orthogonal basis functions at a given time as $u(\mathbf{x}, t) = \sum_k a_k \phi_k(\mathbf{x}, t)$ where $\phi_k(\mathbf{x})$ represents the basis vectors and a_k represents coefficients of the projections. Alternatively, it is possible to decompose the velocity field into a fixed set of orthogonal spatial functions with time-dependent projection coefficients, i.e., $u(\mathbf{x}, t) = \sum_k a_k(t) \phi_k(\mathbf{x})$ where $u(\mathbf{x}, t)$ denotes a velocity field, $a_k(t)$ denotes the time-dependent coefficients of projection, and $\phi_k(\mathbf{x})$ denotes orthogonal spatial functions capturing the spatial description of the field [88]. Such a decomposition underpins the Galerkin projection schemes used in computational fluid dynamics [89, 90] and form the basis of the Proper orthogonal Decomposition (POD), which is a common tool to identify the spatial structures of energetic scales in a turbulent flow and has been used to study the spatial structure of Very Large Scale Motions (VLSMs) [91, 92]. However, to study the temporal evolution of motions at any scale, a POD based gelarkin projection scheme must be adopted to determine the time dependent expansion coefficients. A POD basis is extracted from a full-scale simulation and then the system is modeled on a reduced set of the POD bases. Next, proper boundary and initial conditions for the new basis are set before solving the resultant system of ordinary differential equations in order to determine the time-dependent expansion coefficients ($a_k(t)$) [eg., 93]. If only the spatial structure coherent motions is of interest, determining the spatial basis vectors $\phi_k(\mathbf{x})$ is sufficient. Many studies have used POD to this end [eg., 84, 85].

The relatively new method of modal decomposition, namely Dynamic Mode Decompo-

sition (DMD), is advantageous in short time flow evolution studies. DMD is completely data driven and does not require any knowledge of the underlying conservation laws that govern the dynamics, unlike POD method. Another attractive feature of DMD is that it can isolate dynamic structures with a particular frequencies where POD modes can correspond to a mix of frequencies. This feature makes DMD useful to isolate and rank structures that evolve at different time scales and study their spatial patterns. DMD have been successfully used to identify structures behind bluff bodies, but has so far not been used to characterize VLSMs in the high Reynold's number boundary layer where the only restriction on scale separation is the dynamic range of the simulation and experimental data in contrast to finite Reynold's number direct numerical simulation studies. In this study, DMD is used to study the spatial and temporal characteristics of VLSMs in the atmospheric boundary layers under two different forcing conditions.

4.2 Large Eddy Simulation

Large Eddy Simulation (LES) was carried out to simulate an Ekman layer and flow in a channel. Resolution in horizontal and vertical directions were 62.5 m and 7.89 m , respectively. The same numerical LES code along with the same subgrid-scale model that was used to study VLSM characteristics in Chapters 2 and 3 has been used to generate the flow fields (see Sec. 2.2 and 3.2). However, to keep the computational cost of the DMD analysis within a reasonable limit, grid points in horizontal directions were reduced to 768 and in the vertical direction, a total of 96 grid points. The flow domain spanned 48 Km in the horizontal (x, y) directions and 750.0 m in the wall-normal direction (z) for *EK02* and 1500.0 m for *CHNL*. The parameters of the simulations are shown in Table 4.1. The reduced domain size here should not pose any limitations to the evolution of VLSMs because the results in Chapter 2 confirms that the maximum length scale of VLSMs is no larger than 25δ .

4.3 Dynamic Mode Decomposition

DMD can be applied to experimental and numerical data sets alike. This analysis provides dynamic modes that evolve with certain frequencies and are associated with a decay or growth rate. The dynamic modes are composed of recognizable spatial patterns

that can be interpreted as organizational units of fluid flow fields or loosely as eddies. The DMD method approximates the state of a system, e.g., as a component of the velocity field, $u \in R^N$ from one time instance (m) to another ($m + 1$) with the Koopman operator A as

$$u_{m+1} = Au_m . \quad (4.1)$$

An ensemble of M snapshots of u obtained with a fixed time interval Δt between snapshots can be organized in two matrices X and Y

$$X = [u_1 \ u_2 \ \cdots \ u_{M-1}], \quad (4.2)$$

$$Y = [u_2 \ u_3 \ \cdots \ u_M] , \quad (4.3)$$

which using Eqn. 4.1 can be rewritten as

$$X = [u_1 \ Au_1 \ \cdots \ A^{M-2}u_1], \quad (4.4)$$

$$Y = [Au_1 \ A^2u_1 \ \cdots \ A^{M-1}u_1]. \quad (4.5)$$

The columns of X and Y are each elements of a Krylov subspace and the last vector in Y can be approximated within the span of the Krylov subspace in an L^2 sense [94] as

$$u_M = \sum_{i=1}^{M-1} b_i u_i + r, \quad (4.6)$$

where b_i are the coefficients of the Krylov space vectors and r is the residual. Schmid [95] suggests that after a critical number of snapshots, adding more snapshots in X or Y , i.e., any more columns, would not improve the vector space spanned by X and at this point, the last data vector approximation (Eqn. 4.6) would not improve any more. This could practically serve as a limit to the number of snapshots used in calculation. Up until this point, the Koopman operator A is unknown. The key idea of DMD is to find an approximation to the eigen vectors and eigen values of A . From 4.4 and 4.5, a transformation relationship between X and Y can be expressed as

$$Y = AX. \quad (4.7)$$

This matrix equation can also be rewritten following Eqn. 4.6 as

$$Y = XS + re_{M-1}^T, \quad (4.8)$$

where $e_{M-1} \in R^{(M-1) \times 1}$ is the $(M-1)$ th unit vector, $r \in R^{N \times 1}$, and $S \in R^{N \times (M-1)}$ is a matrix of the companion type and assumes the form

$$S = \begin{bmatrix} 0 & \cdots & 0 & b_1 \\ 1 & \ddots & 0 & b_2 \\ 0 & \ddots & \ddots & \vdots \\ & \ddots & \ddots & 0 & b_{M-2} \\ 0 & \cdots & 0 & 1 & b_{M-1} \end{bmatrix}. \quad (4.9)$$

The last column of S contains the unknown coefficients of Eqn. 4.6. Eigen values of S approximate some of the eigen values of A . However, calculating matrix S requires the operator A to be known to proceed with an Arnoldi algorithm. Schmid [95] suggested calculating a matrix \tilde{S} instead of S , where \tilde{S} is a similar matrix to A . Utilizing reduced singular value decomposition of the data matrix X and following Eqn. 4.7, \tilde{S} can be calculated from

$$U^*AU = U^*YW\Sigma^{-1} \equiv \tilde{S}, \quad (4.10)$$

where $X = U\Sigma W^*$. At this point, the following eigen value problem is solved,

$$\tilde{S}y_k = \mu_k y_k \quad (4.11)$$

where the eigen values μ_k capture the time dynamics of the discrete Koopman operator A [94]. DMD modes ϕ_k are obtained when the eigen vectors y_k are projected to the reduced column space of X as

$$\phi_k = Uy_k. \quad (4.12)$$

The future state of the flow field at any time $n\Delta t$ can be predicted from DMD modes,

$$x_n = \sum_{k=1}^K b_k \phi_k(x) \exp(\omega_k t), \quad (4.13)$$

or in matrix form,

$$x_{DMD}(t) = \Phi \operatorname{diag}(\exp(\omega t))b, \quad (4.14)$$

where $\omega_k = \ln(\mu_k)/\Delta t$, Φ is a matrix whose columns are the eigen vectors y_k and b_k are the initial amplitudes of each mode. The b_k amplitudes are obtained from the equation, $x_1 = \Phi b$, using Moore-Penrose pseudo-inverse Φ^+ such that,

$$b = \Phi^+ x_1. \quad (4.15)$$

The algorithm as has been described was first proposed by Schmid [95] and a more elaborate version can be found in [94, 96, 97]. This is the most widely used DMD algorithm, although

a proliferation of modified DMD algorithms exists that have been observed to have a finer separation of multiscale spatio-temporal features [eg., 98], can handle data sampled at irregular time intervals [97], can apply DMD to spatially sub-sampled data [99], and can manage large and streaming datasets [100].

Following the algorithm as has been described, DMD was carried out over 8000 frames for both the cases. For *CHNL*, the constant time spacing between consecutive frames (Δt) was 0.1 sec. and for *EK02*, it was 2 sec. Since three dimensional DMD analysis is prohibitively expensive in terms of requirement of the Random Access Memory, two-dimensional DMD was carried out on wall parallel and spanwise-vertical planes. Data were extracted at a particular streamwise-spanwise plane from the three dimensional velocity field for all the 8000 time instances and were stacked as columns in the data matrices X and Y to proceed with DMD mode extraction. Each of the matrices X and Y required 37.7 *GB* of memory. In case of full 3D analysis, the matrix size will rise to 3623.8 *GB*.

4.4 Results and Discussion

DMD separates spatial structures that have different frequencies. Here, the frequency distribution of DMD modes at different heights was examined for both cases. A series of 8000 frames that were equally spaced in time scale was analyzed resulting in 8000 DMD modes that were sorted based on frequency (μ_k). Modes having zero frequency were excluded from analysis because these modes would constitute the mean flow field. Time periods of 5-10 representative DMD modes are categorized against normalized height in Table 4.2 for *CHNL* and in Table 4.3 for *EK02*. DMD time periods (ΔT) are the inverse of the pure sine or cosine frequencies that correspond to the DMD eigen values and they are normalized with large length and velocity scales ($\Delta T/(\delta/U(\delta))$) where ($\delta/U(\delta)$) constitutes large eddy turnover time where and $U(\delta)$ is the mean velocity at the top of the boundary layer. Differences between frequencies of the first few modes resolved at different heights are observed, although for any particular mode, discernible trends with height are not observed. Spatial structures corresponding to DMD modes are shown in Figs. 4.1 and 4.2. To characterise length scales of LSMs and VLSMs comprised of low-speed fluid, velocity fields were reconstructed from the individual DMD modes at selected heights to be utilized in the structure detection procedure. To identify structures of different length scales an

alternative definition adopted in Chap. 2 was used, i.e., a connected region of low-speed fluid in the binarized flow field. In case of *CHNL*, DMD modes with normalized time periods of 12.91, 6.76, 5.75, 4.74 as categorically presented against normalized height of 0.50δ in Table 4.2 were analysed. In case of *EK02*, the DMD modes with normalized time periods of 136.5, 37.65, 21.86, 15.17 at a height of 0.48δ were selected. The key observation that emerges from Fig. 4.3 is that contrary to primary expectation, a particular DMD mode does not isolate a single length scale. Any DMD mode is observed to comprise a distribution of length scales. So, while DMD modes can perfectly isolate dynamics based on time scale, the isolation of coherent spatial structure may not be clean.

From the results, it is also apparent that structures that evolve over a very long time scale can be obtained in both the log and wake layers. Since a linear proportionality between the time scale and the length scale can be established following Taylor's frozen turbulence hypothesis, it can be inferred that the DMD modes with long time period would correspond to long length scales. However, an observation Fig. 4.3 suggests otherwise. Fig. 4.3(a) shows the normalized histogram of the size distribution of the structures in the reconstructed velocity field for the *CHNL* and Fig. 4.3(b) shows the same for *EK02*. A limit in the length scale of the identified structures is observed, e.g., for *EK02* the maximum identified normalized length scale is 15, whereas the normalized DMD time scale is 37.4.

DMD is sensitive to the sampling frequency and follows Nyquist-Shannon sampling theorem. For the *CHNL* case, sample velocity fields were collected every 0.1 sec and for *EK02*, the sampling rate was 2 sec. Therefore, for *CHNL*, any process that evolves with a time period of less than 0.2 sec would not be captured by the DMD decomposition and for *EK02*, that time period would be any less than 4 sec. Since this study is concerned with LSMs and VLSMs that are presumed to correspond with very long time scales, these sampling frequencies should be sufficient. The ratio between the sampling rate of *EK02* and *CHNL* is 20. This difference is reflected in the obtained time periods of DMD modes. A comparison between Tables 4.2 and 4.3 show that the time period of the first few modes of *EK02* can be as large as 11 times larger than that of *CHNL*. However, in *EK02*, the DMD modes that appeared with very large time periods do not show any coherent motions that corresponds to the expected shape or length scales of VLSMs or LSMs. For example, DMD mode with characteristic normalized time scales of 136.50, 37.65, 21.86 as portrayed

in Fig. 4.2 show less prominence of VLSMs as is apparent from Fig. 4.3(b), which shows the distribution of length scales. These modes that correspond to very large time periods that also do not show recognizable coherence in the plots will most likely appear as zero modes if sampling period was lower.

An overall observation from the Tables 4.2 and 4.3 and plots in Fig. 4.3 is that VLSMs persist for a long period of time compared to their length scale. The existence of smaller scale motions are also observed in the scale distribution of slow DMD modes as shown in Fig. 4.3.

4.5 Summary and Conclusions

Large eddy simulations were carried out to study the structure of VLSMs in a pressure-driven channel flow and in an Ekman layer flow. Eight thousand successive frames were recorded from the simulation to investigate the time and length scale of VLSMs using the DMD method. DMD method produced constituent DMD modes that correspond to individual frequencies and could project the temporal evolution of the velocity field over a period of time. The spatial pattern of the individual DMD modes corresponding to a range of frequencies within the time scale of interest were investigated to understand the spatial structure of the VLSMs. It was observed that while DMD method could isolate modes evolving under different frequencies, the spatial patterns were not distinctively unique for any of the modes. Using image processing techniques and under the assumption that connected regions on a thresholded velocity field constitute coherent structures, the reconstructed velocity fields from DMD modes were analysed. It was observed that each DMD mode contained various length scales. The results showed that within the spatial structure of any DMD mode, LSMs were dominant in numbers and the existence of VLSMs with length scales greater than 10δ was rare. The results also indicated that VLSMs and LSMs can evolve over a longer time scale compared to their expected advection time scale estimated from Taylor's frozen turbulent hypothesis.

4.6 References

- [81] R. E. Falco. Coherent motions in the outer region of turbulent boundary layers. *The Physics of Fluids*, 20, 1977.
- [82] Scott E. Hommema and Ronald J. Adrian. Packet structure of surface eddies in the

- atmospheric boundary layer. *Boundary-Layer Meteorology*, 106:147–170, 2003.
- [83] A. K. M. Fazle Hussain. Coherent structures and turbulence. *Journal of Fluid Mechanics*, 173, 1986.
- [84] Dan Li and Elie Bou-Zeid. Coherent structures and the dissimilarity of turbulent transport of momentum and scalars in the unstable atmospheric surface layer. *Boundary-Layer Meteorology*, 140(2):243–262, Aug 2011. ISSN 1573-1472. doi: 10.1007/s10546-011-9613-5. URL <http://dx.doi.org/10.1007/s10546-011-9613-5>.
- [85] Tomas W. Muld, Gunilla Efraimsson, and Dan S. Henningson. Flow structures around a high-speed train extracted using proper orthogonal decomposition and dynamic mode decomposition. *Computers & Fluids*, 57:87 – 97, 2012. ISSN 0045-7930. doi: <http://dx.doi.org/10.1016/j.compfluid.2011.12.012>. URL <http://www.sciencedirect.com/science/article/pii/S0045793011003847>.
- [86] Shervin Bagheri. Koopman-mode decomposition of the cylinder wake. *Journal of Fluid Mechanics*, 726, 2013.
- [87] Yingzheng Liu and Qingshan Zhang. Dynamic mode decomposition of separated flow over a finite blunt plate: time-resolved particle image velocimetry measurements. *Experiments in Fluids*, 56(7):148, 2015.
- [88] Kunihiko Taira, Steven L. Brunton, Scott T. M. Dawson, Clarence W. Rowley, Tim Colonius, Beverley J. McKeon, Oliver T. Schmidt, Stanislav Gordeyev, Vassilios Theofilis, and Lawrence S. Ukeiley. Modal analysis of fluid flows: an overview. *eprint arXiv:1702.01453*, 2017.
- [89] Clarence W Rowley, Tim Colonius, and Richard M Murray. Model reduction for compressible flows using pod and galerkin projection. *Physica D: Nonlinear Phenomena*, 189(1):115–129, 2004.
- [90] Dieter Armbruster, Randy Heiland, and Eric J. Kostelich. Kltool: A tool to analyze spatiotemporal complexity. *Chaos (Woodbury, N.Y.)*, 4, 1994.
- [91] Leo H. O. Hellström, Aman Sinha, and Alexander J. Smits. Visualizing the very-large-scale motions in turbulent pipe flow. *Physics of Fluids*, 23(1):011703, 2011. doi: 10.1063/1.3533016. URL <http://dx.doi.org/10.1063/1.3533016>.
- [92] Sean C. C. Bailey, B. N. and Alexander J. Smith. Experimental investigation of the structure of large- and very-large-scale motions in turbulent pipe flow. *Journal of Fluid Mechanics*, 651:339–356, 2010. doi: 10.1017/S0022112009993983.
- [93] Giovanni Stabile, Saddam Hijazi, Andrea Mola, Stefano Lorenzi, and Gianluigi Rozza. Advances in reduced order modelling for cfd: vortex shedding around a circular cylinder using a pod-galerkin method. *arXiv preprint arXiv:1701.03424*, 2017.
- [94] J. Nathan Kutz. Dynamic mode decomposition. In *Data-driven modeling & scientific computation Methods for Coomplex Systems & Big Data*. Oxford University Press, 2013.
- [95] Peter J. Schmid. Dynamic mode decomposition of numerical and experimental data. *Journal of Fluid Mechanics*, 656, 2010.

- [96] Clarence W. Rowley, Igor Mezić, Shervin Bagheri, and Philipp schlatter. Spectral analysis of nonlinear flows. *Journal of Fluid Mechanics*, 641, 2009.
- [97] Jonathan H. Tu. *Dynamic mode decomposition: theory and applications*. PhD thesis, Princeton University, 2013.
- [98] J. Nathan Kutz, Xing Fu, and Steven L. Brunton. Multiresolution dynamic mode decomposition. *SIAM Journal on Applied Dynamical Systems*, 15, 2016.
- [99] Florimond Guéniat, Lionel Mathelin, and Luc R. Pastur. A dynamic mode decomposition approach for large and arbitrarily sampled systems. *Physics of Fluids*, 27, 2015.
- [100] Maziar S. Hemati, Matthew O. Williams, and Clarence W. Rowley. Dynamic mode decomposition for large and streaming datasets. *Physics of Fluids*, 26, 2014.

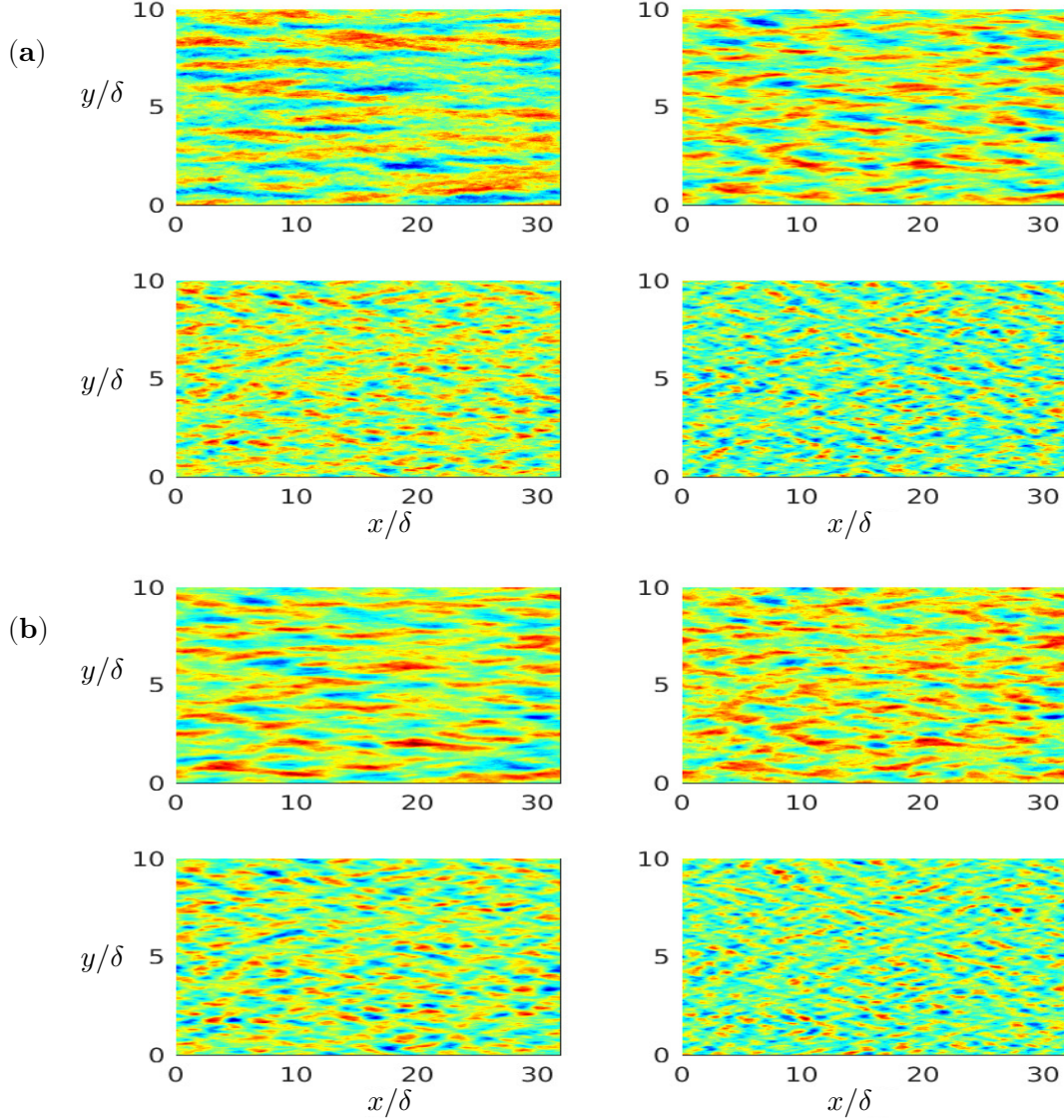


Figure 4.1. First four DMD modes with characteristic time period as listed in Table 4.2 at heights 0.047δ and 0.095δ for the *CHNL* case are shown in subfigure (a) and (b), respectively. In subfigure (a), top left panel shows spatial mode corresponding to normalized time period ($\Delta TU(\delta)/\delta$) of 27.09 and top right, bottom left, bottom right panels correspond to 10.19, 6.11, 4.63, respectively. In subfigure (b) panels beginning from top left corner in the clockwise order corresponds to normalized time periods 14.05, 8.78, 5.65, and 4.07, respectively.

Table 4.1. Simulation parameters

	N_1/N_2	N_3	$L_1/L_2(\text{Km})$	$L_3 (\text{Km})$	$\delta(\text{m})$	Ro
<i>EK02</i>	768	96	48	0.75	563	33
<i>CHNL</i>	768	96	48	1.5	1500	-

Table 4.2. Time period of evolution of the first five DMD modes normalized by $\delta/U(z)$ for *CHNL*. Modes were calculated at different horizontal planes characterized by normalized heights presented.

Normalized Height	Mode 1	Mode 2	Mode 3	Mode 4	Mode 5
0.047δ	27.09	10.19	6.11	4.63	3.48
0.095δ	14.05	8.78	5.65	4.07	3.16
0.2δ	32.07	11.68	6.49	5.01	3.75
0.33δ	50.59	12.87	7.22	4.93	3.94
0.50δ	12.91	6.76	5.75	4.74	3.70

Table 4.3. Statistics of the first five DMD modes for *EK02*. DMD time periods are normalized by $\delta/U(z)$. Modes were calculated at different horizontal planes characterized by normalized heights presented.

Normalized Height	Mode 1	Mode 2	Mode 3	Mode 4	Mode 5
0.04δ	115.5	38.6	22.4	15.4	11.7
0.21δ	113.4	34.8	20.4	14.7	11.4
0.32δ	100.2	35.6	20.8	14.7	11.4
0.48δ	135.7	37.4	21.7	15.0	11.6

Normalized Height	Mode 6	Mode 7	Mode 8	Mode 9	Mode 10
0.04δ	9.6	8.1	7.5	7.0	6.2
0.21δ	9.5	8.1	7.1	6.2	5.5
0.32δ	9.4	7.9	7.1	6.2	5.5
0.48δ	9.5	8.0	7.1	6.2	5.5

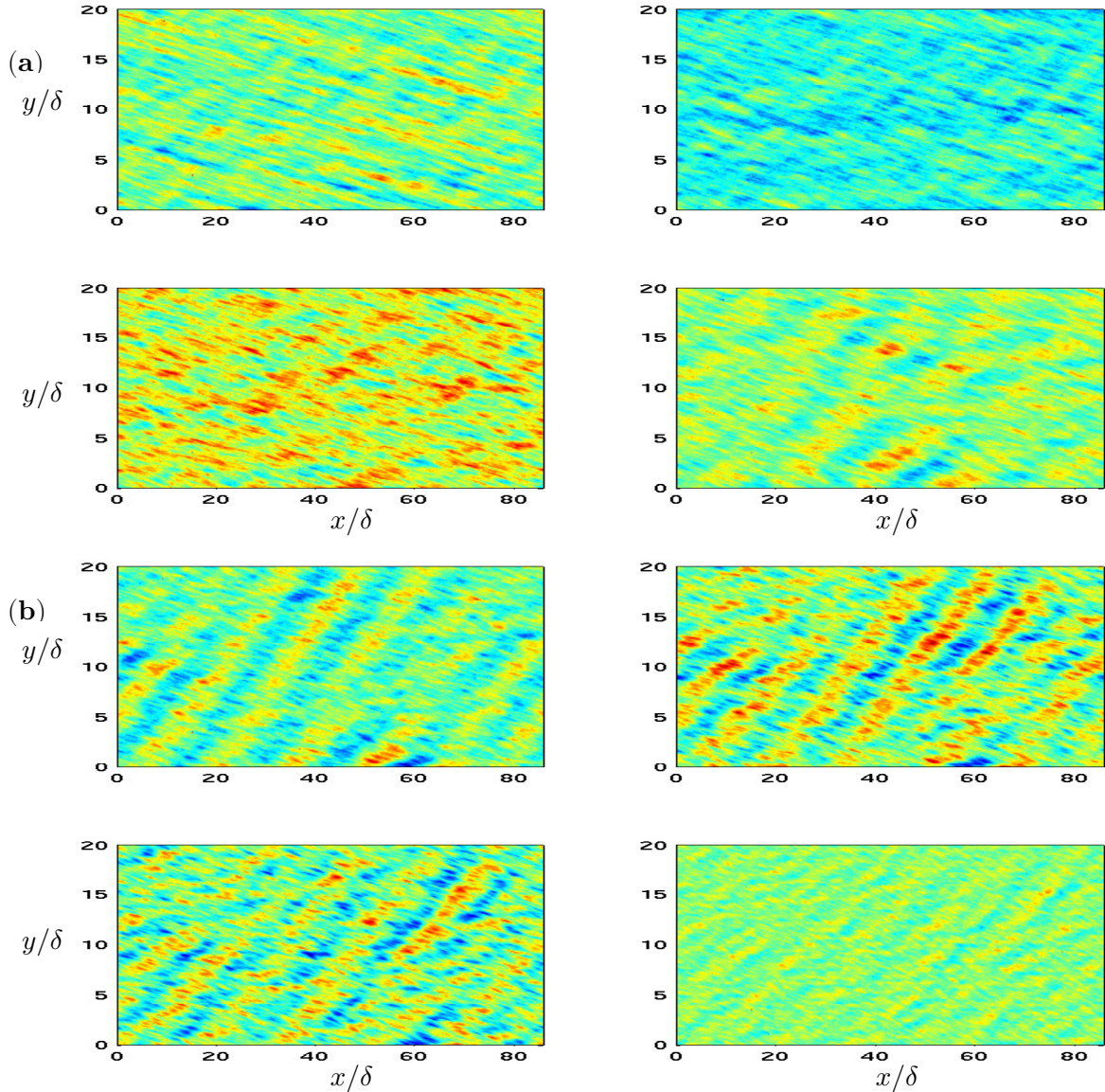


Figure 4.2. DMD modes of different frequencies at a height of 0.48δ are shown for EK02. (a) Four DMD modes in clockwise order beginning from top left panel correspond to normalized time periods of 135.7, 37.4, 21.7, and 15.0. (b) DMD modes with time periods 11.6, 9.5, 8.0, 7.1.

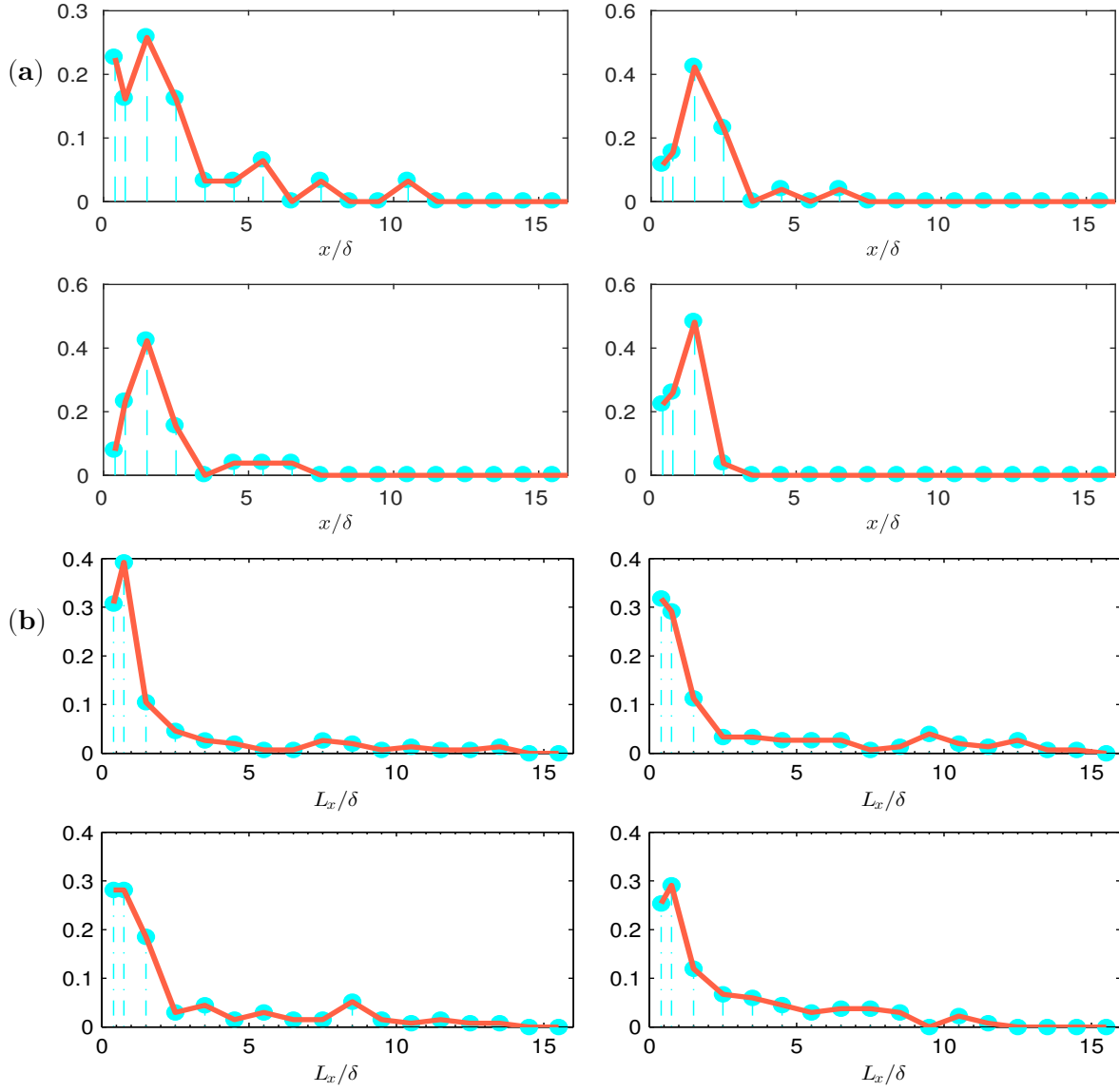


Figure 4.3. Normalized histogram of the length scales of structures detected in the velocity field reconstructed from individual DMD modes. x -axis represents the length scales of structures normalized by the boundary layer depth δ . A discrete set of structures of length scales $\{0.3, 0.5, 1, 2, 3, 4, 5, 6, 7, 8, 9, 10, 11, 12, 13, 14, 15\}\delta$ were searched in the velocity field. Subfigures (a) and (b) represents respectively, *CHNL* and *EK02*. For each of these two cases the four analysed DMD modes correspond to the first four modes as listed in Table 4.2 (at 0.5δ), and 4.3 (at 0.48δ) and are plotted in clockwise fashion beginning from the top left panel of each subfigure.

CHAPTER 5

CONCLUSIONS AND FUTURE DIRECTIONS

This dissertation adds new contributions to the existing scientific literature in regard to understanding Large and Very Large Scale Motions (LSMs & VLSMs) in the atmospheric boundary layer. Along with the introduction of a new way to detect VLSMs and LSMs in simulated flow fields, more established methods and procedures have been utilized to study characteristics of these structures. In this chapter, we summarize the main findings and delineate the future research directions that can address questions that were not within the scope of this dissertation but demand new efforts to advance knowledge on VLSMs, and in understanding of the turbulent flow dynamics in general.

5.1 Summary

While the existence of LSMs and VLSMs was predicted long before a true interest was observed by the scientific community in characterizing them, a lack of a universally accepted definition of VLSMs still plagues the research efforts to properly document their importance and characteristics. Visual cues have always been at the forefront of endeavours in regard to their identification in a flow field. A key contribution of this dissertation is the utilization of the visual characteristics of VLSMs and applying established tools and methods commonly used by the image processing community to identify these structures. In Chapter 2, we developed a new definition of VLSMs as connected regions of pixels that correspond to a section of the probability density function of the velocity distribution and proceeded with the detection of such areas in the velocity field $u(\mathbf{x}, t)$ at a fixed t . Such a detection procedure enabled us to count the occurrences of VLSMs at any wall parallel plane and assess their contributions to shear stresses that can exclusively be attributed to VLSMs. It was observed that VLSMs do not necessarily make a disproportionately bigger contribution towards the shear stress compared to smaller scale counterparts. In fact, based

on the area occupied by the VLSMs, the shear stress contribution of VLSMs was observed to be smaller in the log layer but higher in the outer layer of the BL in comparison to smaller scale structures. The projected 3D structure of VLSMs obtained using conditional averaging showed a difference between structure lengths and widths in different flow fields. It was observed that when rotation is significant in the flow fields, the large scale structures tend to shorten in length and widen in the cross-stream direction compared to those found in canonical pressure-driven channel flows.

It has been previously reported from experimental investigations that VLSMs modulate the small-scale fluctuations. In order to examine whether these experimentally observed phenomena exist in the simulated flow fields and to solidify the fact that these phenomena are universal irrespective of boundary or forcing conditions, the modulation effect of VLSMs were analyzed in Chapter 3. Although previous experiments investigated the modulation effect within the log layer only, strong evidence was found that the modulation effects extended beyond the log layer. In addition to the validation of the modulating effect, interscale energy exchange was analyzed to assess the locality and nonlocality of turbulent kinetic energy transfer for the three flow cases investigated. Any possibility of VLSMs interacting with small-scale motions in a nonlocal fashion due to nonlinearity of the Navier-Stokes equations would imply deviation from the Richardson-Kolmogorov proposed energy cascade scenario and also, that would mean VLSMs could directly modify small scale characteristics. The study of the locality and nonlocality of energy transfer for the very large scale motions poses some challenges due to the fact that the statistical tools available for analysis of turbulence may not be applied to study large-scale motions. As an example, the structure function-based formulations are not suitable for studying VLSMs because length-scale wise the applicability of structure function is limited to the inertial subrange. The *tke* exchange between scales was analyzed in the wavelet domain. It was observed that energy transfer is predominantly local and weak rotation of the reference frame does not have an impact on *tke* transfer characteristics. It can be concluded that in a domain where rotational effects are weak, small scale motions do not receive energy from distant large scales through inertial effects. Also the energy density of large scale in terms of *tke* per unit length-scale per unit area were studied. While the total energy of VLSMs was found to be significant, the energy density per unit length-scale per unit area was found to be negligible compared to that of

small-scale motions.

In Chapter 4, The time period of evolution of VLSMs was studied via Dynamic Mode Decomposition (DMD). Since the u-velocity component was the dominant contributor to the *tke* and defined the overall structure in the velocity field, an analysis of structures in the u-velocity component was undertaken. DMD ranks resultant modes based on frequency and a DMD mode corresponding to a particular frequency typically corresponds to a physical structure or pattern in the velocity field. An ensemble of 8000 successive frames were collected from the simulation and were analyzed resulting in 8000 modes per simulation. Because of our focus on VLSMs, modes with very slow frequencies were studied. Since VLSMs or LSMs correspond to outer scales, the frequency was converted to time period by normalizing with convection velocity at the top of the boundary and the boundary layer height. It was observed that structures of different length scales fell into the same frequency/time period bin. In an ideal case, only one dominant physical structure or pattern along with random noise is expected to correspond to a single time period. However, when analyzed, the high-Re flows showed that several patterns of different length scales correspond to a single mode. In physical context, this means that structures can be advected by larger scale motions without being dissipated by turbulence. The DMD method highlighted that the expected normalized time periods were longer than the expected time period calculated using the frozen turbulence hypothesis for VLSMs and LSMs. This indicates that the advection velocity of VLSMs and LSMs is slower than the mean flow.

Actual flow in the environment is subjected to a complex array of forcing such as Earth's rotation, surface heat flux, gravitational force, and pressure gradients and a multitude of surface conditions such as smooth sea surfaces, urban canopies to mountains, and everything in between. To study the effect of only one forcing condition on the flow, it is necessary to decouple the effect of the desired force or boundary condition from the ensemble. In such a case, simulating the flow becomes invaluable. Accounting for all these effects on VLSMs or LSMs would be a huge undertaking. Here, only the effect of rotation was considered. Evaluating the influence of other forcing and boundary conditions on VLSMs and LSMs is a necessary extension of this study.

Many studies have focused on the importance and defining characteristics of VLSMs and LSMs. This present study also targets the identification and characterization of VLSMs

and LSMs. One issue that must also be addressed is the dynamical development process of the large-scale motions. Several hypotheses have been proposed in that context. The most plausible hypothesis is that LSMs merge together to form VLSMs. LSMs come into existence due to counter rotating vortex rolls. These vortical structures usually extend towards the top of the boundary layer from the ground in the form of hairpin vortices. Such is the view of the attached eddy hypothesis. However, to solidify these arguments, an association must be established between the length scales characterizing the velocity field induced by a vortical structure and the characteristic diameter of the vortical structure. A limited number of studies has focused in this direction.

APPENDIX A

TURBULENT KINETIC ENERGY EQUATION FOR A HORIZONTALLY HOMOGENEOUS, QUASI-STEADY FLOW

The momentum equations for the Ekman layer flows can be simplified under the assumption of horizontal homogeneity and quasi-steady condition. If any generic spatially filtered variable ζ is decomposed into a horizontally averaged ($\langle \zeta \rangle$) and fluctuating components (ζ'), the NS equations can be reduced to the following form:

$$u'_3 \frac{\partial}{\partial x_3} \langle u_i \rangle + \langle u_j \rangle \frac{\partial}{\partial x_j} u'_i + \frac{\partial}{\partial x_j} u'_i u'_j = -\frac{\partial}{\partial x_i} p' - \frac{\partial}{\partial x_i} \langle p \rangle - \frac{\partial}{\partial x_3} \langle \tau_{i3} \rangle - \frac{\partial}{\partial x_j} \tau'_{ij} + f_c \epsilon_{ij3} u_j, \quad (\text{A.1})$$

After further simplification, the NS equations in the x_1 , x_2 , and x_3 directions are as follows for the Ekman layer flow cases *EK10* and *EK02*:

$$u'_3 \frac{\partial \langle u_1 \rangle}{\partial x_3} + \langle u_1 \rangle \frac{\partial u'_1}{\partial x_1} + \langle u_2 \rangle \frac{\partial u'_1}{\partial x_2} + \frac{\partial}{\partial x_j} u'_i u'_j = -\frac{\partial p'}{\partial x_1} - \frac{\partial}{\partial x_3} \langle \tau_{13} \rangle - \frac{\partial \tau'_{ij}}{\partial x_j} + f_c u_2, \quad (\text{A.2})$$

$$u'_3 \frac{\partial \langle u_2 \rangle}{\partial x_3} + \langle u_1 \rangle \frac{\partial u'_2}{\partial x_1} + \langle u_2 \rangle \frac{\partial u'_2}{\partial x_2} + \frac{\partial}{\partial x_j} u'_i u'_j = -\frac{\partial p'}{\partial x_2} + f_c U_g - \frac{\partial}{\partial x_3} \langle \tau_{23} \rangle - \frac{\partial \tau'_{ij}}{\partial x_j} - f_c u_1, \quad (\text{A.3})$$

$$\langle u_1 \rangle \frac{\partial u'_3}{\partial x_1} + \langle u_2 \rangle \frac{\partial u'_3}{\partial x_2} + \frac{\partial}{\partial x_j} u'_i u'_j = -\frac{\partial p'}{\partial x_3} - \frac{\partial}{\partial x_3} \langle \tau_{33} \rangle - \frac{\partial \tau'_{ij}}{\partial x_j}. \quad (\text{A.4})$$

The turbulent kinetic energy (*tke*) equation under the assumption of horizontal homogeneity can be derived within the framework of spatial filtered Navier-Stokes equation by multiplying each Eqn. A.4 by u_i . For convenience, the tilde is dropped and all dependent variables will be understood as spatially filtered quantities. With the proposed decomposition and under the assumption that this horizontal averaging over statistically independent

frames conforms to Reynold's averaging, the transport equation for the turbulent kinetic energy (q) takes the following form:

$$u'_3 u'_i \frac{\partial \langle u_i \rangle}{\partial x_3} + [\langle u_j \rangle \frac{\partial q}{\partial x_j} + u'_j \frac{\partial q}{\partial x_j} + \frac{\partial}{\partial x_j} (u'_i \tau'_{ij})] + u'_i \frac{\partial p'}{\partial x_i} + u'_i \frac{\partial \langle p \rangle}{\partial x_i} + u'_i \frac{\partial \langle \tau_{i3} \rangle}{\partial x_3} - \tau'_{ij} s'_{ij} = 0, \quad (\text{A.5})$$

where, $q = \frac{1}{2} u'_i u'_i$ and $s'_{ij} = \frac{1}{2} (\frac{\partial u'_i}{\partial x_j} + \frac{\partial u'_j}{\partial x_i})$. In Eqn. A.5 the first term on the left-hand side denotes production of *tke* by mean shear, the second term captures the spatial redistribution of *tke* by the mean flow and turbulence, and the third and fourth terms denote velocity and pressure correlation. The fifth term stands for redistribution of *tke* by horizontally averaged subgrid-scale turbulence, and the last term denotes subgrid-scale dissipation by turbulent motions. Although the different terms of this *tke* transport equation were not directly analyzed in this study, it served as a guidepost for the inter-scale energy transfer analysis. In this study, a scale dependent version of the combined terms $(-\frac{\partial}{\partial x_i} \langle p' u' \rangle - u'_j \frac{\partial \langle q \rangle}{\partial x_j} - \frac{\partial}{\partial x_j} \langle u'_i \tau'_{ij} \rangle + \langle \tau'_{ij} s'_{ij} \rangle)$ was analyzed via a discrete wavelet framework.